8-2018

Si-based Germanium Tin Photodetectors for Short-Wave and Mid-Wave Infrared Detections

Thach Pham
University of Arkansas, Fayetteville

Recommended Citation

Pham, Thach, "Si-based Germanium Tin Photodetectors for Short-Wave and Mid-Wave Infrared Detections" (2018). *Theses and Dissertations*. 2838.
http://scholarworks.uark.edu/etd/2838

Si-based Germanium Tin Photodetectors for Short-Wave and Mid-Wave Infrared Detections

A dissertation submitted in partial fulfillment
of the requirements for the degree of
Doctor of Philosophy in Engineering with a concentration in Electrical Engineering

by

Thach Ngoc Pham
University of Arkansas
Bachelor of Science in Electrical Engineering, 2011
University of Arkansas
Master of Science in Electrical Engineering, 2013

August 2018
University of Arkansas

This dissertation is approved for recommendation to the Graduate Council.

Shui-Qing (Fisher) Yu, Ph.D. Dissertation Director	Gregory Salamo, Ph.D. Dissertation Co-Director
Hameed A. Naseem, Ph.D. Committee Member	Simon Ang, Ph.D. Committee Member

Abstract

The demand of light-weight and inexpensive imaging system working in the infrared range keeps increasing for the last decade, especially for civil applications. Although several group IV materials such as silicon and germanium are used to realize detectors in the visible and near infrared region, they are not the efficient approach for imaging system in the short-wave infrared detection range and beyond due to bandgap limit. On the other hand, this market is heavily relied upon mature technology from III-V and II-VI elements over years, which are costly to growth and incompatible with available Si complementary metal-oxide-semiconductor (CMOS) foundries. This limits the fabrication of large scale focal plan arrays detectors in this detection range. Therefore, a material system that meets the necessary requirements has long been in demand.

The $Ge_{1-x}Sn_x$ material system has been introduced as a potential solution for low-cost high-performance photodetector for short-wave infrared towards mid-infrared detections due to its compatibility with Si CMOS process and wide detection range by incorporating more Sn in the alloy. Since then, immense growth efforts have been made to improve the material quality reaching device-quality using commercial chemical vapor deposition (CVD) reactors or molecular beam epitaxy (MBE) chambers.

This dissertation will develop Si-based GeSn photodetectors technology to realize low-cost high-performance focal plane arrays detectors working in the SWIR towards MIR. It began with the development of fabrication process of single element GeSn photoconductor and photodiode, followed by systematic characterization and analysis of detectors' figures of merits to provide a more optimized structure. A peak responsivity of 20 A/W (photoconductor) and 0.34 A/W (photodiode) at 2 µm were achieved. An external quantum efficiency of 20 % was reported for the first time. The highest value of specific detectivity D* is only 3-4 times less than commercially

available Extended-InGaAs detector. Surface passivation technique was also pursued to reduce surface leakage current. Finally, infrared imaging capability was demonstrated using single pixel detector. The study involves a wide range of Sn composition from 10 to 22 %.

Acknowledgment

I would like to express my deep gratitude and my sincere thanks to my advisor, Dr. Shui-Qing (Fisher) Yu, who always motivates and fully supports me during my research time. He gave me opportunity to study, work, develop skills, and become mature. I would like to thank Dr. Gregory Salamo, Dr. Simon Ang, and Dr. Hammed A. Naseem to be part of my Ph.D. committee members.

I am also grateful to Dr. John Tolle, and Dr. Joe Margetis from ASM for providing high quality GeSn samples used in this research work. I thank Dr. BaoHua Li of Arktonics LLC. where I gained precious working experience. Many thanks to Dr. Mourad Benamara from Nano Institute and Errol Porter from HiDEC for providing excellent training and support of facilities usage.

Special thanks to Dr. Wei Du for the very useful discussion and assistance in paper writing. Huong Tran for being a very good lab partner, Yiyin Zhou for all of the support in clean room, and other colleagues Sattar Al-Kabi, Wei Dou, P.C. Grant, Matt. Grant, Seyed Amir, …

I would like to thank my family who are always being understanding and supportive and colleagues and friends who make my time living in Fayetteville enjoyable. Special thanks to Liang Huang for all the conversations he inspired me.

The work in this dissertation was partially supported by an Air Force SBIR Phase-II Project "Epitaxial Technologies for SiGeSn High Performance Optoelectronics Devices" under contract number FA9550-16-C-0016 (PI: Dr. Baohua Li from Arktonics LLC and Program manager: Dr. Gernot S. Pomrenke from Air Force Office of Scientific Research). Any opinions, findings, and conclusions or recommendations expressed in this material are those of the author and do not necessarily reflect the views of the Air Force. The work is also supported by the National Science

Foundation (NSF) under contract number EPS-1003970. Any opinions, findings, and conclusions or recommendations expressed in this material are those of the author and do not necessarily reflect the views of the NSF. Support is also appreciated from Defense Advanced Research Projects Agency DARPA under contract number W911NF-13-1-0196 (Program Manager: Dr. Jay Lewis). Any opinions, findings, and conclusions or recommendations expressed in this material are those of the author and do not necessarily reflect the views of the DARPA. Final National Aeronautics and Space Administration Established Program to Stimulate Competitive Research (NASA EPSCoR) under contract number NNX15AN18A. Any opinions, findings, and conclusions or recommendations expressed in this material are those of the author and do not necessarily reflect the views of the NASA.

Chapter 2 and 4 are largely reproduced from publications in the Electronics Letter, Optical Express, and Journal of Applied Physics.

Parts of chapter 2 were originally published as:

(1) "Si-based $Ge_{0.9}Sn_{0.1}$ photodetector with peak responsivity of 2.85 A/W and longwave cutoff at 2.4 µm," T.N. Pham, W. Du, B.R. Conley, J. Margetis, G. Sun, R.A. Soref, J. Tolle, B. Li and S.-Q. Yu, *Electron. Lett.*, vol. 51, no. 11, pp. 854–856, May 2015.

Parts of chapter 4 were originally published and are accepted as:

(1) "Systematic study of Si-based GeSn photodiodes with 2.6 µm detector cutoff for short-wave infrared detection," T. Pham, W. Du, H. Tran, J. Margetis, J. Tolle, G. Sun, R. A. Soref, H. A. Naseem, B. Li, and S.-Q. Yu, *Opt. Express*, vol. 24, no. 5, pp. 4519–4531, Mar. 2016.

(2) "High performance $Ge_{0.89}Sn_{0.11}$ photodiodes for low-cost shortwave infrared imaging," H. Tran, T. Pham, W. Du, Y. Zhang, P.C. Grant, J.M. Grant, J. Margetis, J. Tolle, G. Sun, R. A. Soref, M. Mortazavi, B. Li, and S.-Q. Yu, *J. Appl. Phys*, 2018.

Table of Contents

List of Figures

List of Tables

Chapter 1: Introduction

1.1 Motivation

The infrared radiation was first discovered by Friedrick William Herschel in the early 19th century [1]. Since then, numerous efforts have been made to detect and analyze the spectrum, which prospered the invention of the first infrared photodetectors in early 20th century. This IR radiation in general span from 0.8 to 12 μm and was divided into different categories as follow: (1) near-IR region ranging from 0.8 to 1.0 μm, (2) short-wave IR (SWIR) ranging from 1.0 to 3.0 μm, (3) mid-wave IR (MIR) region ranging from 3.0 to 5.0 μm, (4) long-wave IR (LWIR) ranging from 8.0 to 12.0 μm, and (5) very long-wave IR which covers wavelength beyond 12.0 μm. There is a range from 5.0 to 8.0 μm that wasn't classified into any categories due to large atmospheric absorption preventing the transmission of those wavelengths in this particular range [2].

Over the years of research and develop, IR photodetectors were revealed with numerous applications. The MWIR and LWIR regions are most important for free-space communications and astronomy since the high transparency of the atmosphere at these wavelengths allows transmission without significant losses [3], [4]. The same regions are also widely used for night vision and missile tracking for military applications. On the other hand, the SWIR regime has its own advantages and interests. By nature, the night-glow of sky contains SWIR illumination that is sufficient to passively enable SWIR detector while it cannot be observed by human eyes. Besides, SWIR has unique inspection capabilities such as: (1) seeing through many packaging materials which is opaque in visible spectrum without the need of contact or destroying the objects, (2) improved penetration through scattering media such as fog, haze, and tissue [5]. Due to distinct features of SWIR technology listed above, it has been used for a vast multitude of applications from military applications to civil applications including automotive, solar cell inspection, materials and products quality control, gas sensing, surveillance, night vision camera …[6], [7]. The market of infrared camera integrated on automobile and cell phone is the most attracting one with a market value estimated at millions of dollars.

The market of SWIR imaging is currently dominated by mature technology from III-V elements such as indium gallium arsenide (InGaAs and extended-InGaAs), indium antimonide (InSb), from II-VI such as mercury cadmium telluride (MCT), lead sulfide (PbS), and from silicon (Si) and germanium (Ge) for shorter wavelength. Figure 1 depicts the spectral detectivity of dominant detectors working in the SWIR. Since the first introduction of MCT and InSb photodetectors in 1960s, the quality of those materials was gradually improved and has become one of most popular materials for IR photodetectors. However, both MCT and InSb detectors require cryogenic cooling system to deliver good performance imaging [8]. Cooling requirements are the main obstacle to the more widespread use of IR systems that makes them bulky, heavy, expensive and inconvenient to use. The cost equipping a cryogenic cooling system ranges from \$15k to \$50k, which increases the total cost of a detector. On the other hand, InGaAs detectors, which was first demonstrated in 1980s, offer low dark current and high responsivity at room temperature [4], [8]. Despite its immense performance, InGaAs detectors or either MCT, PbS, InSb are incompatible with CMOS process. The fabrication of SWIR could not inherit any benefits from available CMOS foundries which results in limited sizes of focal plane arrays (FPAs), high cost, and limited mass production. Other competitors that are worth to notice are Si and Ge detectors which have good performance in the range of 1.0-1.6 µm. Although strain engineering was pursued to reduce the band-gap [9], [10], the progress of extending the detection range beyond 2.0 µm becomes difficult. Therefore, a material system that meets the necessary requirements (e.g. working in SWIR towards MIR with good performance and CMOS fabrication process compatible to be non-expensive solution either using single element detector or FPAs) has long been in demand.

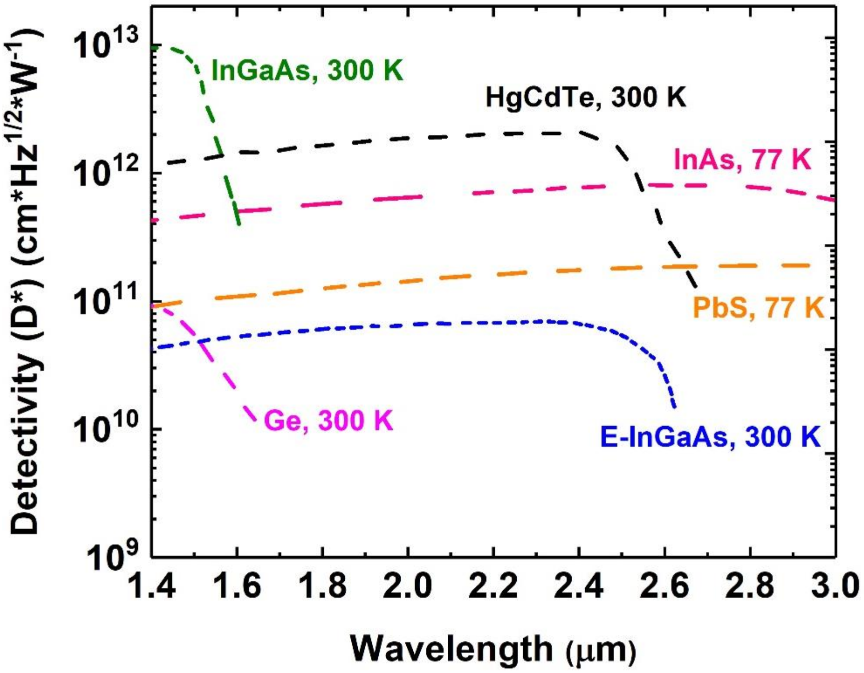

Figure 1: Replotted spectral detectivity of InAs, PbSe, Ge, PbS, HgCdTe, and InGaAs detectors [11]

The field of Si photonics has seen impressive growth since the early visions of 1980s and 1990s. It has achieved numerous applications in near IR wavelength range in the fields of interconnect, sensors, imaging, displays, and optical storage [12]. The success of Si photonics was thought to be limited within NIR range not until R. Soref proposed a new vision that newly designed silicon-based optoelectronic circuits will operate from 1.6 to 200 um range [13]. Since then, endless efforts of developing new material system from group IV was made to establish a solid foundation of Si-based optoelectronics devices working in the SWIR range and beyond. A newly developed group IV alloy, GeSn, has been introduced with outstanding material properties that are favorable for SWIR detection:

- The ability to engineer the lattice constant and bandgap by varying the composition of Ge and Sn
- Wide range of coverage from SWIR and beyond up to 12 µm through band-to-band transitions
- Low material growth temperature below 400°C fully compatible with CMOS process
- The feasibility of selective area growth which is desirable for optoelectronics integration

1.2 Background:

Germanium (Ge) was first investigated as a candidate material to incorporate on Si optoelectronics. Much success was achieved in developing high speed Ge detectors with responsivity of 1 A/W at 1.55 µm and a working bandwidth in GHz level [9]. However, Ge light emission device performance was limited due to its indirect bandgap. Either introducing 2% tensile strain into Ge film or high doping level up to 3×10^{19} cm^{-3} (n-type) could compensate for the energy difference between Γ (direct) and L (indirect) valleys. This resulted in successful demonstration of Ge laser with emission at 1.6 µm [14]. The solutions also suffer from difficulties in fabrication of tensile strain Ge and low performance of heavily doped Ge laser.

Tin (Sn), also a group IV element, is a semi-metal with a diamond cubic allotrope. When it is introduced to Ge to form $Ge_{1-x}Sn_x$ alloy, the band gap of the material can be tuned. This incorporation of Sn shrinks Γ (direct) and L (indirect) valleys. Since Γ valley drops faster than L valley as Sn incorporation increases, it allows a crossover point from indirect to direct material (6 – 10 % Sn depending on the strain of the GeSn film) [15]. The wide range of tunable bandgap of GeSn alloy as shown in Figure 2 (band gap versus lattice constant) shows promising potential for SWIR towards MIR detection range.

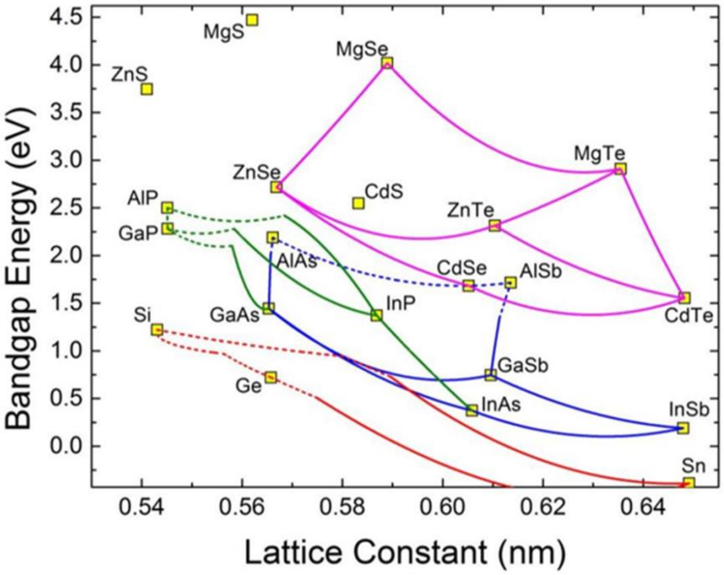

Figure 2: Lattice constant versus bandgap energy of Si-Ge-Sn ternary, III-V, and II-VI compounds [16]. Dotted lines signify indirect bandgap materials and solid lines mark direct bandgap materials.

The major technical challenge with Sn incorporation into the Ge lattice is the large lattice mismatch between the elements (17%) and the instability of the α-Sn (or grey Sn) above 13^{o}C [17]. This results in unstable GeSn alloy. Various deposition technique via chemical vapor deposition (CVD) or molecular beam epitaxy (MBE) has been explored. With the discovery of a viable Sn precursor, deuterated stannane SnD_4, significant material breakthrough using UHV-CVD was made [18], [19]. In 2012, an alternative low cost and chemically stable precursor tin tetrachloride $SnCl_4$ was found for material growth using CVD reactors in combination with germane or di-germane precursors. Since then, there has been a huge growth for GeSn research with reports of material growth, material characterizations, and high performance devices such as: demonstration of direct bandgap [15], [20] followed by demonstration of optical pump laser [21]–[23] , quantum-well study [24]–[28], light emitting devices [25], [29], [30], photodetectors [31]–[59] …

The summary in Table 1 highlights key parameters of $Ge_{1-x}Sn_x$ photodetectors that were developed through years:

Table 1: Summary of $Ge_{1-x}Sn_x$ and $Si_{1-x-y}Ge_ySn_x$ photodetectors

Year	**Sn% Si%**	**Structure**	**Responsivity λ = 1.55 µm @-1 V bias (A/W)**	**Responsivity λ > 1.55 µm @-1 V bias (A/W)**	**I_{Dark}**	**Ref.**
2009	2 % Sn	PIN	0.05 @ -0.16 V	-	1 A/cm^2	ASU [31]
2011	0.5 % Sn	PIN	0.1	-	10 A/cm^2	Stuttgart [32]
2011	2 % Sn	PIN	0.12 @ -0.25 V	-	1.0 A/cm^2	ASU [33]
2011	3 % Sn	PIN	0.23	0.12 @1.64 µm	1.8 A/cm^2	CAS China [34]
2012	2 % Sn, 7 % Si	PIN	-	-	1 mA/cm^2	ASU [35]
2013	3.85 % Sn	PIN	0.27	0.165 @1.6 µm	0.4 A/cm^2	NTU Taiwan [36]
2012	4 % Sn	PIN	0.2	0.17@1.6 µm	100 A/cm^2	Stuttgart [37]
2012	9 % Sn	QW/PC	1 @ -5 V	0.1 @ 2.2 µm	0.5 mA	Ghent Belgium [38]
2013	3.6 % Sn	PIN/ Ge substrate		0.71 A/W @ -3V and 1790 nm	6.1 mA/cm^2	CAS China [39]
2013	8 % Sn	PN	0.031	-	11 µA @ -1 V	Stanford [40]
2013	9.8 % Sn	PN	-	-	100 µA @ 5 V	Delaware [41]
2013	9 % Sn	PN	-	-	1 A/cm^2 @ -0.6 V	Delaware [42]
2014	1.78 % Sn	PIN	0.18 @ 0 V	-	0.05 A/cm^2	NCCU Taiwan [43]

Table 1 (Cont.): Summary of $Ge_{1-x}Sn_x$ and $Si_{1-x-y}Ge_ySn_x$ photodetectors

Year	**Sn% Si%**	**Structure**	**Responsivity λ = 1.55 µm @-1 V bias (A/W)**	**Responsivity λ > 1.55 µm @-1 V bias (A/W)**	$\mathbf{I_{Dark}}$	**Ref.**
2014	4.2 % Sn	PIN	0.22 @ 0V	-	0.89 A/cm^2	Stuttgart [44]
2014	7 % Sn	QW/PIN	0.13	-	0.1 A/cm^2	Stuttgart [45]
2014	7 % Sn	PC	0.18 @ 10 V	-	1.5 mA @ 10 V	UA [46]
2014	10 % Sn	PC	1.63 @ 50 V	-	-	UA [47]
2014	12 % Sn	PN	-	-	0.05 A @ -0.5 V	Delaware [48]
2015	5 % Sn	PIN	0.18	0.06 @ 1.63 µm	73 mA/cm^2	NUS Singapore [49]
2015	10 % Sn	PC	2.85 @ 5V	-	7.7 A/cm^2	UA [50]
2016	2.5 % Sn	PIN	0.3	-	1 mA/cm^2 @-0.5 V	NTU Taiwan [51]
2016	2.5 % Sn	Arrays/PIN	-	0.45 A/W @ 1.7 µm	0.1 mA/cm^2 @-0.1 V	NTU Taiwan [52]
2016	6% Sn	PIN	0.35	0.09 @ 2 µm	3 A/cm^2	CAS China [53] [54]
2016	10 % Sn	PIN	0.19 @ -0.1 V	-	4.3 A/cm^2	UA [55]
2017	2.8 % Sn	MQW/PIN	62 mA/W	-	0.059 A/cm^2	NCCU/NTU Taiwan [56]
2017	3% Sn	QW/PIN	-	-	4 mA/cm^2	Stanford [57]
2017	10% Sn	MQW PIN	-	0.02 A/W @ 2 µm	0.031 A/cm^2	NUS Singapore [58]
2018	8 % Sn	MSM (GeSnOI)	0.39 A/W	0.1 A/W @ 2 µm	65nA @1V	NUS Singapore [59]

1.3 Challenges and goals:

Last couple of years witnessed the potential and growing performance of GeSn photodetectors that is approaching the one of extended-InGaAs. Yet, the device design, either photodiodes or photoconductors, was not fully optimized. Hence, there is a room for GeSn photodetectors performance to be improved by (1) controlling and optimizing the active layer thickness, the Sn composition, and the doping concentration, and (2) applying an effective surface passivation which is necessary to reduce the leakage current. The optimization process is therefore needed, yet, it should be matched with growth and fabrication capabilities. It is also worth to note that the interface layer between Ge buffer and high quality GeSn was also found to be an unintentional defective layer. As a result, GeSn photodetector performance will be reduced and Ge buffer will also contribute to the overall detector results. Finally, realizing images in IR range using single element / arrays of GeSn detectors that is being developed has not yet been fully explored.

The long-term goal of this work is to demonstrate low cost high performance GeSn FPAs detectors by using Si-based GeSn photodetectors. To realize this goal, it is necessary to establish the baseline performance of single element GeSn photodetectors starting with photoconductor and photodiode structure. The study began with the evaluation of thin film photoconductors (~200 nm) with 10 % Sn. The active GeSn film thickness was eventually increased up to 1.0 µm and Sn composition ranges from 11 % to 22 %, which is the world-record at that time. The study of GeSn photodiodes began with 7 % and 10 % Sn samples, based on which a more optimized photodiode design structure was proposed, fabricated, and characterized using 11 % Sn. External quantum efficiency was reported as the first time. A 2.0 µm incident laser source was used to eliminate the contribution of Ge layers. Second, two different surface passivation methods, which are germanium oxynitride and germanium / germanium tin oxide with aluminum oxide, were studied to reduce the surface leakage current. Third, imaging capability in SWIR using single element GeSn photodetectors was developed by controlling the movement path in such way that follows the structure of a detector array. Subsequently, linear arrays would be implemented. Finally, fabrication process of GeSn photodetectors was developed and improved.

1.4 Photodetectors background and figures of merits:

1.4.1 Photoconductor:

The detection principle of a photoconductive detector is defined by the change of the conductivity when an incident light source having energy greater than the bandgap of the detector material shines upon it. Due to photons excitation, the additional free charge carriers are generated in the semiconductor. As the electric field is applied, those photogenerated carriers, which cause an increase in the conductivity of the detector, are collected at the electrodes and form the photocurrent, as shown in Figure 3.

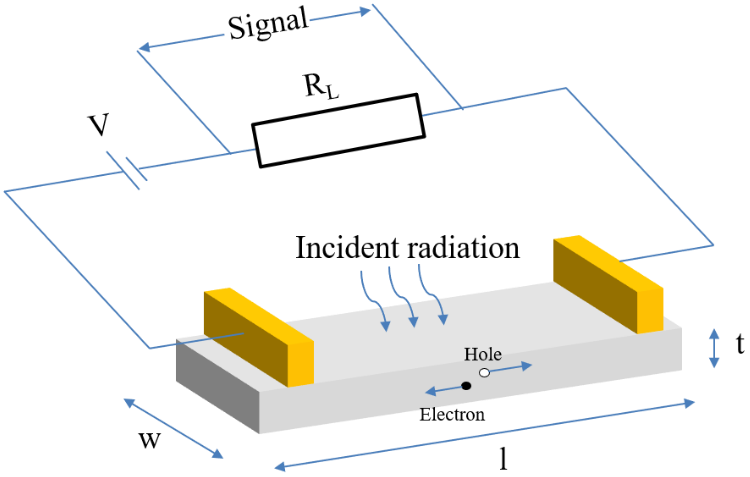

Figure 3: Geometry and bias of a photoconductor

The conductivity (ohm^{-1}cm^{-1}) of a photoconductive detector without illumination can be expressed as:

$$\sigma_o = N_o\mu_n q + P_o\mu_p q \quad (1)$$

Where N_o and P_o are free carrier concentrations of electron and holes (cm^{-3}), μ_n and μ_p are mobilities of electron and holes (cm^2 sec^{-1} V^{-1}), and q is charge on electron, 1.6×10^{-19} cm^{-3}.

As excess electrons δn and holes δp are generated by the absorption of photons, the conductivity is increased by an amount:

$$\Delta\sigma = \delta n\mu_n q + \delta p\mu_p q = \delta n(\mu_n + \mu_p)q \quad (2)$$

Since each absorbed photon breaks a bond and creates an electron-hole pair, the excess electron and hole are equal. Assuming the light intensity is constant and independent with time (or steady state), the excess carriers in intrinsic semiconductors become:

$$\delta n = G_o\tau_n \quad (3)$$

where G_o is the net optical generation rate and τ_n is electron lifetime. The change in conductivity can be rearranged as:

$$\Delta\sigma = G_o\tau_n(\mu_n + \mu_p)q \quad (4)$$

The photocurrent can be expressed as:

$$\Delta I = \Delta JA = \Delta\sigma EA = G_o\tau_n\left(\mu_n + \mu_p\right)qA\frac{V}{l} \quad (5)$$

or

$$\Delta I = G_o qlA\,(\frac{\tau_n}{\tau_{t,n}} + \frac{\tau_n}{\tau_{t,p}}) \quad (6)$$

where A = w×t is the corss-sectional area, E = V/l is the electric field, $\tau_{t,n}$ is the electron transit time, $\tau_{t,p}$ is the hole transit time.

The ratio ($\frac{\tau_n}{\tau_{t,n}} + \frac{\tau_n}{\tau_{t,p}}$) is defined as the photoconductive gain showing how fast carriers can transit to electrodes and contribute to the photocurrent before they are recombined. It could be further simplified as $\frac{\tau}{\tau_{t,n}}$ since electrons seems to dominate the conductivity in well-known high sensitivity photoconductors [reference?]. If τ_n is much shorter than transit time, the electron and hole will immediately recombine, which result in a small photocurrent. If the transit time is shorter than the carrier lifetime, more photocurrent is generated thanks to significant increase in the amount of electron / hole reaching the electrodes without being recombined.

Next, the optical generation rate G_o is defined as the number of injected photon flux per unit volume multiplied by the quantum efficiency

$$G_o = \eta \frac{P_{inc}/hv}{lwt} \tag{7}$$

where P_{inc} is the optical power (W) of incident light, l×w×t is the unit volume, and η is the quantum efficiency. The QE is a function of absorption multiplied with intrinsic quantum efficiency η_i or the number of electron-hole pairs generated by each absorbed photon.

$$\eta = \eta_i (1 - R)(1 - e^{\alpha d}) \tag{8}$$

where R is the optical reflectivity between air and semiconductor, α is the absorption coefficient, and d is active layer thickness. The photocurrent will become:

$$\Delta I = \eta \frac{P_{inc}/hv}{lwt} qlA \left(\frac{\tau_n}{\tau_{t,n}} + \frac{\tau_n}{\tau_{t,p}}\right) = \eta q \frac{P_{inc}}{hv} \left(\frac{\tau_n}{\tau_{t,n}} + \frac{\tau_n}{\tau_{t,p}}\right) \tag{9}$$

Dividing equation of the photocurrent by the optical incident power yields the responsivity (A/W), which is one of figure of merit of photodetector:

$$\Re = \frac{\Delta I}{P_{inc}} = \eta \frac{q}{hv}\left(\frac{\tau_n}{\tau_{t,n}} + \frac{\tau_n}{\tau_{t,p}}\right) \tag{10}$$

1.4.2 Photodiode

When the incident light having energy greater than the bandgap of the photodiode material illuminated the photosensitive area, the electrons in valence band are excited to the conduction band and leaves holes in the valence band. This effect occurs throughout N region, P region, and depletion region. In the depletion region, the electric field swept the electrons towards N region while holes moved to P region. At the same time, electrons in P region (conduction band) and holes in N region (valence band) are subsequently diffused to N region and P region respectively. As electrodes are formed and connected to external circuit, the electrons located in N regions and the holes located in P regions will be extracted and form photocurrent.

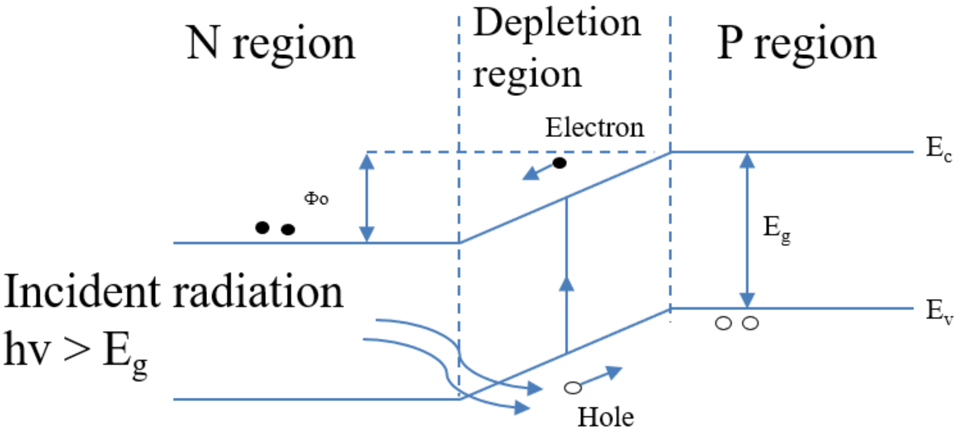

Figure 4: Band diagram p-n junction of a photodiode

In addition to the required energy of incident light for the photo excitation, the temperature of the photodiode should be low to avoid thermal excitation across the bandgap, especially for low bandgap material, GeSn, e.g. $\frac{kT}{q} \ll E_g$ (eV). k is the Boltzmann's constant (1.38×10^{-23} WsK^{-1}) and T is the temperature (K).

The depletion width where electron-hole pairs are generated from photon excitation is defined in centimeters as:

$$W = 10^3 \sqrt{\frac{K\phi_o(N_d + N_a)}{N_a N_d}} \tag{11}$$

where K is the dielectric constant (K=16 for Ge), N_d is the donors concentrations in N region, N_a is the acceptors concentration in the P region, and Φ_o is the potential barrier: $\phi_o = \frac{kT}{q} \ln\left(\frac{N_a N_d}{n_i^2}\right)$. n_i is the intrinsic carrier concentration. The diffusion length of electrons and holes are expressed as:

$$L_e = \sqrt{\frac{kT}{q}\mu_e \tau_e} \tag{12}$$

$$L_h = \sqrt{\frac{kT}{q}\mu_h \tau_h} \tag{13}$$

where μ_e and μ_h are electron and hole mobilities, and τ_e and τ_h are electron and hole lifetimes. The absorption is quite small in the diffusion length.

The dark current and photocurrent of a photodiode in a steady state are described as follow:

$$I_{dark} = I_o(e^{\frac{qV}{kBT}} - 1) \tag{14}$$

$$I_{ph} = qAG_o(L_h + L_e) = q\eta \frac{P_{inc}}{hv} \tag{15}$$

where I_o is the reverse saturation current. Once again, the responsivity is the ratio of photogenerated current over the optical incident power. Unlike the responsivity of photoconductor, the gain is typically equal to one.

$$\Re = \frac{I_{ph}}{P_{inc}} = \eta \frac{q}{hv} \tag{16}$$

1.4.3 Figures of merits

Responsivity, the ratio of photocurrent to incident light intensity, indicates how efficiently the detector responds to an optical signal. It is expressed as

$$\Re = \frac{I_{ph}}{P_{inc}} = \eta \frac{q}{hv} \times Gain \tag{16}$$

The gain in photoconductor is defined as the ratio of effective carrier lifetime versus carriers transit time as described above. Therefore, increasing photoconductive gain will result in an increase of responsivity. There are several methods to enhance the photoconductive gain among which the reduction of the transit time is presented in this study. It was implemented in the fabrication process of photoconductor by introducing interdigitated electrodes which reduces the travel distance of electrons / holes. In addition, an increase in applied bias will significantly reduce the transit time as well. In the case of photodiode, the gain becomes one.

Another method to improve the responsivity is to reduce the loss in the quantum efficiency. The ideal value of one is desired, yet there are losses due to: (1) optical reflection losses; (2) surface traps or recombination; (3) absorption coefficient and absorption depth; (4) generation of carriers located a long distance away from the depletion region. For Ge / GeSn material, the reflection loss (normal incident) is approximately ~0.36. This loss could be reduced by applying an antireflection coating and was not included in this study. Besides, the loss due to surface traps or recombination could be overcome by applying an effective surface passivation that was discussed in chapter 5. Next, the absorption coefficient of different Sn composition ranging from 7 % to 20 % remains at around 10000 cm^{-1}. To match with the absorption coefficient, a thicker active layer is required.

However, this is strongly dependent on the growth capability. In our study, the thickness of GeSn active layer was increased up to 1.0 µm (photoconductor) and 500 nm (photodiode). Finally, photodiode structure has been revised to optimize the position of depletion region and diffusion length (chapter 4 part 2).

Another figure of merit is the noise equivalent power (NEP). It is the required power incident on the detector to produce a signal output equal to the rms noise output. In other word,

$$NEP = i_{rms}/\Re \tag{17}$$

where i_{rms} is the root-mean-square noise current (A) and $\Re$ is the responsivity (A/W). Either spectral responsivity or blackbody responsivity could be used. This NEP value could be used to compare the detectivity performance of similar types of detectors in term of materials, structure, and size. In the case between different types of detectors, specific detectivity D* was preferred. This parameter (cm $Hz^{1/2}$ W^{-1} or Jones) normalizes the active detector area to 1 cm^2 and the noise bandwidth to 1 Hz.

$$D^* = \frac{\sqrt{A\Delta f}}{i_{rms}}\Re \tag{18}$$

where A is the active detector area, and Δf is the bandwidth over which the measurement collection occurs. In this context, it is also referred to as the equivalent noise bandwidth (ENBW) or the switching bandwidth defined as 1/(2*T), where T is the observational period. This bandwidth is different from the maximum bandwidth of the device in terms of switching speed. The i_{rms} is the sum of noise current in the detector system. It includes Johnson noise or thermal noise, shot noise due to the fluctuations of charges, generation-recombination noise, and 1/f noise.

$$i_{rms} = \sqrt{i_{shot}^2 + i_{thermal}^2 + i_{G-R}^2 + i_{1/f}^2} \tag{19}$$

The Johnson noise or thermal noise is contributed by the random thermal motion of charge carriers in a resistive element. It occurs in the absence of external applied bias and is linked with the resistance of the device. Either photoconductor or photodiode contains this noise.

$$i_{thermal} = \sqrt{4kT\Delta f/R_0} \tag{20}$$

where k is Boltzmann constant, T is the absolute temperature, Δf is the measurement bandwidth (1 Hz), and R_o is the resistance of the device.

The generation-recombination noise is referred as the random generation and recombination of free charge carriers due to crystal vibrations. The Generation-recombination noise occurs mainly in photoconductor since recombination is invalid in an ideal photodiode limited by diffusion.

$$i_{G-R} = \sqrt{\frac{4qI\Delta f \times Gain}{1 + (2\pi f\tau)^2}} \tag{21}$$

The shot noise describes the fluctuations of electrons at the collection circuit and is described as:

$$i_{shot} = \sqrt{2qI\Delta f} \tag{22}$$

where I is the average current flow from a photodetector under illumination. This mean I contains dark current and photo current.

The 1/f noise or flicker noise dominates the noise current if the detector works under low frequency condition.

$$i_{1/f} = \sqrt{\frac{BI_{DC}^a\Delta f}{f^b}} \tag{23}$$

where B is a constant depending on detector material, I_{DC} is the DC current through detector, f is frequency under measurement, a and b are constant and usually have value of 1 and 2 respectively. 1/f noise is usually negligible by considering an appropriate measuring frequency.

1.5 Organization

Design, fabrication, and characterization of GeSn photoconductors are organized as follow. The first chapter gives an introduction and motivation of Si-based GeSn photodetector for SWIR range towards MIR. It also contains background and figures of merit of photodetectors. The second chapter covers the study of thin film photoconductors. Interdigitated electrodes structure was introduced and fabricated to enhance the photoconductive gain, which increases the responsivity of the photodetector. Chapter 3 further explores photoconductor devices by introducing thick active layer up to 1.0 µm and incorporating high Sn % up to 22 %. This results in a tremendous enhancement in responsivity and extension in cut-off wavelength up to MIR. New fabrication process was developed in this chapter.

Chapter 4 involves the study of GeSn photodiode. The first part covers the baseline performance of 7 % and 10 % Sn photodiode, based on which analysis and simulation was processed to figure out limiting factors of photodiode structure. The second part presents the new proposed structure with significant enhancement in performance.

In order to reduce surface leakage current, two surface passivation methods were studied and is summarized in chapter 5 with detailed fabrication process and characterization. Chapter 6 focuses on the demonstration of SWIR imaging using a single element GeSn detectors that was fabricated and studied in previous chapters.

A summary of this work along with future approach is presented in chapter 7.

Chapter 2: Systematic Study of thin film $Ge_{1-x}Sn_x$ Photoconductors

This chapter conducts a study of thin film $Ge_{1-x}Sn_x$ photoconductors grown on Ge buffered Si. It evolves Si CMOS compatible fabrication process and temperature dependent characterization of GeSn photoconductor with a nominal Sn composition of 10 % and with film thickness of 100 nm. In this study, interdigitated structures were implemented to reduce transit time which results in enhancing photoconductive gain. Square mesas of 0.5 and 1.0 mm were fabricated into photoconductors with and without interdigitated electrodes. The electrode width is 3, 6, and 12 μm with a corresponding electrode gap of 6, 12, and 24 μm, respectively. Photoconductors without interdigitated electrodes or co-planar contacts were used as control samples. Spectral response at 77 and 300 K of photoconductors with Sn compositions up to 10 % has been investigated with longest cutoff at 2.4 µm. Temperature dependent responsivity of photoconductors has been conducted with a peak responsivity of 2.85 A/W at 1.55 µm and 77 K. This is higher than Ge (0.8 A/W) and standard InGaAs (1 A/W) detectors at the same wavelength. The specific detectivity of GeSn photoconductor has been improved and is one order of magnitude below extended-InGaAs detector. A peak D* of 3.5×10^9 $cm\cdot Hz^{1/2}W^{-1}$ was obtained.

2.1 Thin film $Ge_{1-x}Sn_x$ photoconductors growth and structures

In the past few years, the growth of high quality GeSn film was demonstrated by several research groups. Different growth approaches using either CVD system [60]–[67] or MBE system [32], [68]–[71] were employed with the use of Sn-based precursors deuterated stannane (SnD_4) or tin tetrachloride ($SnCl_4$) in combination with germane GeH_4 or digermane Ge_2H_6. Ge_2H_6 and SnD_4 have been used to demonstrate a film of Sn composition up to 15 % [67], [72], [73]. However, SnD_4 is well-known as an unstable gas and decomposes at room temperature while Ge_2H_6 is potentially explosive in liquid form due to its easiness of decomposition. Therefore, it requires specialized handling and storage which makes these precursors less appealing for widespread use in semiconductor manufacturing. $SnCl_4$, on the other hand, is a better choice for industrial standard deposition tools due to its stability and ease of handling and storing. In addition, GeH_4 is more stable and is cost-effective from industrial manufacture perspective.

In this study, the thin GeSn films were grown on Ge-buffered Si substrate using ASM Epsilon 2000 plus reduced pressure CVD system. The growth temperature was kept below 450^oC. $SnCl_4$ and GeH_4 were chosen as precursors for the growth of GeSn active layer and Ge buffer layer. The Ge buffer layer acts as a virtual substrate compensating the lattice mismatch with Si and reducing the defect propagation, which is one of the reason of lower material quality and device performance. Ge buffer thickness is kept around 700 nm and GeSn active layer thickness is approximately 200 nm and 100 nm for 7 % and 10 % Sn respectively. The Sn composition and thickness were determined by using X-ray diffraction (XRD) and secondary-ion mass spectrometry (SIMS). The thickness limit will be further explained in chapter 3 and more growth details are found in Ref [74].

2.2 Device fabrication

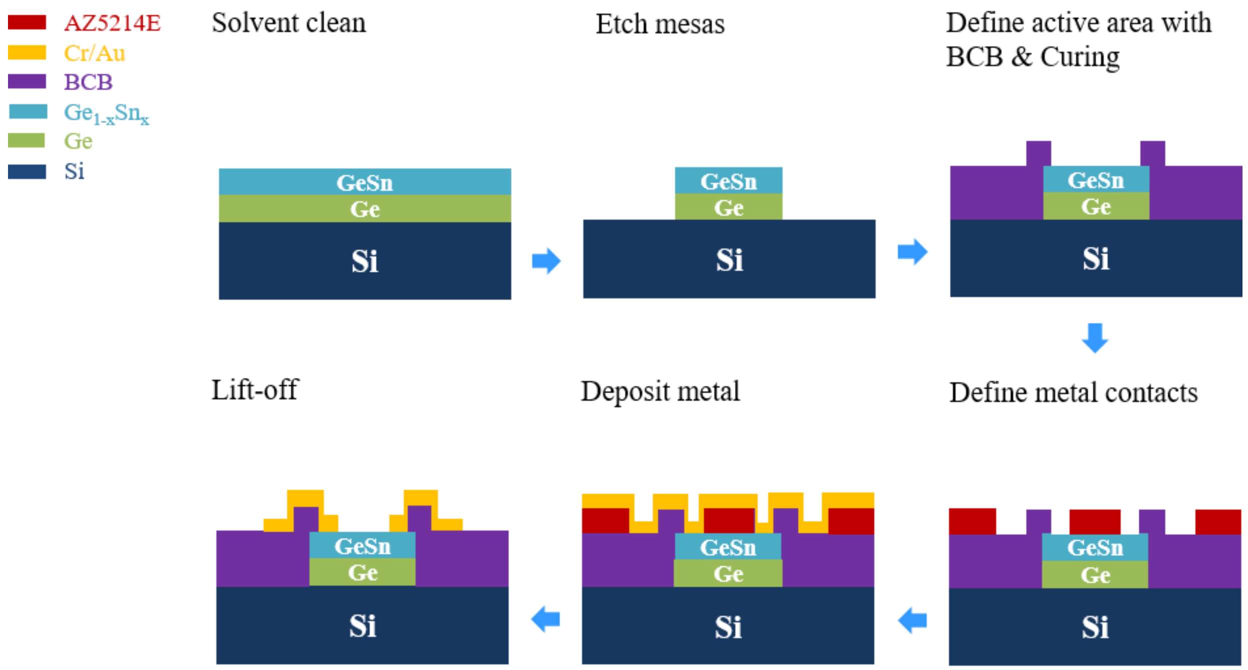

Figure 5: Fabrication process flow of thin film $Ge_{1-x}Sn_x$ photoconductors with interdigitated structures using photoactive BCB as dielectric layer

Thin film GeSn samples of 10 % Sn were fabricated into photoconductors with (IEPD) and without (standard or coplanar PD) interdigitated structures using three-steps mask. The fabrication process flow that was illustrated in Figure 5 has six major process steps. The fabrication process started with samples cleaning using acetone and isopropyl alcohol in ultra sonic bath for five minutes each to remove organic traces. After being rinsed with deionized water, the samples were baked for three minutes to dehydrate water vapor and to promote ahesion prior photolithography.

The second step, mesas etching, began with spin-coating of hexamethyldisilazane (HMDS) to achieve the surface hydrophobicity before applying positive photoresist AZ4110. Mesas with an area of 500 x 500 μm^2 each were defined using 1st photomask and developer AZ 300 MIF. Mesas etching was performed using Reactive-ion Etching (RIE) system from Plasma Therm. The etching process of GeSn / Ge samples could be explained as follows: the plasma glow assists in ionization of Ar gas to form Ar ions and dissociation of CF_4 gas into reactive ions which are CF_3 and F. At the GeSn surface, F radicals will react with Ge atoms to form volatile byproducts GeF_4 which is easily desorbed from the surface [75], [76]. In contrast, nonvolatile products tin fluoride (SnF_x) are formed when F radicals reacts with Sn atoms. This results in a deposition of very thin layer of SnF_x that prevents further chemical reactions. It also implies that the etching rate will be dramatically reduced as Sn composition increases. However, in case of thin layer of GeSn, it can still etch through thanks to physical sputtering effects by Ar ions. At the Ge buffer surface, Ar ions assist in breaking bonds and leave opened space for chemical reactions taking place. Subsequently, GeF_4 is formed as volatile byproducts, which are sputtered away. The etching process is calibrated to stop at Si substrate. The photoresist was stripped by using acetone and IPA in ultrasonic bath, followed by descum for three minutes. Figure 6 (a) shows the GeSn mesas after etching using RIE.

The third step is to define the detector active area where the incident light will be aligned and focused. A benzocyclobutene polymer (BCB) was spin-coated and exposed as a negative photoresist using the 2nd photomask. It also plays as an isulator layer. After development, an area of mm was opened on top of the mesas as shown in Figure 6 (b). GeSn samples were loaded into an oven with N_2 flow to proceed the BCB curing process at 250^o C for 5 hours. This resulted in a thickness of 3.5 µm which is 2.0 µm above the photoconductor mesas height and a slope at the sidewalls as shown in Figure 6 (f). However, BCB is not recommended for the process of high tin composition samples and samples with doping due to long period of baking at high temperature.

The next process defines metal contacts and interdigitated structures for photoconductors using the 3rd photomask. A negative photoresist AZ5214E was used to ease the lift-off process, followed by a descum step to completely remove resist residues. A Cr/Au thickness of 10 nm / 200 nm was deposited using thermal evaporator. Chromium was used to promote the adhesion between samples' surface and gold contacts. Fabrication of photoconductor samples were finished by a lift-off process in acteone and a rinse in IPA / DI water.

Figure 6 (d) and (e) present a top view optical image of the final photoconductor device without and with interdigitated electrodes 12-24. There are three sets of interdigitated structures which are 3-6, 6-12, and 12-24. The width of electrodes in each set is 3, 6, and 12 µm while the center to center spacing between two consecutive electrodes is 6, 12, and 24 µm respectively. The width of interdigitated electrodes contains 10 % error in size.

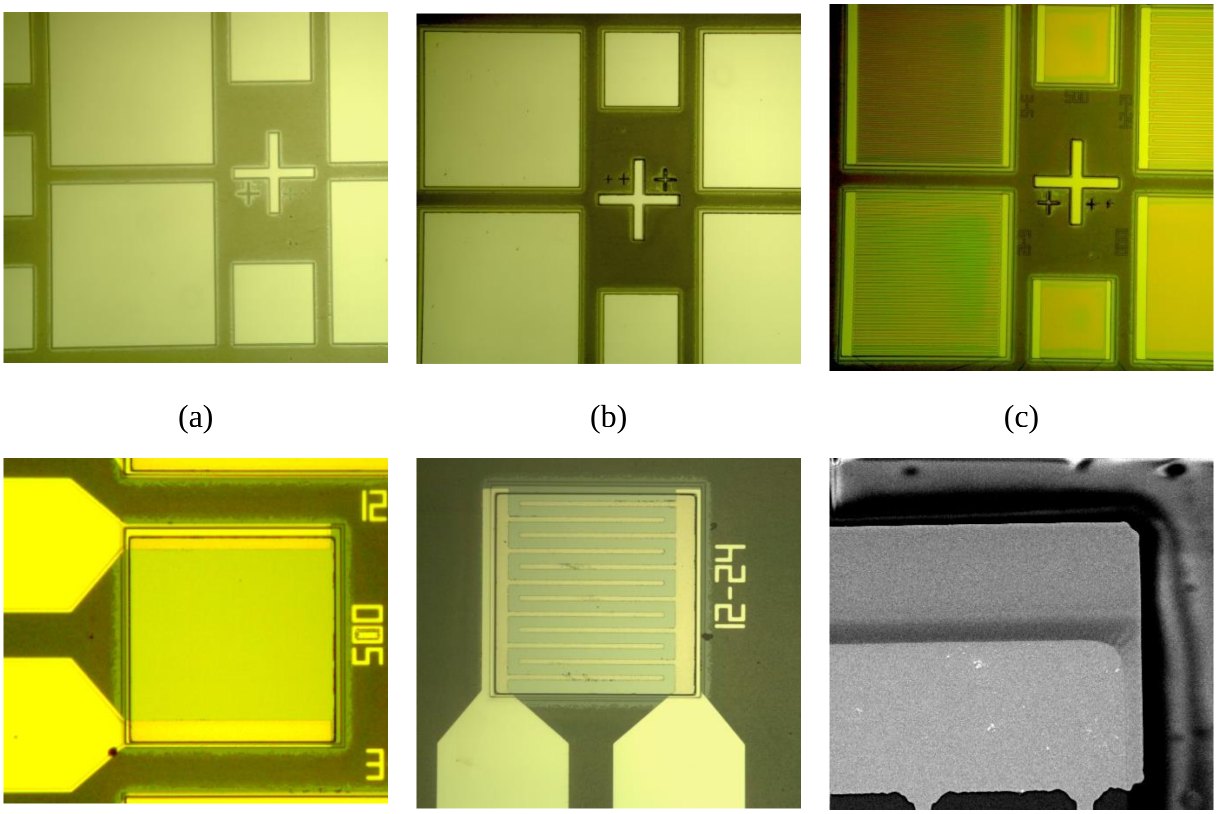

(a) (b) (c)

(d) (e) (f)

Figure 6: Top view microscope images of (a) mesas etching using RIE (1st mask), (b) defined active area with BCB (2nd mask), (c) defined metal contacts (3rd mask), (d) standard photoconductor after lift-off, (e) 12-24 interdigated photoconductor after lift-off, and (f) top view SEM image of a metal covered slope created by BCB.

2.3 Spectral response cut-off

Figure 7 summarizes the spectral response of photoconductors with low Sn composition from 0.9 to 10 % Sn that was characterized at 300 K and normalized at 1.5 µm. The 10 % cut-off was applied to evaluate cut-off wavelength of each Sn composition. The lowest Sn % device, 0.9 % Sn, shows a cut-off wavelength of 1700nm. This cut-off is further red shift to 1780, 1810, 2142, 2150, 2250 nm with 2.6, 3.2, 7, 8, 10 % Sn device respectively. As Sn composition increases, the cut-off wavelength is extended to longer coverage due to the reduced bandgap. This is in agreement with the Vegard's law interpolation between Ge and Sn [77]. The Sn composition used in the measurement is nominal Sn.

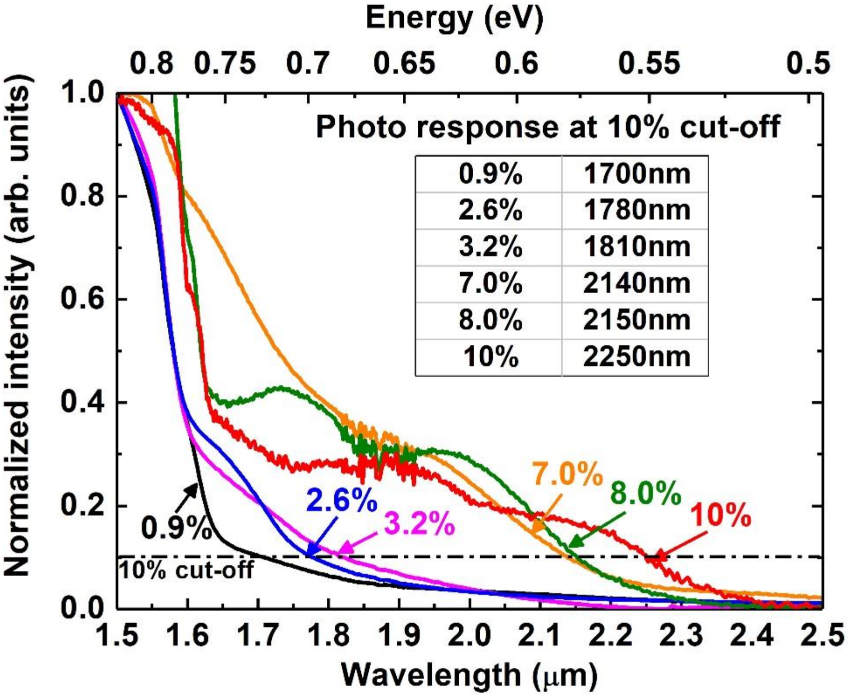

Figure 7: Normalized photoresponse at 10 % cut-off of low tin photoconductors (0.9, 2.6, 3.2, 7, 8, and 10 % Sn) was measured at 300 K.

The spectral response of 10 % Sn photoconductor was measured and normalized at 1.5 µm to allow direct comparison of cut-off wavelength at 77 and 300 K as shown in Figure 8 (a). As the temperature increases from 77 to 300 K, a red shift from 2.2 µm to 2.4 µm was observed. The long cut-off wavelength is beyond 1.55 µm which is the band-to-band absorption edge of Ge. This suggests that the absorption is contributed from GeSn material. The distortion of signal at 1.8 – 1.9 µm that occurs for every temperature is due to atmospheric absorption.

The absorption edge of 10 % Sn photoconductor was further investigated by analyzing the absorption coefficient of detector's active region. This value could be evaluated either by using spectroscopic ellipsometry or experimental photoresponse measurement as described in Refs [41], [78]. The photoresponse intensity is:

$$P_{PR} = P_{IN} \times (1 - e^{-\alpha x}) \tag{25}$$

where P_{IN} is the incident light intensity, α is absorption coefficient, and x is the device thickness. This equation can be simplified to $P_{PR} = C \times \alpha$ as the thickness of the $Ge_{0.9}Sn_{0.1}$ active layer is much smaller than the light penetration depth i.e., $\alpha x << 1$. Moreover, the absorption coefficient near the absorption edge can be expressed as:

$$\alpha \propto [hv - E_g \pm E_p]^m \tag{26}$$

where hν is the incident photon energy, Eg is the bandgap of the material, Ep is the energy of the phonon that allows for indirect bandgap transition, and m is a constant. Therefore, the m value and the bandgap near the absorption edge can be evaluated by fitting photon energy versus spectral response intensity as shown in Figure 8 (b). Based on the study of band-to-band transition, the m is generally equal to 2 and 1/2 for the indirect and direct bandgap transition, respectively. The m values in this study were extracted as 0.67 for the 10 % Sn device at 300 K and 2.09 at 77 K. The 10 % Sn alloy has been identified as a direct bandgap material, the Sn composition of 9.24% in this study is very close to the indirect-to-direct transition point. Although the sample is still an indirect bandgap material, the absorption arising from direct bandgap transition dominates the spectral response, leading to the m value of 0.67 which is close to 1/2. However, as temperature decreases, the m value goes up to 2.09 which indicates an indirect gap transition. The bandgap values near the absorption edge were extracted as 0.566 and 0.532 eV at 77 and 300 K. This is equivalent with a cut-off wavelength of 2188 at 77 K and 2326 nm at 300 K.

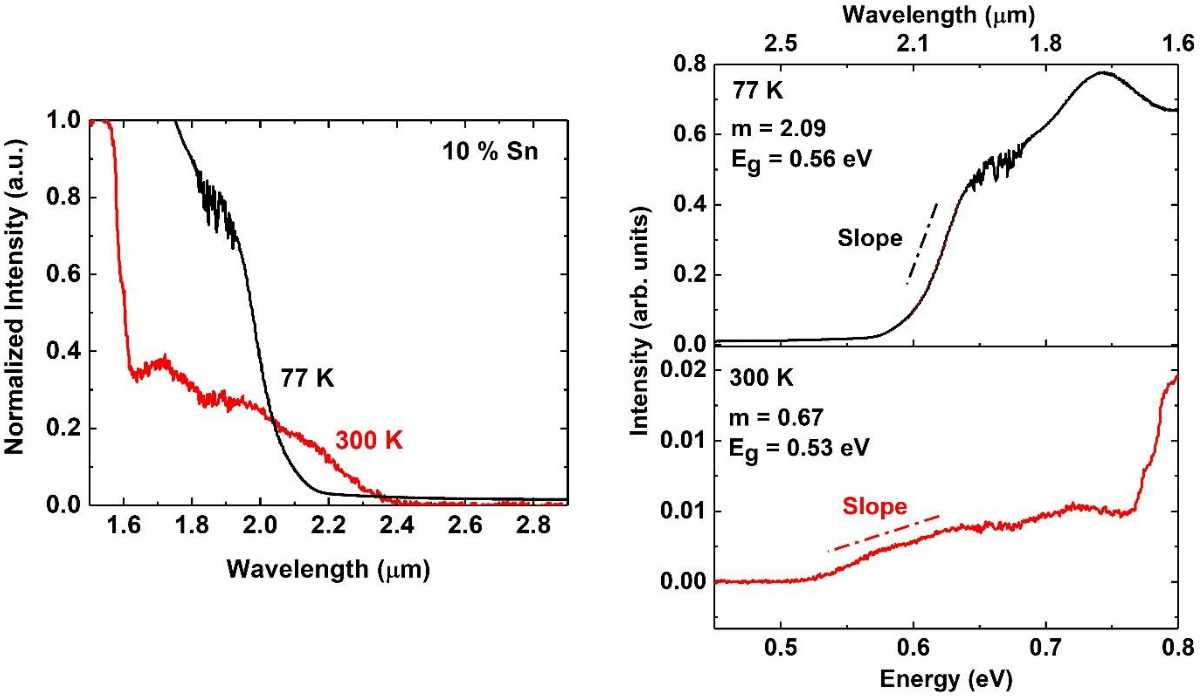

(a) (b)

Figure 8: (a) Normalized spectral response of 10 % Sn photoconductor at 77 and 300 K. (b): Slope and bandgap fitting of spectral response at 77 and 300 K.

2.4 Responsivity and Specific Detectivity D*

Responsivity is an important figure of merit of photodetector. It measures the change in the current per incident light power. The incident light that was used in this experiment is 1.55 µm laser with a spot size of 1 mm in diameter and with calibrated power. Detailed measurement technique of responsivity is discussed in Appendix.

Figure 9 plots responsivity versus voltage bias of 10 % Sn photoconductors with 12-24 interdigitated electrodes (IEPD) and photoconductor without interdigitated electrodes (Standard PD) at 300 K. Regardless of device structures, as the applied voltage increases, the responsivity increases. This could be explained as follow: the responsivity is proportional to the photoconductive gain which is expressed as a ratio of carrier lifetime over carrier transit time. Based on equation (10), carrier transit time is reduced as higher voltage bias is applied, resulting in an enhance in photoconductive gain and responsivity.

A responsivity of 0.27 A/W was measured at 10 V applied bias from a 0.5x0.5 mm^2 12-24 IEPD device. The obtained responsivity from IEPD device shows an enhance of 6.2 comparing with standard PD device at same applied bias while it is only 3-4 times less than the one of commercially available Ge and Extended-InGaAs detectors. High obtained responsivity from IEPD device is as expected since the introduction of interdigitated electrodes reduce the transit time of carrier and consequently contributes to the improvement of photoconductive gain. As the applied voltage keeps increasing, responsivity of IEPD devices starts saturating. The saturation behavior is caused by the minority carrier sweep-out effect that occurs when the photoconductive gain is equal or less than unity. This might suggest that the carrier effective lifetime becomes smaller than the carrier transit time, which enables the formation of a built-in space charge region around the metal contacts that causes repulsion of carriers.

With such improvement in responsivity comparing with standard PD, temperature dependent responsivity of 12-24 IEPD was investigated. The responsivity of 12-24 IEPD in Figure 10 shows a significant enhancement with decreasing temperatures. A maximum responsivity of 2.85 A/W under 5 V bias at 77 K and 1.55 μm was achieved, which is 75% higher than our previous study on a PD in Ref. [47] with lower applied bias and three times that from commercially available InGaAs photovoltaic detectors. This dramatically increased responsivity can be explained as follows: as temperature decreases, the activated background carrier concentration is reduced while the effective carrier lifetime increases, resulting in a higher photoconductive gain at low temperature. Note that for the commercial photodiode detectors, normally there is no significant change in responsivity as temperature decreases. It is worth pointing out that, at low temperatures, the responsivity value starts to saturate at 3 V and decreases beyond 5 V applied bias. This saturation behavior was explained above.

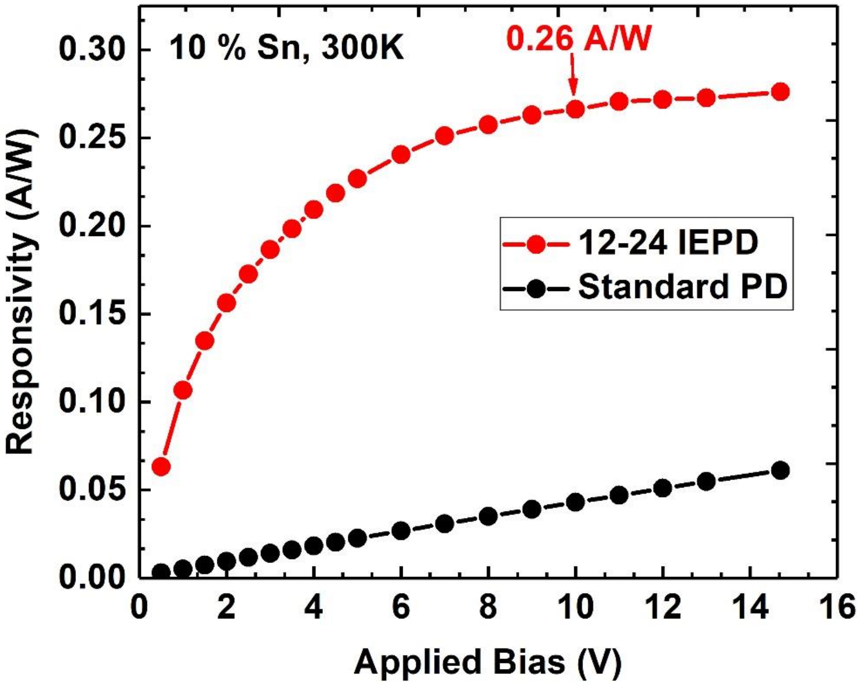

Figure 9: Responsivity versus voltage bias at 300 K of 10 % Sn standard PD and 12-24 IEPD.

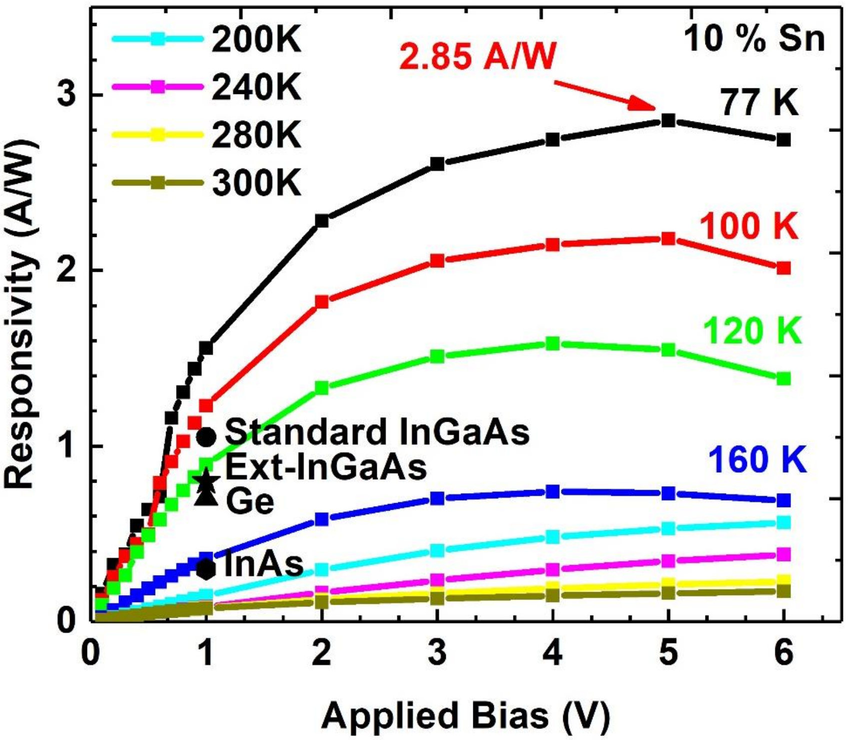

Figure 10: Temperature dependent responsivity of 12-24 IEPD with 10 % Sn from 77 to 300 K. Other market dominating infrared detectors are plotted for comparison.

Specific detectivity D* is another important figure of merit to directly compare individual detector. According to equation (18), D* can be calculated using noise current, responsivity, device area, and 1 Hz equivalent noise bandwidth. The noise current is estimated based on shot noise and thermal noise. Therefore, current-voltage characteristic of 10 % Sn photoconductor with 12-24 interdigitated electrodes was measured from 77 to 300 K. Linear behavior of I-V demonstrated that the metal contacts of photoconductors are Ohmic. The dark resistance was also extracted for each temperature in Figure 11. As the temperature decreases, the resistance increases as a result of the carrier frozen in the device.

For this set of devices wherein dark current is large, the shot noise dominates others noise mechanisms. As applied voltage increases, the noise current increases with a factor of √V while the responsivity saturates. Although the responsivity is enhanced at low temperature, it cannot compensate for the increasing noise current at high applied voltage. Therefore, the D* decreases after a certain applied voltage. At 77 K, the peak D* value of 3.95x10^9 cm*$Hz^{1/2}$*W^{-1} was observed at 1V, as shown in Figure 12.

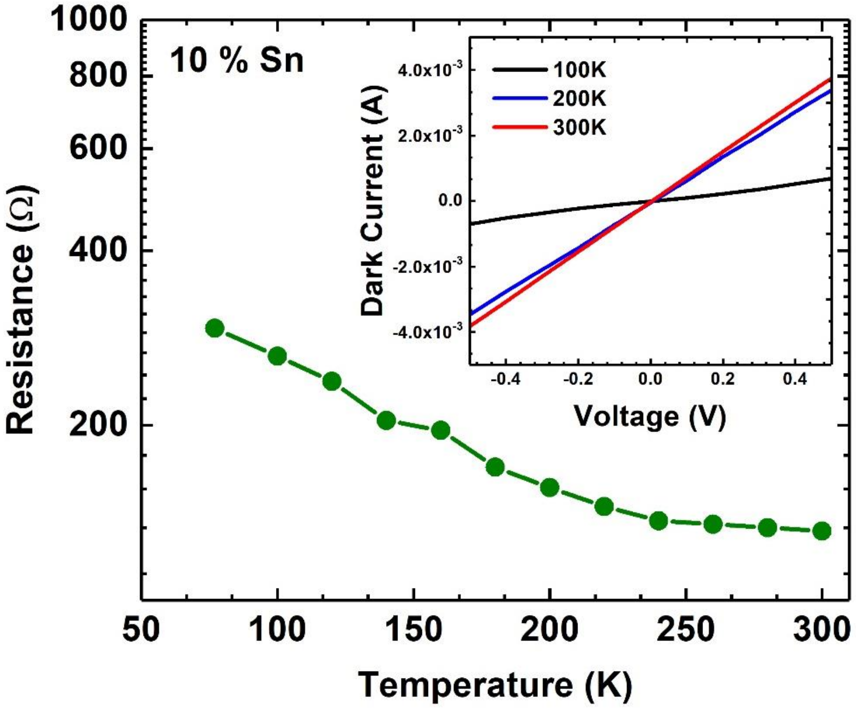

Figure 11: Extracted resistance from 77 to 300 K of 10 % Sn photoconductor. Inset: Voltage-dark current characteristic at 100, 200, and 300 K of 10 % Sn photoconductor .

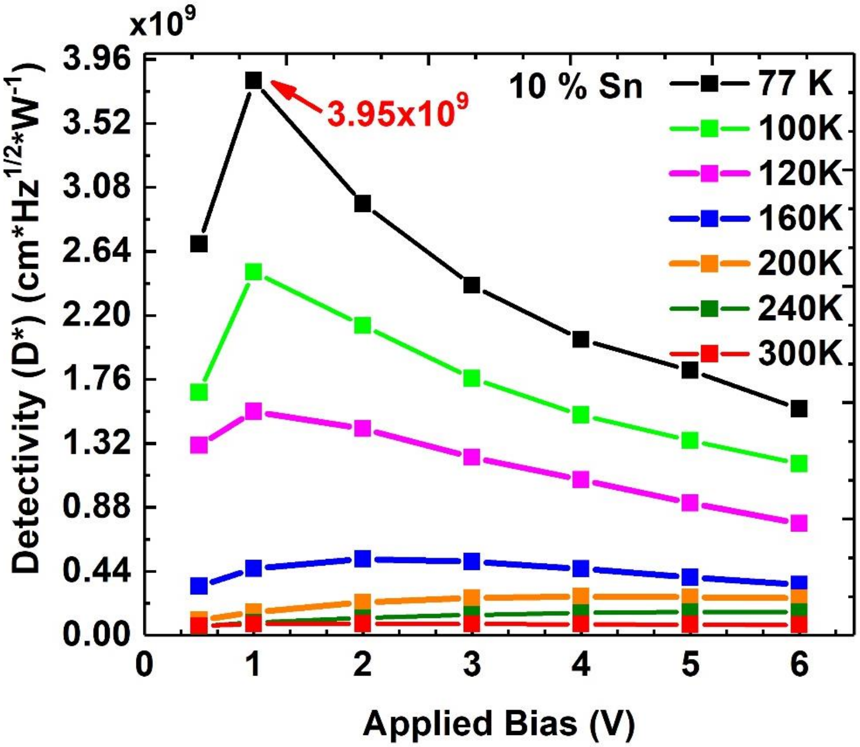

Figure 12: Temperature dependent specific detectivity D* of 12-24 IEPD with 10 % Sn from 77 to 300 K.

2.5 Spectral detectivity

The spectral detectivity of the 10 % Sn IEPD at 77 and 300 K is plotted together with market dominating infrared detectors such as Ge, InGaAs, extended-InGaAs, PbS, and InAs for comparison in Figure 13. The absorption edge of spectral response at 300 K is 2.4 μm and blue shifts to 2.2 μm with the decreasing temperature. The D* reported in this study is only one or two orders of magnitude lower than these mature detectors in the SWIR range. Although the responsivity of 10 % Sn IEPD achieves 2.85 A/W, which is two to three times enhance than that of mature detectors listed above, the higher dark current in 10 % Sn IEPD reduces the overall value of D*. In order to improve D* value of GeSn photoconductors and compete with commercially available FPAs in the SWIR, a decrease in the dark current together with an increase in responsivity are required. It could be done by reducing the defects and background doping during material growth and by growing a thicker GeSn active layer. It is worth to note that the current active layer thickness of 10 % Sn IEPD is only around 100 nm.

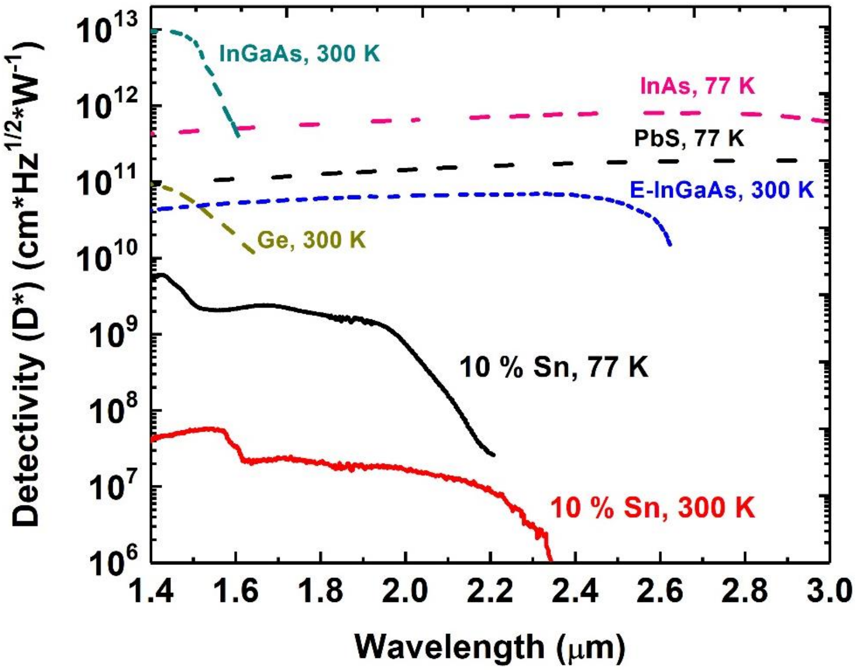

Figure 13: Spectral D* of thin film 10 % Sn photoconductor at 77 and 300 K.

Chapter 3: Systematic Study of thick film Ge1-xSnx Photoconductors

The performance of $Ge_{0.9}Sn_{0.1}$ photoconductors presented in chapter 2 was limited by: (1) the thin absorption layer of 100 nm, which results in a short cut-off wavelength of 2.4 µm at 300 K and a peak responsivity of 2.85 A/W despite of the gain enhancement from interdigitated electrodes structures; (2) the low tin composition of 10 % (nominal) that contributes in the short cut-off wavelength; (3) a high dark current that is possibly originated from the defective GeSn / Ge layers and the lack of effective surface passivation technique. Thanks to the recent breakthrough in growth technique using CVD system, better GeSn material quality has been achieved with higher Sn composition up to 22 % and thicker GeSn absorption layer up to 1.0 µm. This enabled a new systematic study of high Sn composition and thick film GeSn photoconductors. In this chapter 3, a set of samples with Sn composition ranging from 11 to 22 % and with thickness of 500-1000 nm will be presented. Mesas size of 0.5 and 1.0 mm were fabricated into photoconductor devices with and without interdigitated electrodes (width of 12 µm and spacing of 24 µm). Temperature dependent dark current-voltage, spectral response, and responsivity were measured.

3.1 Thick film $Ge_{1-x}Sn_x$ photoconductors growth and structures

In general, a higher Sn composition that is more than 10 % Sn is preferred to extend the cut-off wavelength of a photodetector to mid-IR range. Such high Sn incorporation enables bandgap reduction and hence prolongs the detection range of GeSn photodetector. Although significant progress of material growth using CVD system has been made recently, it has reached a threshold of ~ 15 % Sn regardless of precursor choice and recipe. In the recent work, the compressive strain was discovered as the main limiting factor of Sn incorporation rather than the chemical reaction [23], [79]. When GeSn is grown on a Ge buffer using a nominal 9 % GeH4 based recipe, a distinct two-layer structure was formed as follow: (1) As the growth starts, the first layer being defective is gradually relaxed and has 9 % Sn incorporation; (2) the second layer being low-defect density changes to 12 % Sn without changing the growth recipe. This specific growth mechanism is called spontaneous-relaxation-enhanced (SRE) process that inspires a new set of GeSn photoconductors with Sn composition up to 22 % and with a thickness ranging from 500-1000 nm. Those samples could be divided in two groups where the first group employed the SRE approach which results in two-layer structure with 16 % Sn and the second group used GeSn virtual substrate approach which leads to three-layer structure with 22 % Sn. The GeSn virtual substrate method is a continuous growth using the two-layer GeSn structure obtained from the SRE process to achieve higher Sn composition.

In this chapter 3, GeSn samples were grown using an industry-standard ASM Epsilon® 2000 PLUS reduced pressure chemical vapor deposition (RPCVD) reactor. The transmission electron microscopy (TEM), the Secondary Ion Mass Spectrometry, X-ray diffraction (XRD) 2θ-ω scan, and reciprocal space mapping (RSM) were used to determine the layer thickness, the Sn compositions and strain. The Ge buffer layer thickness is around 600 nm and the defective layer thickness ranges from 200 to 400 nm. As the Sn is gradually increases, average Sn composition is used for convenience. Table 2 summarizes samples information including the total thickness of GeSn layer, the maximum Sn composition, and the strain of layer having the highest Sn composition [80]. The first three samples, ASM 108 – 116 -112 have with two-layer structure while samples ASM 118 – 128 – 129 is composed of three-layer structure. TEM images of sample ASM 116 and ASM 118 are shown in Figure 14 as examples of two and three-layer structure [23]. It is worth to note that sample ASM 128 has achieved the highest Sn composition which surpasses the record of Sn incorporation growth by using CVD reactor with GeH_4 recipe (12%) and Ge_2H_6

recipe (15%). With such high Sn incorporation and GeSn absorption layer thickness, longer cut-off wavelength extended to mid-IR and high responsivity could be realized.

Table 2: GeSn layer thickness, maximum Sn composition and strain of the layer having highest Sn composition

Sample	GeSn thickness (nm)	The maximum Sn content (%)	Strain (%)
0108-ASM	840	11.4	-0.14
0116-ASM	920	14.4	-0.39
0112-ASM	660	15.9	-0.29
0118-ASM	1120	17.5	-0.38
0128-ASM	1210	22.3	-0.61
0129-ASM	1420	20.0	-0.52

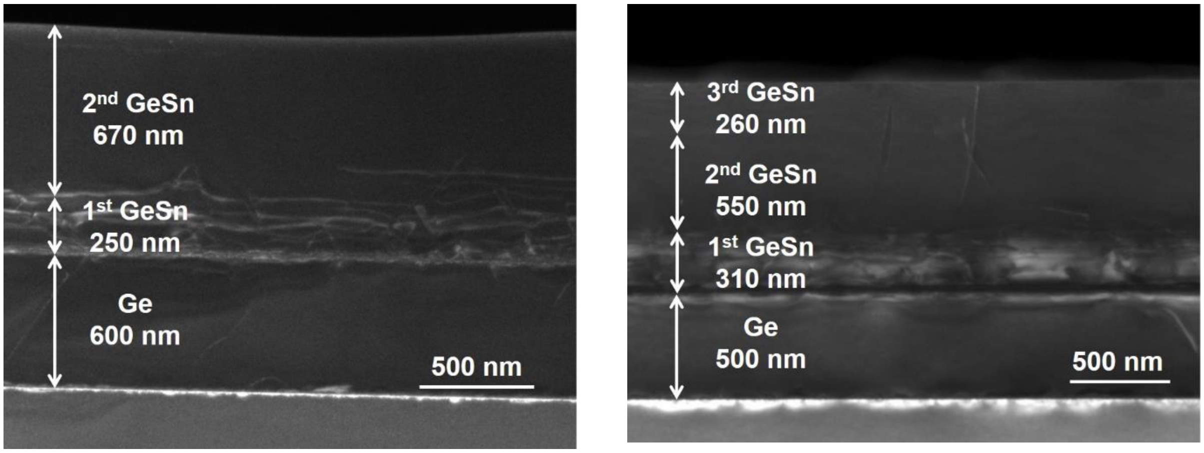

(a) (b)

Figure 14: TEM image of (a) 2-layer-structure with a maximum Sn composition of 14.4 % and (b) 3-layer-structure with a maximum Sn composition of 17.5 % [23].

3.2 Device fabrication process

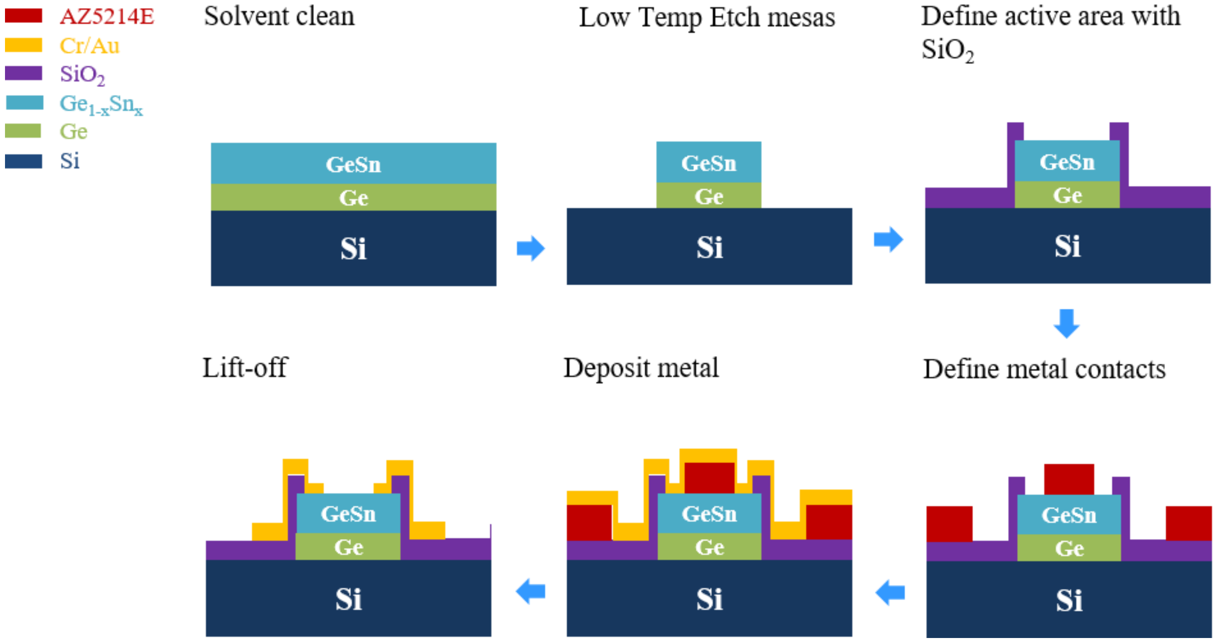

Figure 15: Fabrication process flow of thick film Ge$_{1-x}$Sn$_x$ photoconductors with interdigitated structures using SiO$_2$ as dielectric layer

Figure 15 presents the fabrication process flow of thick film Ge$_{1-x}$Sn$_x$ photoconductors. It has six major steps which are similar with the one of thin film photoconductor. The most significant change is the etching method due to the increase of Sn composition and thickness of the GeSn absorption layer. Such change leads to the modification of dielectric layer and metal deposition process. In addition, SiO$_2$ deposited by PECVD system was selected to replace BCB polymer due to the ease of process with no exposure to high temperature for long time.

After going through the cleaning process, square mesas of 500 x 500 µm^2 were defined by using photolithography. The photoresist thickness is around 1.7 µm after hard baking process at 130^o C for 15 mins. The etching target is to reach Si substrate to eliminate the contribution of Ge background to the responsivity measurement. This results in an etching depth of 1500 to 2000 nm. At first, a wet chemical solution of HCl: H$_2$O$_2$: H$_2$O = 1:1:10 was performed at room temperature. However, severe lateral etching was observed and the photoresist as the stopping mask was removed after 30 minutes. Therefore, low temperature wet etching was studied and performed. The low temperature wet etching will reduce the activities of molecules; hence smoother mesas side walls could be obtained as shown in Figure 16 (a). Since those six samples contain multiple layer of grading GeSn on a Ge buffer, the etching depth will be presented in Table 3.

A wet chemical etching solution of HCl: H_2O_2: H_2O = 1:1:10 was prepared in a beaker which was surrounded by ice to reach 0^o C. The etching temperature of samples ASM 108 – 112 – 116 was strictly maintained at 0^o C for the whole etching time presented in Table 3. In contrast, the etching process of samples ASM 118 – 128 - 129 was divided into two steps: the temperature was kept at 0^o C for the first 60 minutes and was later increased to 2-3^o C until a blue dark color was observed. This indicated that Si layer was reached. It is recommended to perform dry etching with Chlorine based gas for samples having a thick GeSn absorption layer (more than 1.5 µm).

Table 3: Etching time at 0^o and 2^o C and corresponding etching depth of different Sn composition samples

Sample	Etching time @ 0^o C (min)	Etching time @ 2^o C (min)	Etching depth (µm)
0108-ASM	60	-	1.54
0116-ASM	65	-	1.73
0112-ASM	75	-	1.93
0118-ASM	60	13	1.87
0128-ASM	60	15	2.16
0129-ASM	60	17	2.7

After the wet etching process, samples were processed similar with those steps in chapter 2. The SiO_2 thickness to be deposited was adjusted to be 30-40 % of the etching depth. It is extremely difficult to balance the exposure dose during the exposure of small interdigitated electrodes on the top of the mesas due to the height difference between top and bottom. It is also important to note that only sample ASM 108 has a SiO_2 layer deposited by PECVD system, as shown in Figure 16 (b). The SiO_2 layer that was deposited on the other samples was done using

Electron-Beam Evaporator system. The fabrication process of those samples will be later clarified in Chapter 5. Figure 16 (c) and (d) show the final state of ASM 108 photoconductor with metalized interdigitated electrodes structures of 6-12 and 12-24 respectively.

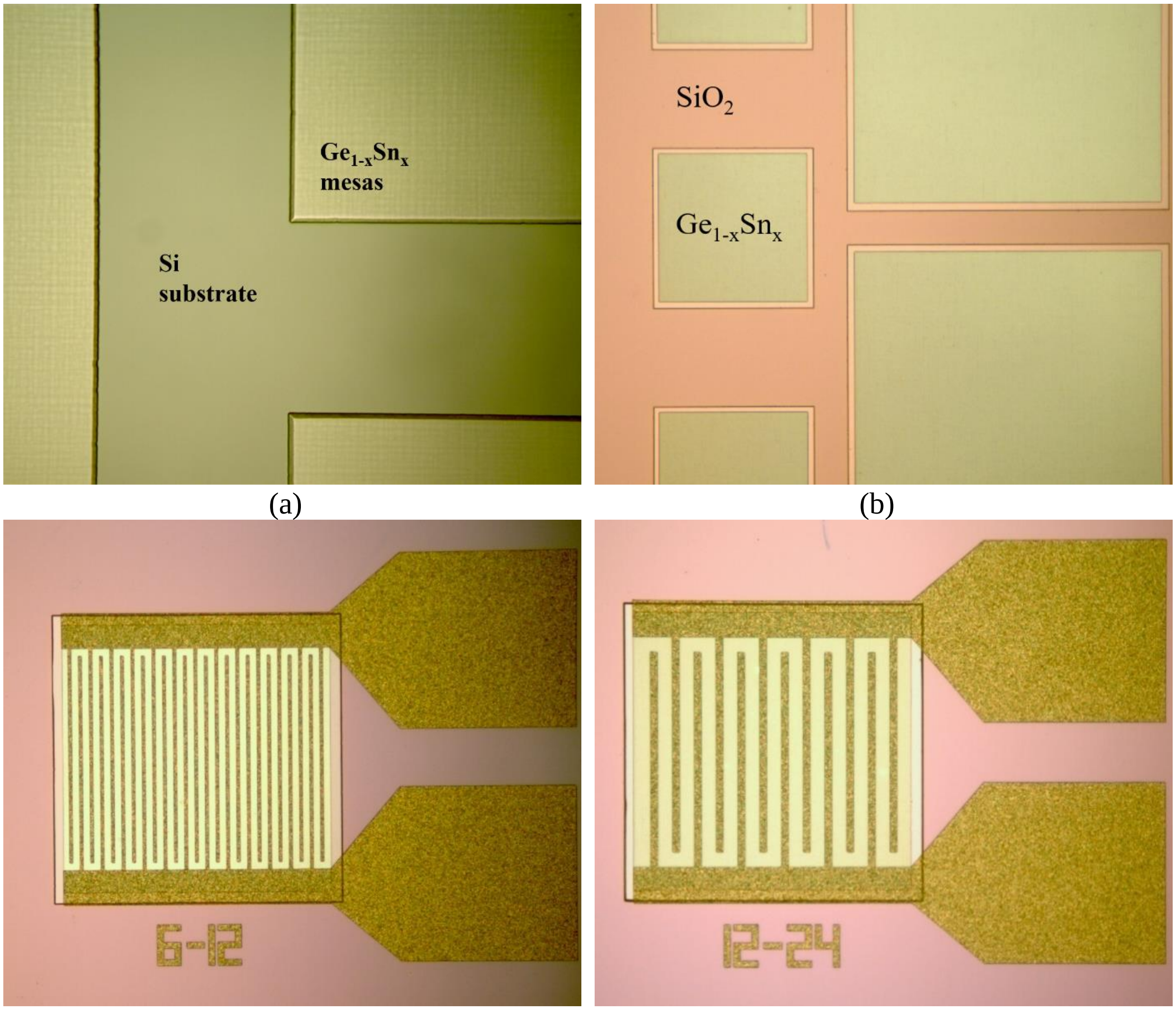

(a) (b)

(c) (d)

Figure 16: Top view microscope image of (a) ASM 108 after wet etching at low temperature, (b) ASM 108 after defining the active windows, (c) 500x500 μm^2 ASM 108 with 6-12 interdigitated electrodes structure after lift-off, and (d) 500x500 μm^2 ASM 108 with 12-24 interdigitated electrodes structure after lift-off

3.3 Spectral response

Spectral response of 11 %, 13 %, 16 %, 17.5 %, 20 %, and 22 % Sn photoconductors was measured from 77 to 300 K to determine the working range of thick film GeSn photodetectors.

Figure 17 presents the normalized spectra of the above photodetectors with 10 % cut-off at 300 K. The 11 % Sn sample has the shortest cut-off wavelength of around 3.0 µm. This has surpassed the one of 10 % Sn photoconductor reported in chapter 2. As Sn composition increases, the cut-off wavelength is extended to longer coverage due to the reduced bandgap. This is in agreement with the Vegard's law interpolation between Ge and Sn [77]. The wavelength is extended to around 4.0 µm using 20 and 22 % Sn samples. Although those two samples have a 2 % difference in Sn composition, their cut-off wavelength is similar. In fact, the Sn composition of ASM 129 was obtained from a single point on the wafer using SIMS measurement. Moreover, different bandgap was observed by measuring photoluminescence at other positions of the wafer, which suggests a non-uniformity of Sn composition is possible.

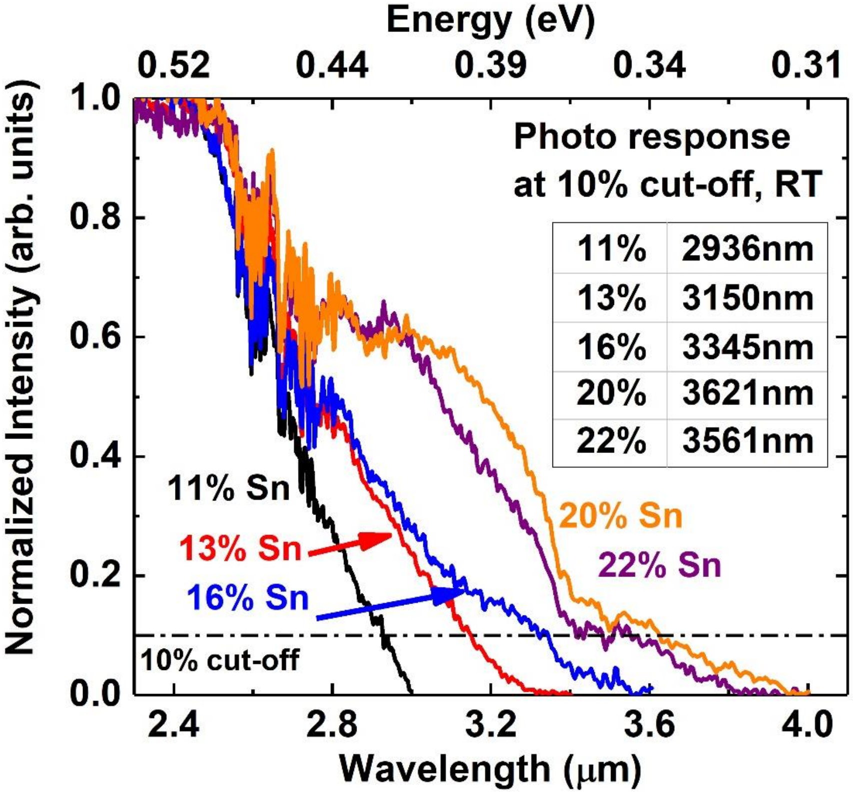

Figure 17: Normalized spectral response with 10 % cut-off wavelength of 11 %, 13 %, 16 %, 20 %, and 22 % Sn photoconductors measured at 300 K.

Temperature dependent spectral response of 11 %, 13 %, 16 %, 17.5 %, 20 %, and 22 % Sn photoconductors were plotted side by side and were normalized at 2.0 µm as shown in Figure 18 (a), (b), (c), (d), (e), and (f) respectively. As the temperature increases from 77 to 300 K, a red shift from 2.6 µm to 3.0 µm, 2.9 µm to 3.3 µm, 3.0 µm to 3.5 µm, 3.25 µm to 3.7 µm, 3.4 µm to 4.0 µm, 3.3 µm to 3.8 µm was observed for 11 %, 13 %, 16 %, 17.5 %, 20 %, and 22 % Sn samples. The long cut-off wavelength is far beyond 1.55 which is the band-to-band absorption edge of Ge. This suggests that the absorption is contributed from GeSn material. The distortion of signal at 2.6 – 2.8 µm that occurs for every temperature and samples is due to atmospheric absorption. The eruption of intensity beyond 3.2 was observed in samples with 16 %, 17.5 %, 20 %, and 22 % Sn. This is mainly due to existence of a thin SiO_2 layer that was not completely removed during the fabrication process of GeSn photoconductor devices with passivation. Sample with 13 % Sn was not affected because of its short cut-off wavelength below 3.2 µm while sample with 11 % Sn was not included in this fabrication batch.

The bandgap near the absorption edge can be evaluated by fitting photon energy versus spectral response intensity as presented in chapter 2. The fitting bandgap reduces as the Sn composition increases. However, the one of 20 % and 22 % Sn, found in Table 4, is both close to 0.31 eV, which once again confirms the non-uniformity of Sn composition of sample 20 % Sn.

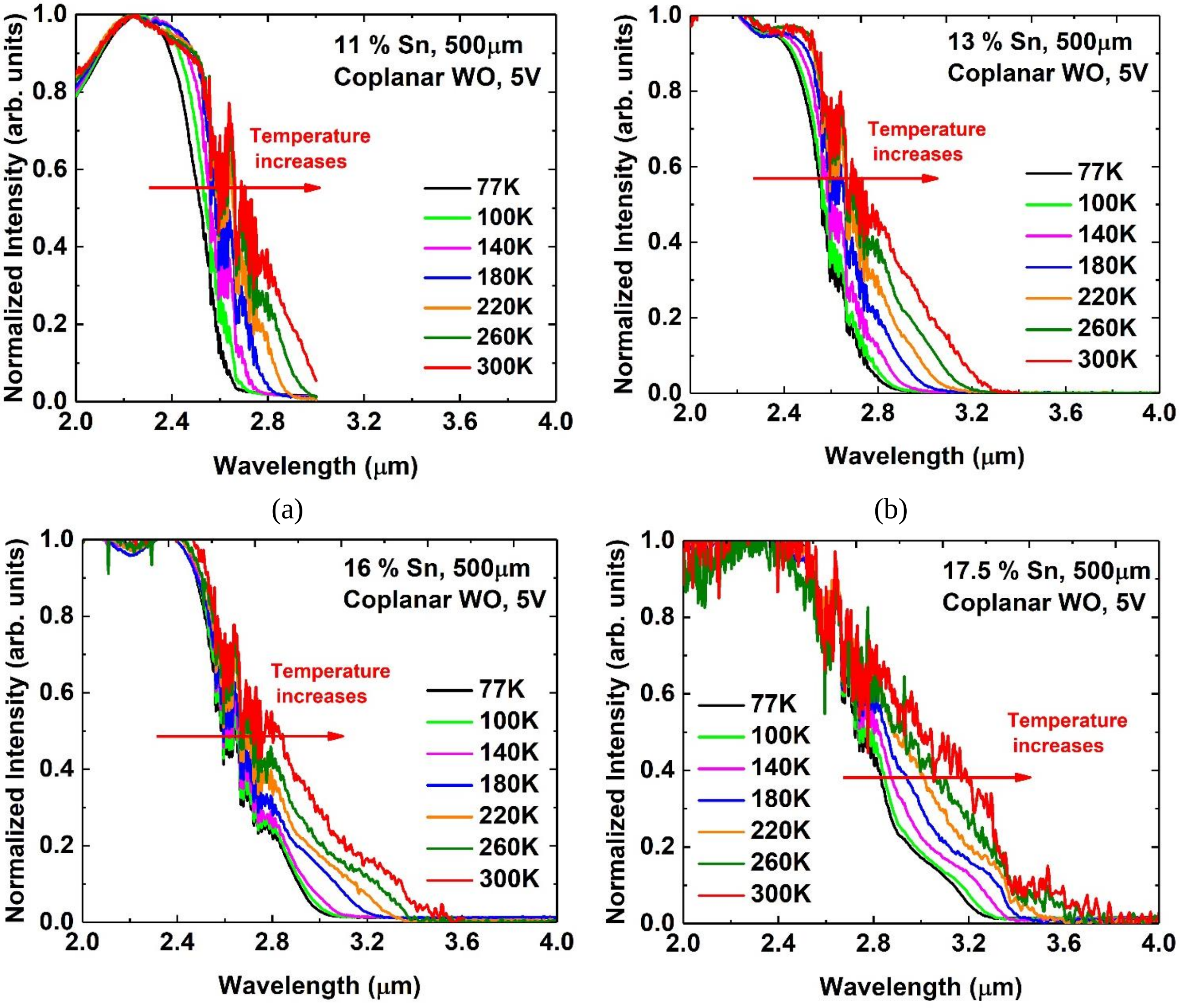

(a) (b)

(c) (d)

Figure 18: Normalized temperature dependent spectral response of 500 µm coplanar photoconductor with a nominal Sn composition of (a) 11 %, (b) 13 %, (c) 16 %, (d) 17.5 %, (e) 20 %, and (f) 22 %.

Figure 18 (Cont.)

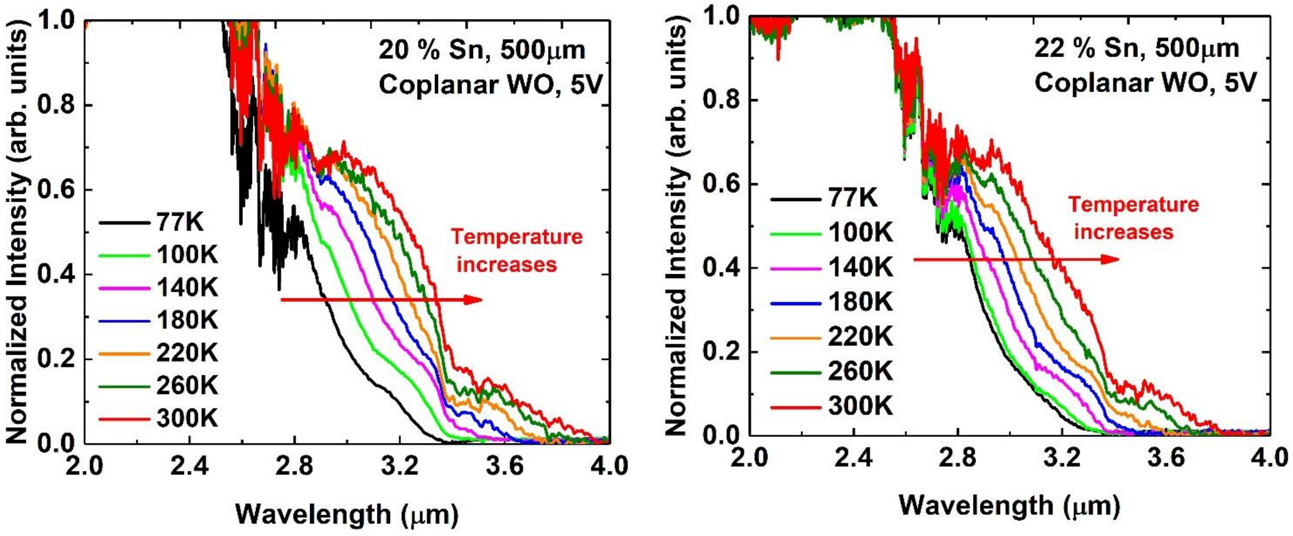

(e) (f)

Table 4: Extracted bandgap using spectral response intensity of 11 %, 13 %, 16 %, 17.5 %, 20 %, and 22 % Sn photoconductors

	11 % Sn ASM 108	13 % Sn ASM 116	16 % Sn ASM 112	17.5 % Sn ASM 118	20 % Sn ASM 129	22 % Sn ASM 128
E_g (eV)	0.41	0.38	0.34	0.32	0.31	0.31

3.4 Responsivity and Specific Detectivity D*

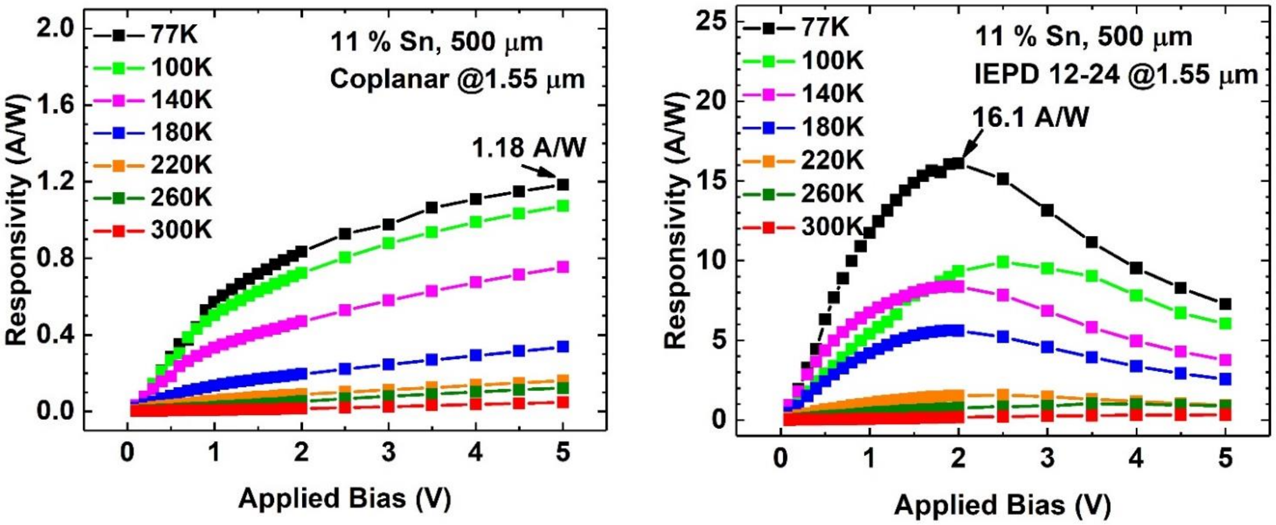

(a) (b)

Figure 19: Temperature dependent responsivity of (a) 11 % Sn coplanar photoconductor and (b) 11 % Sn IEPD 12-24 measured at 1.55 µm.

The responsivity of 11 % Sn photoconductor was first characterized from 77 to 300 K by using a 1.55 µm laser source with a power density of 0.4 mW/cm^2. The beam spot was estimated to be larger than the parameter of the 500×500 μm^2 mesas. Since 1.55 µm laser source was used, it is worth to notice the contribution of Ge in the final responsivity of the device, which results in a larger responsivity. This contribution is originated from the Ge buffer layer since Ge areas surrounding the mesas were completely removed during the wet etching process. Later batch of GeSn devices were measured at 2.0 µm to eliminate the contribution factor from Ge buffer layer.

Figure 19 (a) and 6 (b) presents the temperature dependent responsivity of 11 % Sn photoconductor with coplanar structure and 12-24 µm interdigitated electrodes structures. The responsivity of the devices in Figure 6 shows a significant enhancement with decreasing temperatures. This dramatically increased responsivity can be explained as follows: as temperature decreases, the activated background carrier concentration is reduced while the effective carrier lifetime increases, resulting in a higher photoconductive gain at low temperature. A peak responsivity of 1.18 A/W and 16.1 A/W was obtained at 5 V (77 K coplanar) and 2 V (77 K IEPD), respectively. The IEPD structure reduces the transit time, hence improves the photoconductive gain and results in higher responsivity. This peak responsivity of 16.1 A/W is the world record value of GeSn photoconductor at this time and is six times higher than our previous thin photoconductors because of thicker high-quality GeSn active layer, which enhances photons absorption rate. Note that for the commercial photodiode detectors, normally there is no significant change in responsivity as temperature decreases. The responsivity of IEPD devices decreases as the applied voltage over 2 V at low temperatures. This behavior is explained by the minority carrier (electron) transit time becoming shorter than the effective lifetime, which enables the formation of a built-in space charge region around the metal contacts to cause repulsion of carriers.

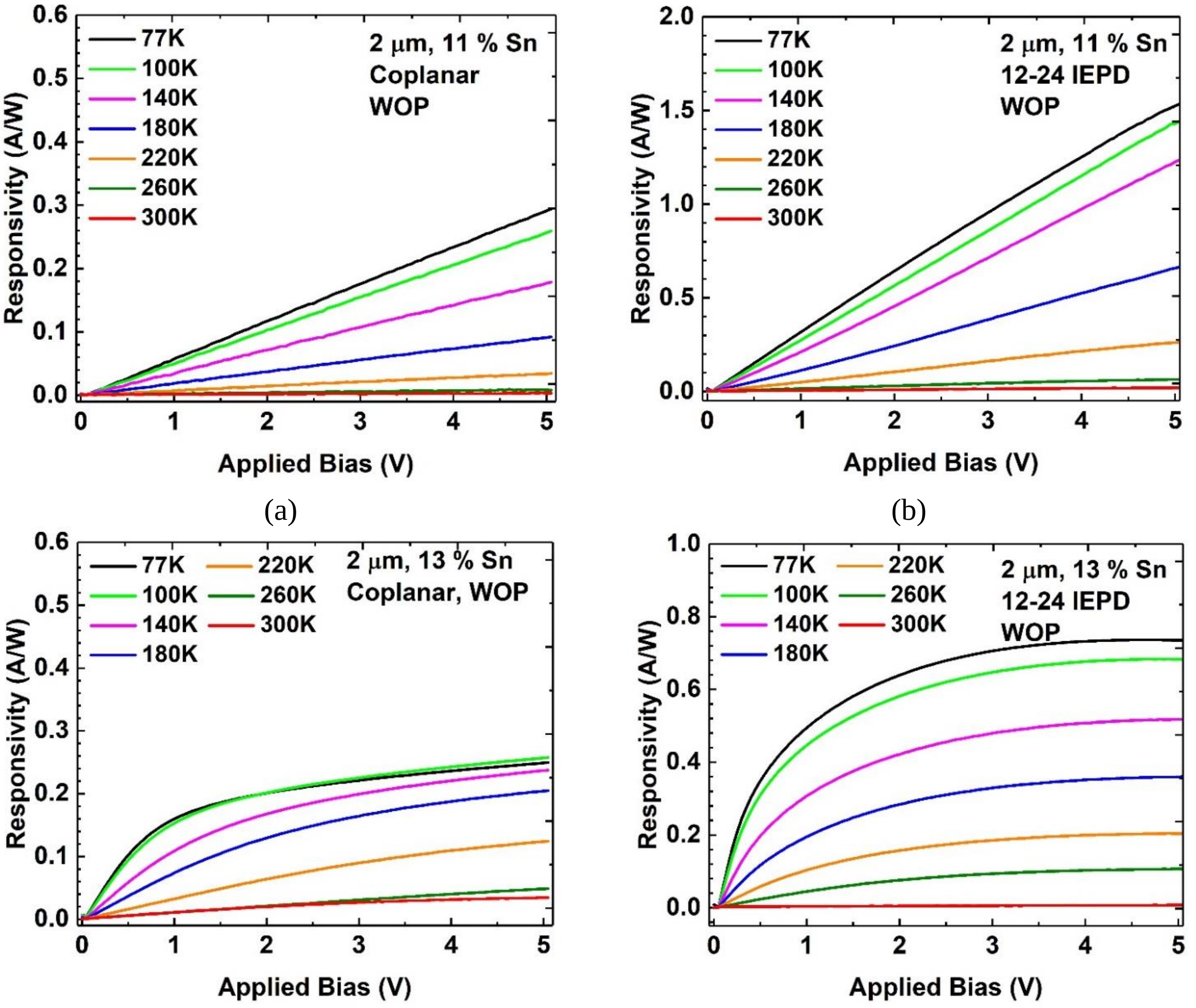

(a) (b)

(c) (d)

Figure 20: Temperature dependent responsivity of coplanar structure with (a) 11 % Sn, (c) 13 % Sn, (e) 16 % Sn, (g) 17.5 % Sn, (i) 20 % Sn, and (k) 22 % Sn and 12-24 interdigitated electrodes structure with (b) 11 % Sn, (d) 13 % Sn, (f) 16 % Sn, (h) 17.5 % Sn, and (j) 20 % Sn measured at 2.0 µm.

Figure 20 (Cont.)

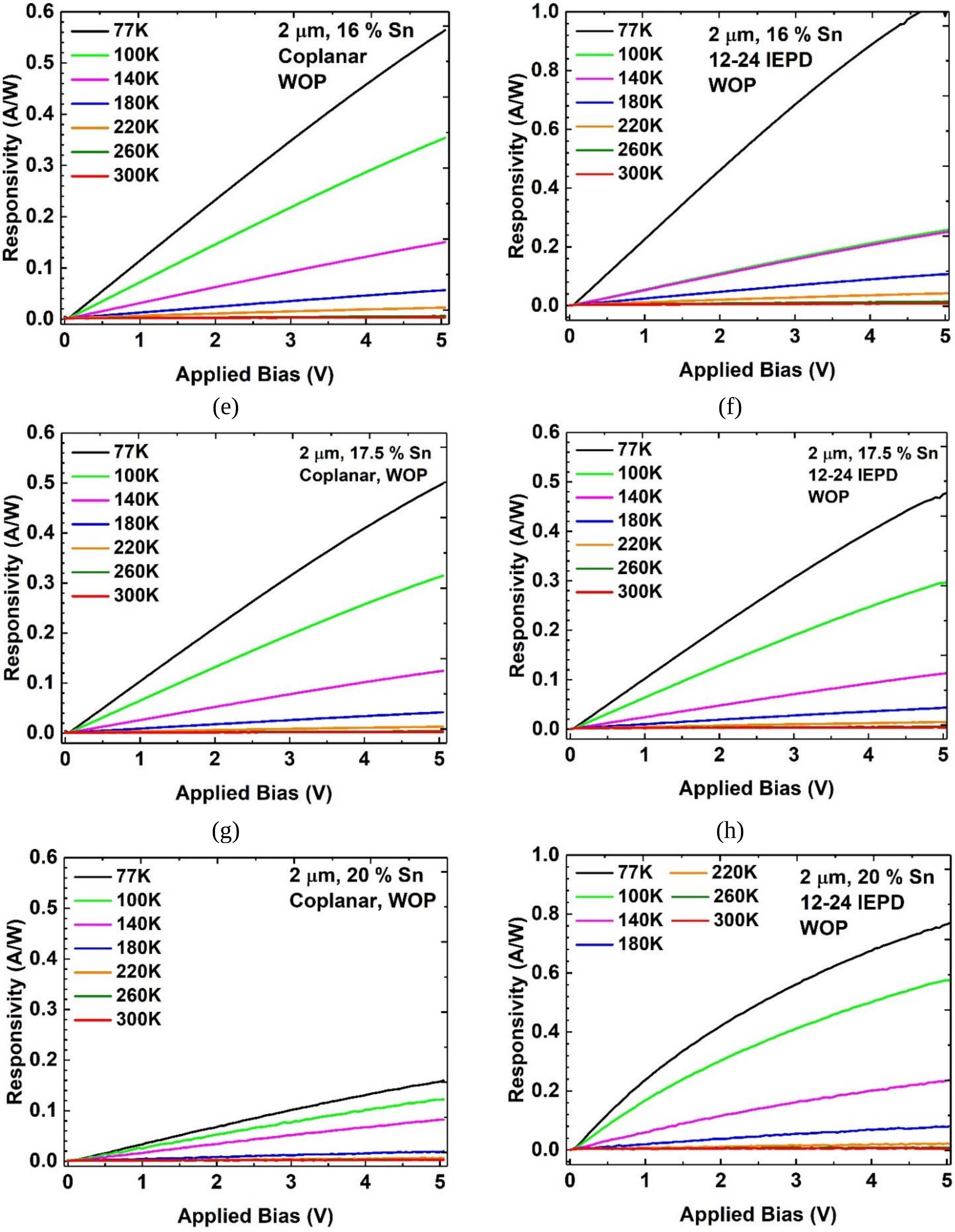

(e) (f)

(g) (h)

(i) (j)

Figure 20 (Cont.)

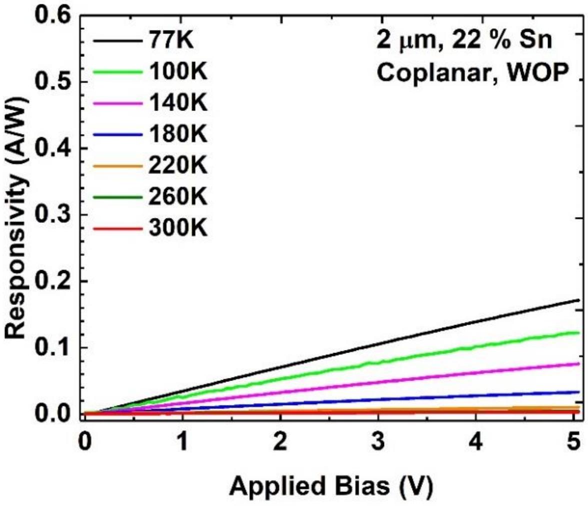

(k)

To eliminate the effect of Ge buffer layer, responsivity of GeSn photoconductors with and without interdigitated electrodes of 11 %, 13 %, 16 %, 17.5 %, 20 %, and 22 % Sn were measured at 2.0 µm, as shown in Figures 20. The fabrication process of those devices will be discussed in the following chapter 5. The peak responsivity of 11 %, 13 %, 16 %, 17.5 %, 20 %, and 22 % Sn coplanar photoconductors measured at 2.0 um and 77 K was 0.29, 0.25, 0.56, 0.5, 0.16, and 0.17 A/W respectively. Thanks to the increase of photoconductive gain by using 12-24 interdigitated electrodes photoconductors (IEPD), the peak responsivity of 11 %, 13 %, and 20 % Sn was enhanced to 1.5, 0.73, and 0.77 A/W. However, the responsivity behavior the responsivity characteristic of 16 % and 17.5 % Sn samples with 12-24 IEPD is similar with the one of coplanar structure. This suggests that the12-24 IEPD devices act as coplanar structure and the electrodes were not fully in contact with GeSn active layer due to the existence of a thin layer SiO_2. This was confirmed by using XPS measurement for those samples. The 22 % Sn photoconductor only has coplanar structure.

Temperature dependent I-V characteristic of 11 %, 13 %, 16 %, 17.5 %, 20 %, and 22 % Sn photoconductors were measured to calculate the noise current and specific D*. Current density and shunt resistance was also extracted at 77 and 300 K in Table 5. The current density of 11 % Sn photoconductor is 8 times less than the one of 13 % Sn at 77 K and is 21 times less than the photoconductor incorporated with highest Sn %, 22 % Sn, at 77 K. It is expected that 22 % Sn sample would have highest shot noise and thermal noise due to owning highest dark current and lowest shunt resistance. The specific D* would be reduced by RMS noise current value, which is the sum of shot noise and thermal noise.

Table 5: Current density measured at 77 and 300 K and shunt resistance extracted at 77 and 300 K.

Devices	Current density @ 1 V (A/cm^2)		Shunt resistance (Ω)	
	77 K	300 K	77 K	300 K
11 % Sn, CP	0.05	1.1	10100	694
11 % Sn, IEPD 12-24	2.2	8.6	240	51
13 % Sn, CP	0.4	0.85	1811	658
13 % Sn, IEPD 12-24	11.4	19.5	37	21
16 % Sn, CP	0.5	1.2	840	309
16 % Sn, IEPD 12-24	30	26.8	13	19
17.5 % Sn, CP	0.72	1.16	556	333
17.5 % Sn, IEPD 12-24	39	33	10	12
20 % Sn, CP	0.94	1.5	426	259
20 % Sn, IEPD 12-24	29	32	14.2	12.5
22 % Sn, CP	1.03	1.88	389	209

Although growth technique has been gradually improved, GeSn photoconductor performance was not significantly improved and hindered by high dark current. Silvaco simulation was therefore performed based on the sample structure from TEM cross-section images, which typically is composed of a layer of high Sn composition laying on a defective layer of lower Sn composition, germanium buffers layers, and a silicon substrate. The defective layers were represented high carrier concentration of 10^{19} cm^{-3}. Figure 21 plots the current flow inside 11 %

Sn photoconductor. The current flow is not evenly distributed and remains mostly in layers with high carrier concentration or defective layers. This is the main reason besides the fact that effective surface passivation method was not applied, causing high dark current in photoconductor. By removing those layers, GeSn photoconductor D* is believed to be improved. The cutoff wavelength of the spectral response will be further extended due to relaxation of the GeSn film. On the other hand, the measured photodetector characteristic of substrate removal sample will come directly from GeSn film. This is a milestone in the study of GeSn material system. The fabrication process will be discussed in future work section of chapter 7.

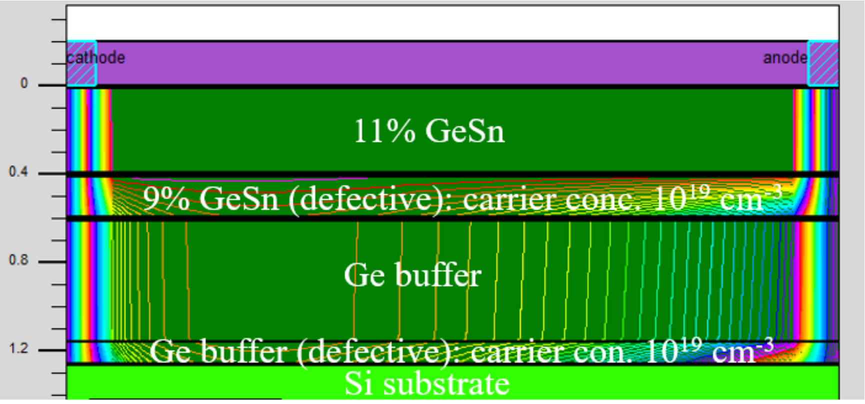

Figure 21: Current flow simulation of 11 % Sn photoconductor using Silvaco.

The specific D* was first calculated using noise current, responsivity, device area, and 1 Hz equivalent noise bandwidth. It was later used to plot spectral D* for 11 %, 13 %, 16 %, 17.5 %, 20 %, and 22 % Sn photoconductors at 77 K (Figure 22 (a)) and 300 K (Figure 22 (b)). Commercially available detectors such as InGaAs, InAs, PbS, Ext-InGaAs were plotted together as a baseline to achieve and surpass in future. In summary, the performance at 77 K of 11 % Sn photoconductor is only 3-4 times less than the one of Ext-InGaAs. As Sn composition increases from 11 % to 22 % Sn, the detection range was extended from SWIR range to mid-IR range up to 4.0 μm at 300 K.

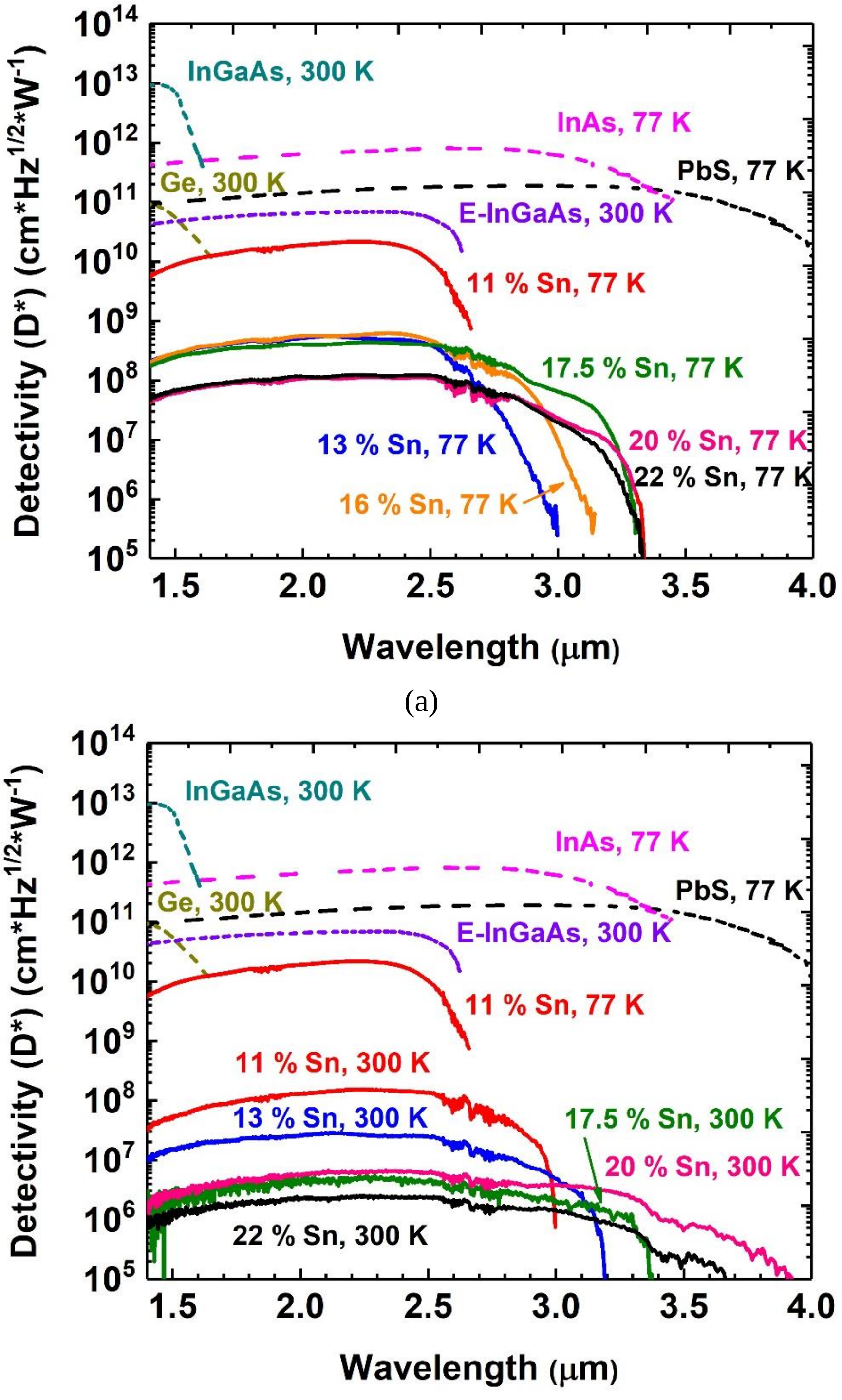

(a)

(b)

Figure 22: Spectral detectivity of 11 %, 13 %, 16 %, 17.5 %, 20 %, and 22 % Sn photoconductors was plotted at (a) 77 K and (b) 300 K in comparison with commercially available detectors.

Chapter 4: Development of $Ge_{1-x}Sn_x$ Photodiodes

The last two chapters, chapter two and chapter three, revealed a comprehensive study of thin film and thick film GeSn photoconductors. The responsivity of GeSn photoconductor was improved by implementing a thicker active GeSn layer with less defects while the cut-off wavelength was extended to mid-infrared range by increasing Sn composition up to 22 %. This chapter four will investigate another type of photodetector which is a double heterostructure photodiode (DHS) Ge / $Ge_{1-x}Sn_x$ / Ge. The $Ge_{1-x}Sn_x$ i-layer is grown on top of n-type Ge buffer on Si substrate and covered by a thin p-type Ge cap layer. The first photodiode design with a nominal Sn composition of 7 and 10 % defines a baseline of GeSn photodiode while the later one with more optimized structure and better growth technique reveals its capability and potentials for SWIR to MIR photodetection.

For the first-generation photodiode, 10 % Sn sample with an i-layer of 250 nm thick has a cut-off wavelength up to 2.3 and 2.6 µm at 77 and 300 K. A peak responsivity of 0.19 A/W under -0.1 V bias at 300 K was observed and reduced to 0.07 A/W as the applied voltage increased to -1 V. A D* of 2.4×10^9 Jones (10 % Sn) and 4×10^9 Jones (7% Sn) at 1.55 µm was calculated respectively. However, the performance of that device is limited by following factors: (1) the thin GeSn active layer (~ 250 nm) that results in low responsivity, (2) the short cut-off wavelength due to compressive strain, (3) the short depletion region, because of high doping junction (~ 10^{19} cm^{-3}), that enables high dark current (25 mA/cm^2 at -0.1V) and poor carrier collection. Moreover, the device responsivity was over estimated with a contribution from Ge buffer as it was measured using a 1.55 µm laser source.

In order to address the above issues, a newly designed photodiode structure together with newly developed growth technique [23], [65], [66] have been implemented. Details structure will be further discussed in the following section 4.2. The cut-off wavelength of 11 % Sn with a thick GeSn absorption layer of 700 nm is extended to 2.5 and 2.8 µm at 77 and 300 K due to thicker active layer and less compressive strain. The device shows a dark current density of 7.9 mA/cm^2 at 0.1 V. The room-temperature responsivity was measured as 0.34 A/W at 2 µm, corresponding to an external quantum efficiency (EQE) of 20 %. It is worth noting that since the responsivity was measured using a 2.0 µm laser, the contribution from the Ge buffer layer was mostly eliminated, leading to a more accurate characterization of the GeSn photodiode.

4.1 First generation $Ge_{1-x}Sn_x$ photodiodes

4.1.1 Material growth and device structure of GeSn photodiode

The GeSn DHS samples were grown using an ASM Epsilon® 2000-plus reduced- pressure chemical vapor deposition system. Figure 23 (a) illustrates the schematic cross-sectional view of the device structure, composed of a 750-nm-thick p-type Ge layer (also serving as the buffer layer), a 200-nm-thick unintentionally doped $Ge_{1-x}Sn_x$ active layer, and a 50-nm-thick n-type Ge cap layer. Since the unintentionally doped GeSn layer was measured to be slightly p-type doped, in order to achieve a good p-n junction, the doping concentrations for p-type and n-type Ge layers were chosen as 5×10^{18} and 1×10^{19} cm^{-3}, respectively. The relaxed p-type Ge layer was grown by a two-step growth method. Since the introduction of boron doping leads to the degradation of Ge seed layer quality, firstly an undoped 150 nm Ge seed layer was grown at < 400ºC in H_2 carrier gas using GeH_4 as precursor at the partial pressure of 0.2 torr. The temperature was then increased to 600 ºC at a ramp rate of 1 ºC/min while keeping the GeH_4 partial pressure, followed by the introduction of 1 % B_2H_6 as boron doping source once the temperature stabilized at 600 ºC. A post growth *in-situ* anneal was done at > 800 ºC, which reduced the threading dislocations and re-distributed the boron dopant more evenly across the entire p-type Ge layer.

The chamber was then cooled down to < 350 ºC in H_2 ambience for GeSn layer growth. The $SnCl_4$ and GeH_4 were used as Sn and Ge precursors, respectively. The $GeH_4/SnCl_4$ molar flow ratio varied between 0.95 and 0.99 depending on the target Ge/Sn composition. The H_2 was used as carrier gas at a flow rate of 15 slm. Finally, the 50-nm-thick n-type Ge layer was deposited at the same temperature to avoid Sn-precipitation. N_2 carrier gas was used to increase the Ge growth rate at the low growth temperature and 1% PH_3 was used as the phosphorous doping source. A detailed study of this growth method was reported elsewhere [63].

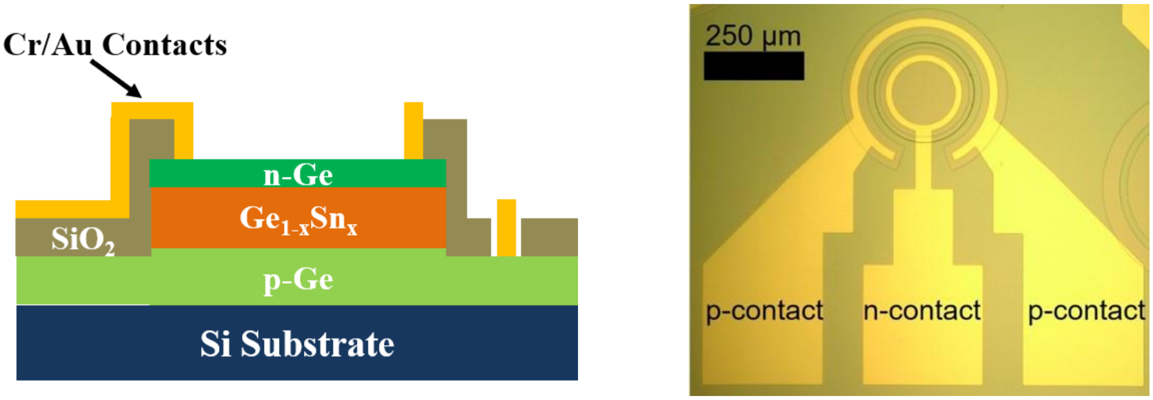

(a)

(b)

Figure 23 (a): Schematic cross-sectional view of the device structure. Figure 23 (b): Top view microscope image of 250 µm device.

The material quality, layer thickness, and strain of two samples presented in this study were characterized using transmission electron microscopy (TEM) and X-ray diffraction (XRD) techniques. TEM results show the high quality of grown material with defects trapped at Ge/Si interfaces due to the optimized growth of Ge buffer layer, leading to the low-defect GeSn active layer. The XRD-measured Sn compositions of 6.44 and 9.24 % are slightly lower than the targets of 7 and 10 %, respectively. Further analysis using two-theta omega scan (not shown here) reveals a clear single Ge$_{1-x}$Sn$_{x}$ peak for each sample, which suggests the high material quality. The Ge$_{0.9}$Sn$_{0.1}$ and Ge$_{0.93}$Sn$_{0.7}$ active layers exhibit the in-plane compressive strain of 0.48 and 0.33 %, respectively. The material characterization results are summarized in Table 6.

Table 6. Sn Composition, Thickness, and Strain for Each Layer.

Nominal Sn %	Measured Sn %	p-type Ge thickness (nm)	Ge$_{1-x}$Sn$_{x}$ thickness (nm)	n-type Ge thickness (nm)	Ge$_{1-x}$Sn$_{x}$ in-plane Strain
7.0	6.44	750	200	50	-0.43 %
10.0	9.24	750	200	50	-0.48 %

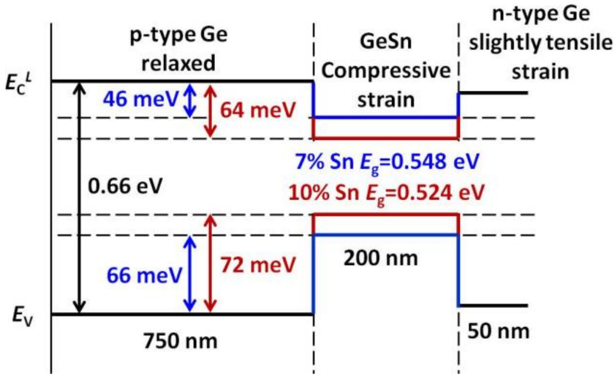

Figure 24: Ge/Ge$_{1-x}$Sn$_{x}$/Ge DHS band structure (not to scale). Type-I band alignment was formed, which provides a favorable carrier confinement for the device.

Based on our theoretical study, both GeSn layers with 7 and 10 % Sn compositions remain indirect bandgap due to the compressive strain (otherwise 10 % Sn could be the direct bandgap). Incorporation of Sn pushes down the Γ- and L-valley in the conduction band while lifts the valence band, therefore the type-I alignment of the Ge/Ge$_{1-x}$Sn$_{x}$/Ge DHS is achieved, which favorites the carrier confinement. The band structures of 7 and 10 % Sn samples are shown in Figure 24.

4.1.2 Device fabrication

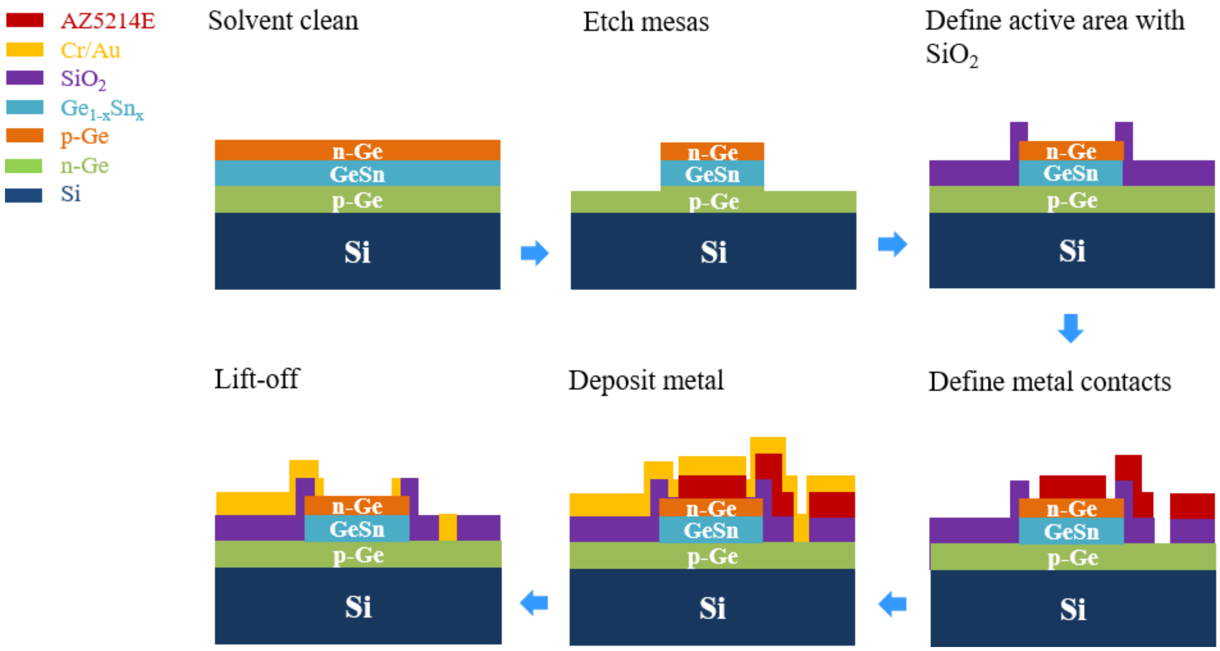

Figure 25: Fabrication process flow of first generation DHS GeSn photodiode with an absorption layer of 250 nm and with SiO_2 as dielectric layer

A 7 % and a 10 % Sn GeSn DHS were fabricated into photodiode devices with a top active area of 250 and 500 µm in diameter following the processing flow as shown in Figure 25. It was composed of six major steps which resembles of the fabrication process of thin film photoconductor presented in chapter 2. However, a wet etching method and another choice of dielectric layer were employed.

After cleaning with acetone / IPA / DI water, circular mesa structures with diameters of 250 and 500 µm were defined by photolithography. Wet chemical etching method was selected instead of RIE etch to have a better control on the etching depth with increasing Sn composition and active layer thickness. In addition, the byproducts generated from the reaction of CF_4 and Sn are not soluble and prevent further chemical reaction. Therefore, only physical sputtering process will occur and results in rough surface. In this section, the solution of $HCl:H_2O_2:H_2O = 1:1:20$ was used for the mesa etching. H_2O_2 acts as a strong oxidizer to form Ge-O which is soluble in aqueous solution while HCl continuously remove Sn particles by forming $SnCl_x$. Others wet etching solution such as $NH_4OH:H_2O_2:H2O$ = 1:2:160 [81], [82] and $H_2SO_4:H_2O_2:H_2O$ = 1:1:8 [83] has also showed success in etching GeSn material. In fact, wet chemical etching suffers from lateral etching to the sidewall of devices. Hence, dry etching with the use of chlorine base gas is more desired for future GeSn devices.

The etching depth was controlled to be 500 nm to expose the p-type Ge layer for metal contact. A stable etching rate of 100 nm/min at room temperature was observed with only a slight decrease as Sn composition increases. This discrepancy in etching rate will expand as higher Sn composition samples will be used.

In the next step where active area is defined, BCB was replaced by SiO_2 as the dielectric layer for photodiode device. This is due to the curing process of BCB at 250^o C for 5 hours. Such high temperature for long period of time might affect the doping profile of the top n-type Ge cap layer, where one of the contact is formed, and leads to non-rectifying diode like behavior in I-V characteristic of DHS GeSn photodiode. Hence, a 100-200 nm-thick SiO_2 passivation layer was then deposited by plasma-enhanced chemical vapor deposition followed by the openings made for the metal contacts. Electrode pads were patterned and metalized with 10/200 nm of Cr/Au. The top view SEM image of the final devices with a diameter of 250 and 500 µm are shown in Figure 26 (a) and (b) respectively.

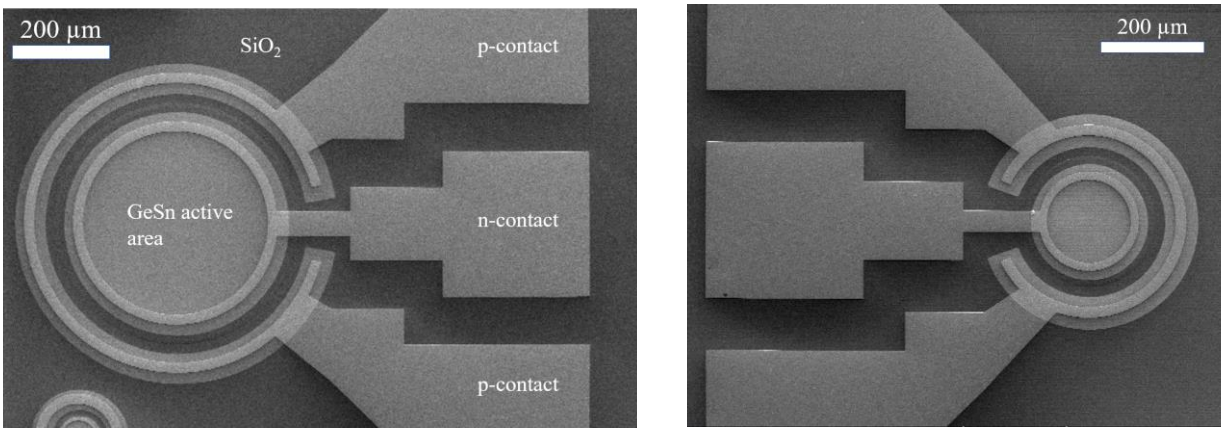

(a) (b)

Figure 26: Top view SEM image of (a) 500 µm diamter devic and (b) 250 µm diamter device

4.1.3 Temperature dependent current-voltage characterization

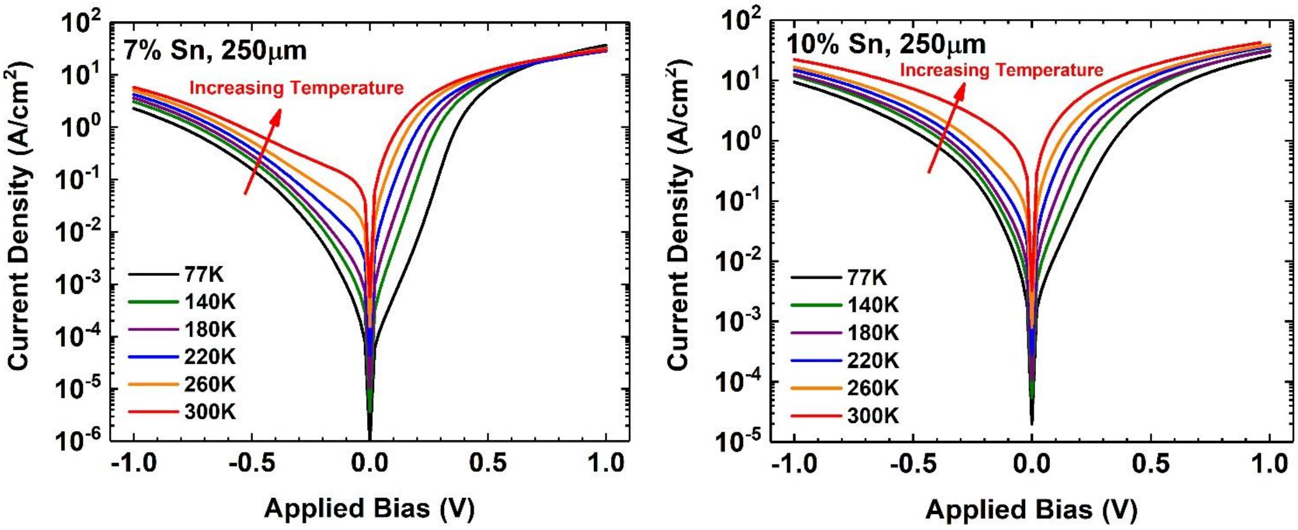

(a) (b)

Figure 27: Temperature dependent I-V characteristic of GeSn photodiode with (a) 7 % Sn and (b) 10 % Sn and the mesa size is 250 µm in diameter.

Figures 27 (a) and (b) illustrate the dark current-voltage (I-V) characteristics from 300 to 77 K of the GeSn photodiodes (mesa size of 250 µm in diameter) with Sn compositions of 7 and 10 %, respectively. The rectifying diode like behavior was observed on both devices at each temperature. Similar behavior was observed for devices with mesa size of 500 µm in diameter, that are not shown here. As the temperature increases, the reverse current density increases as a result of more thermally activated carriers. At a certain reverse voltage, the current density of the 10 % Sn device is higher than that of the 7 % Sn device for each temperature. This is mainly due to the narrower bandgap of the 10 % Sn device compared to that of the 7 % Sn device due to the higher Sn composition, which results in the more thermally excited carriers.

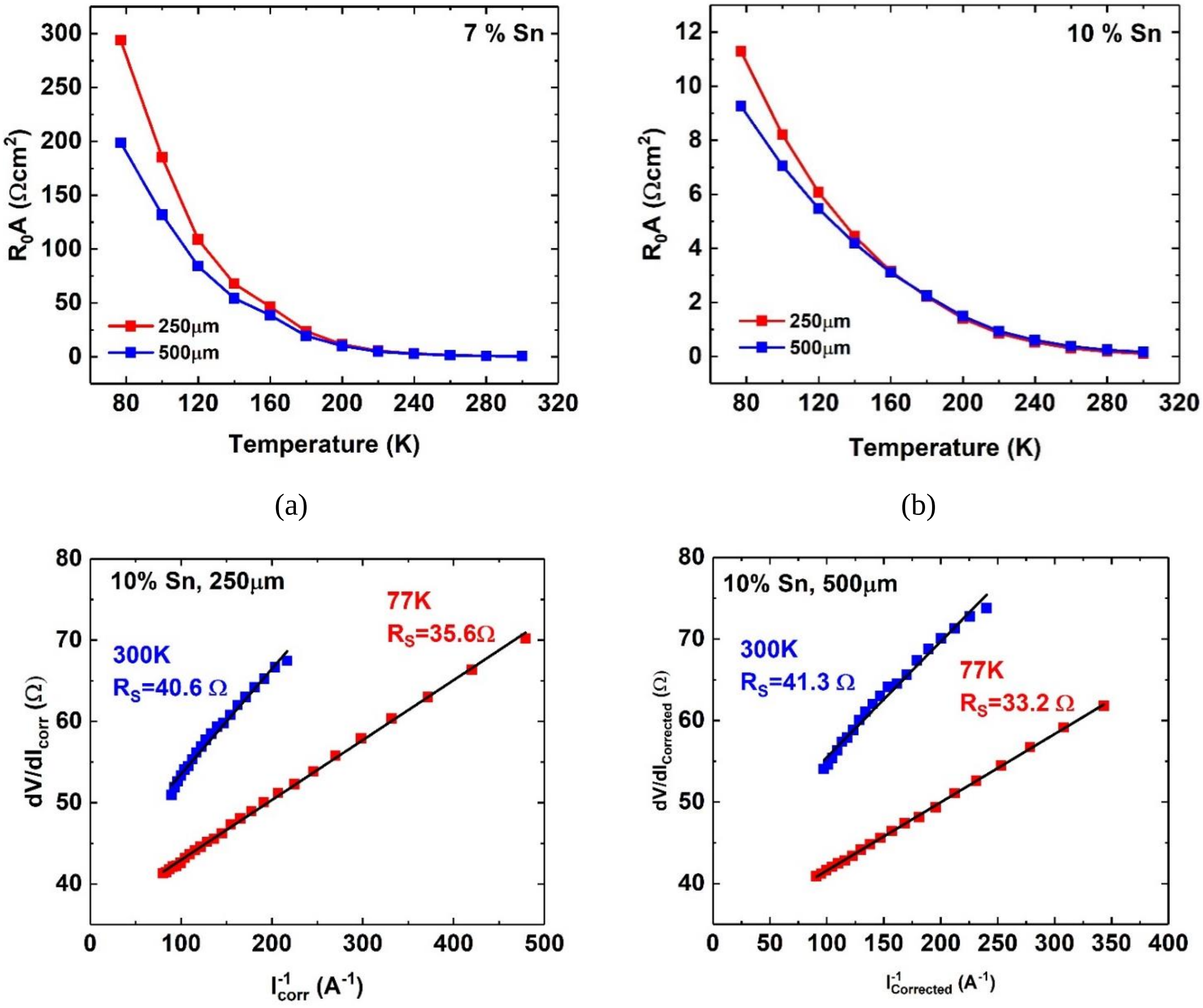

(a) (b)

(c) (d)

Figure 28: Zero-bias resistance-area product (R_0A) at different temperatures of (a) 7 % Sn and (b) 10 % Sn devices. Linear fit of $(I_{corr})^{-1}$ as a function of dV/dI_{corr} at 77 and 300 K of the (c) 10 % Sn sample of 250 μm, (d) 500 μm in diameter, and (e) 7 % Sn sample of 250 μm and 500 μm in diameter. Activation energy of 7 and 10 % Sn with different mesa sizes was shown in Figure 28 (f).

Figure 28 (Cont.)

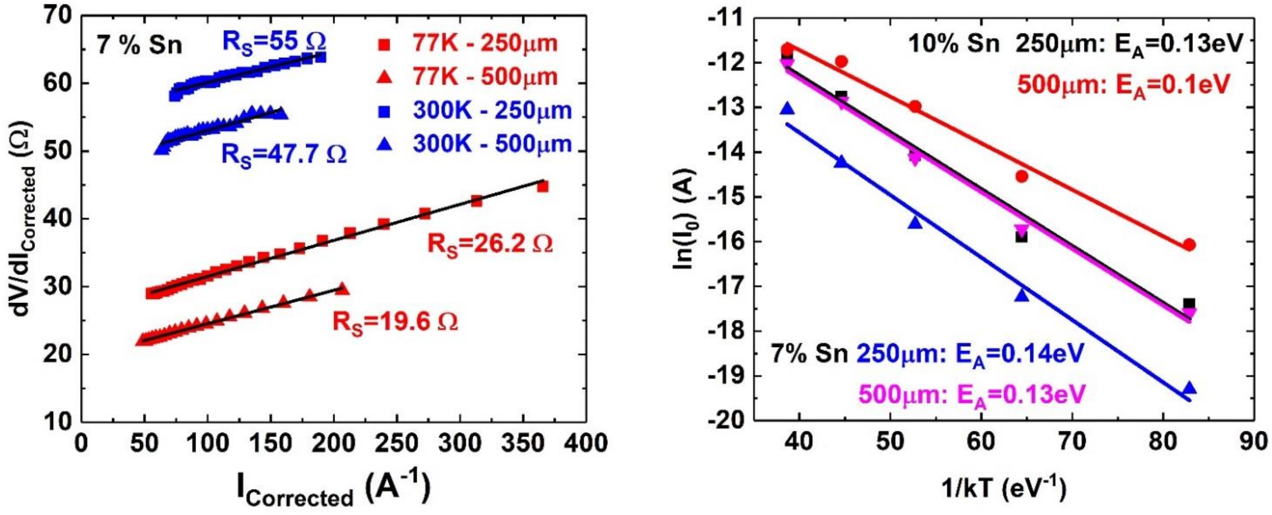

(e) (f)

The diode current can be expressed as [42]:

$$I = I_0 \exp[\frac{q(V - R_S I_{corr})}{nkT}] + \frac{V}{R_{Sh}} \tag{27}$$

where I is the measured current, I_0 is the reverse saturation current, q is the electronic charge, V is the applied voltage, n is the ideality factor, k is the Boltzmann constant, T is the absolute temperature, R_s is the series resistance, R_{sh} is the shunt resistance, and $I_{corr} = I - V/R_{Sh}$ is the corrected diode current (net current flowing through the diode) **[42], [84], [85]**. Shunt resistance R_{sh} was first extracted by taking dI/dV near 0 V (where $1/R_{sh}$ dominates other terms) for each temperature. Consequently, the zero-bias resistance-area product ($R_0A \approx R_{sh}A$) was calculated with the corresponding device area A, as shown in Figure 28 (a) and 28 (b). R_0A values of 300 and 11 Ω·cm^2 were obtained at 77 K for 7 and 10 % Sn devices, respectively, which are lower values compared to those of InGaAs and HgCdTe detectors **[8], [86]**. The shunt resistance is mainly coming from the following facts: 1) surface recombination due to the lack of surface passivation. This part of shunt resistance can be eliminated by applying passivation technique that reported in

[49], [57]; 2) since wet chemical etching process was used for mesa etch, the Sn could be re-deposited on the mesa surface and sidewall, resulting in the shunt current.

Replacing I by $I_{corr} = I - V/R_{Sh}$ in equation (27) and taking the reciprocal derivative $dV/dI_{corr} = (nkT/q)I_{corr}^{-1} + R_S$, the series resistance R_s can be extracted at the y-axis intercept of the dV/dI_{corr} versus $(I_{corr})^{-1}$ plot, as shown in Figure 28 (c), (d), and (e). By extrapolating the semi-logarithmic plot of I_{corr} versus $V\text{-}R_S I_{corr}$, the reverse saturation current I_0 can be evaluated from the y-axis intercept (figures are not shown here). Moreover, the Arrhenius activation energy was estimated from a fit of temperature dependent $I_0 = I_{00}\exp(-E_A/kT)$, where I_{00} is a constant, as shown in Figure 28 (f). The GeSn diode parameters are summarized in Table 7.

Table 7. Series Resistance, Shunt Resistance, Reverse Saturation Current, and Activation Energy at 77 K and 300 K

Device	77 K			300 K			E_A (eV)
	R_S (Ω)	R_{Sh} (kΩ)	I_0 (A)	R_S (Ω)	R_{Sh} (kΩ)	I_0 (A)	
7 % Sn, 250 µm	26.2	599	6.4×10^{-8}	55.5	0.85	2.2×10^{-5}	0.14
7 % Sn, 500 µm	19.6	101	2.4×10^{-7}	44.7	0.22	5.9×10^{-5}	0.13
10 % Sn, 250 µm	35.6	23.0	3.2×10^{-6}	40.6	0.21	6.9×10^{-5}	0.13
10 % Sn, 500 µm	33.2	4.70	2.6×10^{-5}	41.3	0.08	8.1×10^{-5}	0.10

As the Sn composition increases, the shunt resistance R_{sh} decreases while the reverse saturation current I_0 increases. On the other hand, devices with larger mesa size feature lower shunt resistance and higher saturation current compared to those with smaller mesa size. There is no clear trend for the series resistance Rs, which ranges from 19.6 Ω (7 % Sn, 500 µm) to 35.6 Ω (10 % Sn, 250 µm) at 77 K and from 40.6 Ω (10 % Sn, 250 µm) to 55.5 Ω (7 % Sn, 250 µm) at

300 K. It is desirable to have small series resistance in a photodiode. For our samples, the high series resistance might be attributed to the relatively thin n-type Ge contact layer (50 nm cap layer). In contrast with R_S, infinite parallel shunt resistance R_{sh} is desirable in a photodiode since it reduces the thermal noise effect. A parallel shunt resistance from 100 to 600 kΩ and 5 to 23 kΩ at 77 K and from 220 to 850 Ω and 84 to 214 Ω at 300 K was obtained for 7 and 10 % Sn devices, respectively. The lower value of shunt resistance with the higher Sn-composition device signals the existence of the leakage current. The device with larger perimeter featuring lower shunt resistance was observed as expected. Similar photodiode behavior has been reported for InGaAs, extended-InGaAs, and short-wave HgCdTe detectors [87]. From the temperature-dependent reverse saturation current, the Arrhenius activation energies E_A for both devices were extracted. According to the theoretical study, the $E_A \sim E_g/2$ indicates that the Shockley-Hall-Read recombination is the main source of dark current [88]. For the E_A obtained in this study, their values ranging from 0.1 to 0.14 eV were much lower than $E_g/2$ (~0.28 and 0.24 eV for 7 and 10 % Sn devices, respectively), which seems to suggest a process of defect-assisted tunneling and/or thermionic tunneling [33], [89], [90].

The reverse dark current density was further investigated to estimate the surface leakage current, which is proportional to the perimeter of the device under test. At -1 V, J_{surf} were extracted to be ~ 2 mA/cm and 40 mA/cm for 7 and 10 % Sn sample at 77 K, respectively. As the temperature increases to 300 K, these values reach 18 mA/cm and 100 mA/cm. The relatively high surface leakage current density is mainly due to these causes: 1) no surface passivation technique was applied on the sidewalls of photodiode device; and 2) the narrowed bandgap of the $Ge_{1-x}Sn_x$ alloy leads to more thermally excited carriers. The dark current can be reduced by a passivation technique either using Si [49], yttrium-doped GeO_2 *[91]*, or GeO_x/Al_2O_3 [57] as the passivation layer.

4.1.4 Spectral response

Figures 29 (a) and 29 (b) show the spectral response of 7 and 10 % Sn photodiode detectors in the temperature range from 300 to 77 K. The red shift of absorption edge as the temperature increases was observed for both devices. The 7 % Sn device exhibits a cutoff wavelength of 2.0 and 2.2 µm at 77 and 300 K, respectively. Such cutoff wavelengths are way beyond the Ge band-to-band absorption edge (1.55 µm), indicating that the photoresponse beyond 1.55 µm is mainly contributed by the GeSn absorption. For the 10 % Sn device, the observed photoresponse extended to 2.3 and 2.6 µm at 77 K and 300 K, respectively. This longer wavelength coverage is due to the reduced bandgap for the increased Sn composition as expected by Vegard's law interpolation of Ge and Sn [30]. The signal distortion at 1.8-1.9 µm is due to the atmospheric absorption that occurred for all of devices regardless of the Sn composition and temperature.

As mentioned in equation in chapter 2, a semi-logarithmic plot of spectral response intensity versus the photon energy can be used to extract the *m* values, as shown in Figure 29 (c) and 29 (d) for the 7 and 10 % Sn photodiode devices. Based on the study of band-to-band transition, the *m* is generally equal to 2 and 1/2 for the indirect and direct bandgap transition, respectively. The *m* values in this study were extracted as 1.11 for the 7 % Sn device, and 0.61 for the 10 % Sn device at 300 K. This can be explained as following: for the 7 % Sn device, the energy separation between indirect and direct bandgap is small (28 meV), therefore the absorption edges of indirect and direct bandgap transition cannot be identified, resulting in the "overall" absorption edge with *m* value between the 2 and 1/2; while for the 10 % Sn device, since the GeSn alloy with 10 % Sn has been identified as a direct bandgap material, the Sn composition of 9.24 % in this study is very close to the indirect-to-direct transition point. Although the sample is still an indirect bandgap material, the absorption arising from direct bandgap transition dominates the spectral response, leading to the *m* value of 0.61 which is close to 1/2. Moreover, as temperature decreases, the *m* values stay almost unaltered for both devices, indicating the identical absorption mechanism at each temperature.

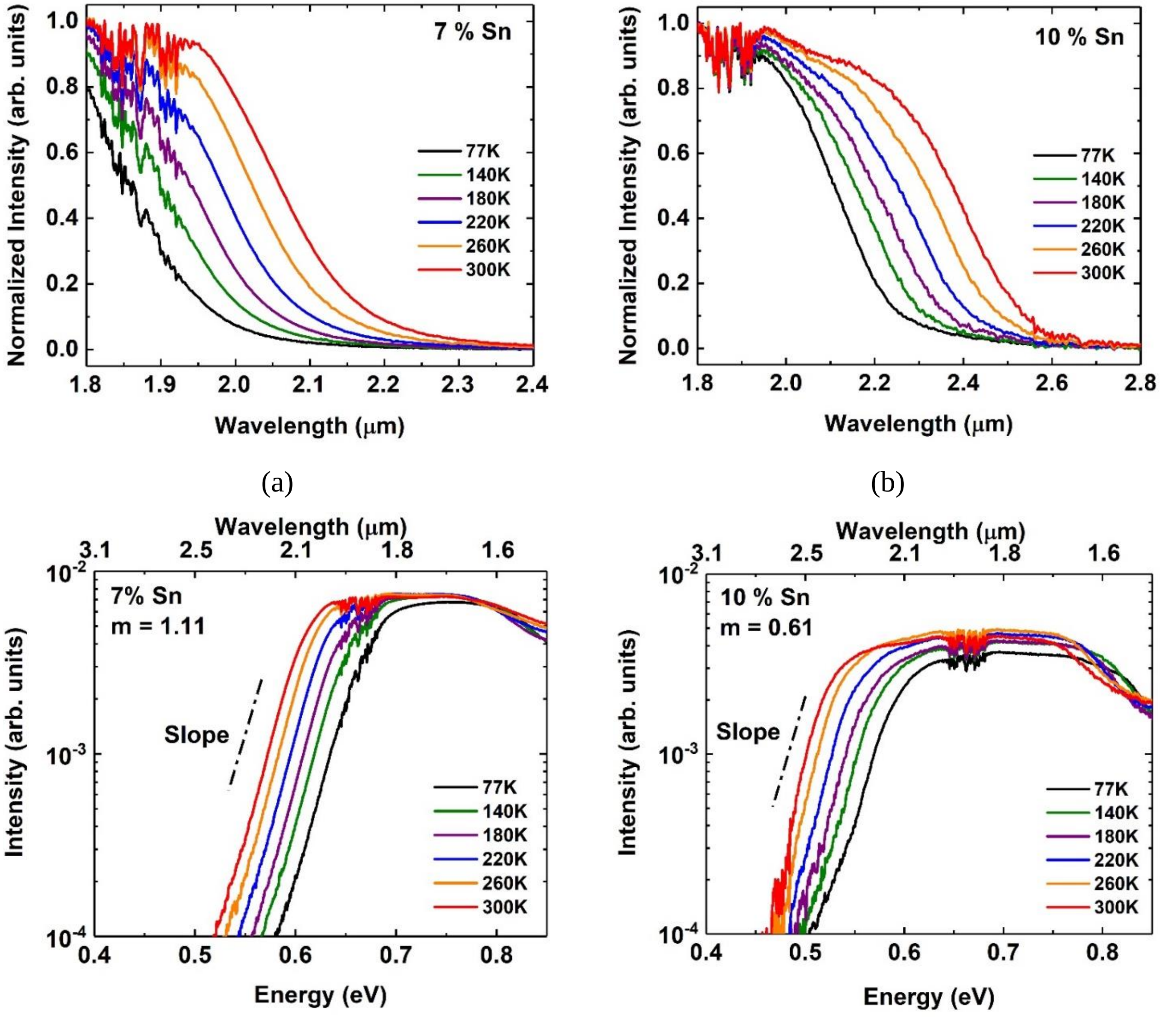

(a) (b)

(c) (d)

Figure 29: Normalized temperature dependent spectral response of (a) 7 % Sn photodiode and (b) 10 % Sn photodiode. Temperature dependent absorption edge of (c) 7 % Sn photodiode with m = 1.11 and (d) 10 % Sn photodiode with m = 0.61.

4.1.5 Temperature dependent responsivity

The responsivity was measured at 1.55 µm with a normal incidence laser beam. The I-V curves measured under dark and laser illumination at each temperature were used to calculate the responsivity value verse the bias voltage. Responsivity can be interpreted as *[39], [78]*:

$$R = \frac{\lambda}{1.24}(1-r)\eta_r(1-e^{-\alpha x}) \tag{28}$$

where λ is the wavelength, r is the Fresnel loss, η_r is the collection efficiency, α is the absorption coefficient, and x is the thickness of absorption layer.

Figures 30 (a) and 30 (b) show the responsivity at 1.55 µm of 7 and 10 % Sn photodiode devices at the temperatures ranging from 77 to 300 K. The peak responsivities of 0.3 and 0.19 A/W were obtained at 300 K with 0.1 V reverse bias voltage for 7 and 10 % Sn samples respectively. As the reverse bias voltage increases, the responsivity decreases. This may be due to the higher leakage current under higher reverse bias voltage. In addition, it has been reported that the voltage dependent change of absorption coefficient as a result of the Franz-Keldysh effect could affect the responsivity [92]. At 1 V reverse bias voltage, the responsivities reduce to 0.15 and 0.07 A/W for 7 and 10 % Sn devices, respectively. The temperature dependent responsivity shows the monotonically decreased value at lower temperatures for both devices. The increasing bandgap with the decreasing temperature is responsible for this with the absorption coefficient drop. Moreover, in general the responsivity of 7 % Sn sample is higher than that of 10 % Sn sample. This is mainly due to the higher material quality of 7 % Sn sample, which was confirmed by the material characterization. The lower material quality of 10 % Sn sample leads to the enhanced non-radiative recombination such as Shockley-Read-Hall recombination (recombination through the defect levels), which reduces the extraction efficiency of photo generated carriers, resulting in the lower responsivity than 7 % Sn sample.

According to equation (28), responsivity could be improved by reducing the Fresnel optical reflection losses with an appropriate antireflection coating and by increasing the GeSn layer thickness. However, the increase in *x* decreases the response speed of the detector [86], [93]. The tradeoff between high responsivity and high-speed response should be taken into account in the design of the photodetector.

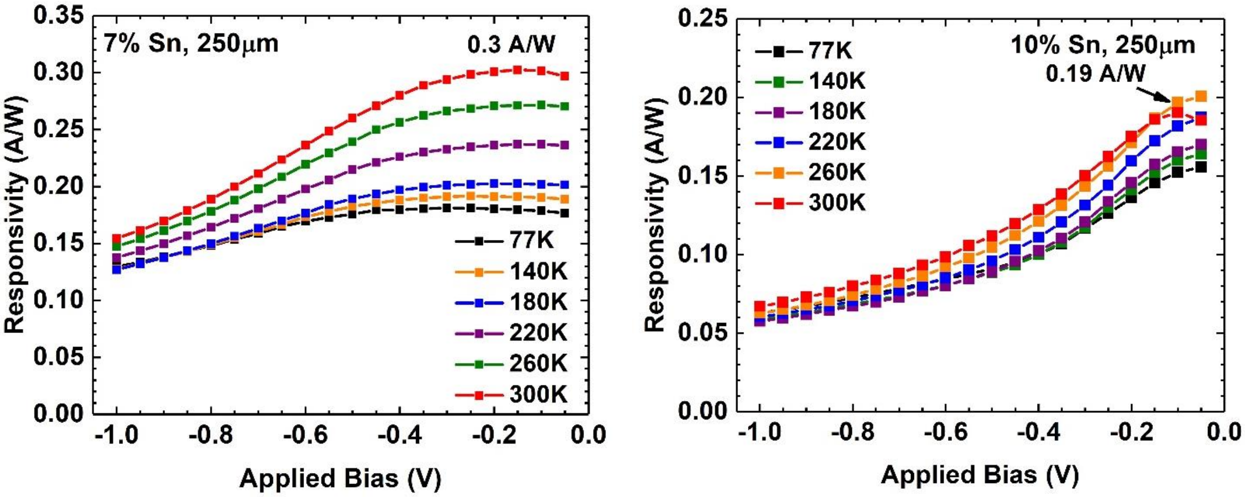

(a) (b)

Figure 30: Temperature dependent responsivity measured at 1.55 μm of (a) 7 % Sn and (b) 10 % Sn devices with mesa size of 250 μm in diameter.

4.1.6 Specific D* and noise analysis

Noise analysis

The figure-of-merit most commonly used to compare individual detector is specific detectivty D* since it normalizes detector area and uses an equivalent noise bandwidth of 1 Hz. D* can be expressed as:

$$D^* = \frac{\sqrt{A}}{NEP} = \frac{R\sqrt{A\Delta f}}{\sqrt{I_n^2}}$$

where A is the area of the detector, NEP is noise equivalent power, R is responsivity, Δf is the bandwidth, and I_n^2 is mean squared noise current in the bandwidth. For an ideal photodiode, the noise current is generally composed of thermal fluctuations (Johnson-Nyquist) and shot noise [86]. Flicker or 1/f noise is excluded since its contribution is not significant for measurement conditions above 1 Hz. Therefore, $I_n^2 = I_{thermal}^2 + I_{shot}^2$. The thermal noise follows $I_{thermal} = \sqrt{4kT\Delta f / R_0}$, where k is the Boltzmann constant, T is absolute temperature, Δf is the bandwidth, and R_0 is the resistance. The shot noise is related to dark current and photocurrent caused by incident light source. It can be described as $I_{shot} = \sqrt{2q(I_{dk} + I_{ph})\Delta f}$, where q is the electron charge, I_{dk} is the dark current, and I_{ph} is the photocurrent. The photocurrent was extracted from the responsivity measurement. In this study, noise bandwidth was set by configuring the time constant and slope/oct of the lock-in amplifier to 100 ms and 18 dB/oct, respectively. The dark current and photocurrent for the devices with 250 µm in diameter are listed in the Table 8.

Table 8. Dark current and photocurrent at different reverse bias voltages

Temperature (K)	Applied voltage (V)	7 % Sn		10 % Sn	
		Dark current (A)	Photocurrent (A)	Dark current (A)	Photocurrent (A)
300	-0.2	9.55×10^{-5}	4.81×10^{-6}	6.42×10^{-4}	2.79×10^{-6}
	-1	2.82×10^{-3}	2.47×10^{-6}	8.97×10^{-3}	1.07×10^{-6}
77	-0.2	3.03×10^{-6}	2.88×10^{-6}	6.55×10^{-5}	2.17×10^{-6}
	-1	1.12×10^{-3}	2.07×10^{-6}	4.6×10^{-3}	1×10^{-6}

Since the ideal photodiode features the suppressed dark current, the thermal noise is the main source of detector noise. However, for the $Ge_{1-x}Sn_x$ detector in this study, the shot noise is the dominant source of noise due to the relatively high dark current. Based on the measured temperature dependent I-V characteristic, each noise component can be determined, as summarized in Table 9.

Table 9. Thermal Noise and Shot Noise of 7 and 10 % Sn DHS Photodiodes with Different Diameter Size, Temperature, and Applied Voltage.

Device	Thermal Noise ($A*Hz^{-1/2}$)		Shot Noise ($A*Hz^{-1/2}$)			
			-0.2 V		-1 V	
	77 K	300 K	77 K	300 K	77 K	300 K
7 % Sn, 250 µm	$8.4\times10-^{14}$	4.4×10^{-12}	1.4×10^{-12}	5.7×10^{-12}	1.9×10^{-11}	3.0×10^{-11}
7 % Sn, 500 µm	2.1×10^{-13}	8.7×10^{-12}	2.8×10^{-12}	1.2×10^{-11}	3.4×10^{-11}	4.5×10^{-11}
10 % Sn, 250 µm	4.3×10^{-13}	8.8×10^{-12}	4.7×10^{-12}	8.6×10^{-12}	3.8×10^{-11}	5.4×10^{-11}
10 % Sn, 500 µm	9.5×10^{-13}	1.4×10^{-11}	1.4×10^{-11}	2.4×10^{-11}	5.2×10^{-11}	7.0×10^{-11}

At 77 K, the thermal noise is two or three orders of magnitude less than the shot noise at various applied bias voltages. As temperature increases, both thermal and shot noise increase with the thermal noise rising more rapidly than shot noise. The thermal noise increases about two orders of magnitude while the shot noise increases less than one order of magnitude as the temperature increases from 77 to 300 K. At 300 K, the thermal noise is only one order of magnitude smaller than the shot noise at -1 V, and is almost equal to the shot noise at -0.2 V. Therefore for the calculation of D*, both thermal noise and shot noise were considered even at lower temperatures.

*Specific detectivity D**

Specific detectivity D* of $Ge_{1-x}Sn_x$ photodiode detectors was determined by using 1 Hz equivalent noise bandwidth, the device area, the calculated noises and the measured responsivity. Figures 31 (a) and 31 (b) show the D* of 7 and 10 % Sn devices with a diameter of 250 µm from 77 K to 300 K. The peak D* of 4×10^{9} and 2.4×10^{9} $cmHz^{1/2}W^{-1}$ for 7 and 10 % Sn devices were obtained at 77 K, respectively. Although the responsivity exhibits the smallest value at this temperature, the dark current significantly decreases, resulting in the reduced noise power, and consequently the improved D* value compared to that at 300 K. The lower peak D* of the 10 % Sn device compared to that of the 7 % Sn device is due to the smaller responsivity and larger noise power. Moreover, the D* of devices with different mesa sizes show the very close values under the same temperature and bias voltage, suggesting the uniform device quality of $Ge_{1-x}Sn_x$ detectors.

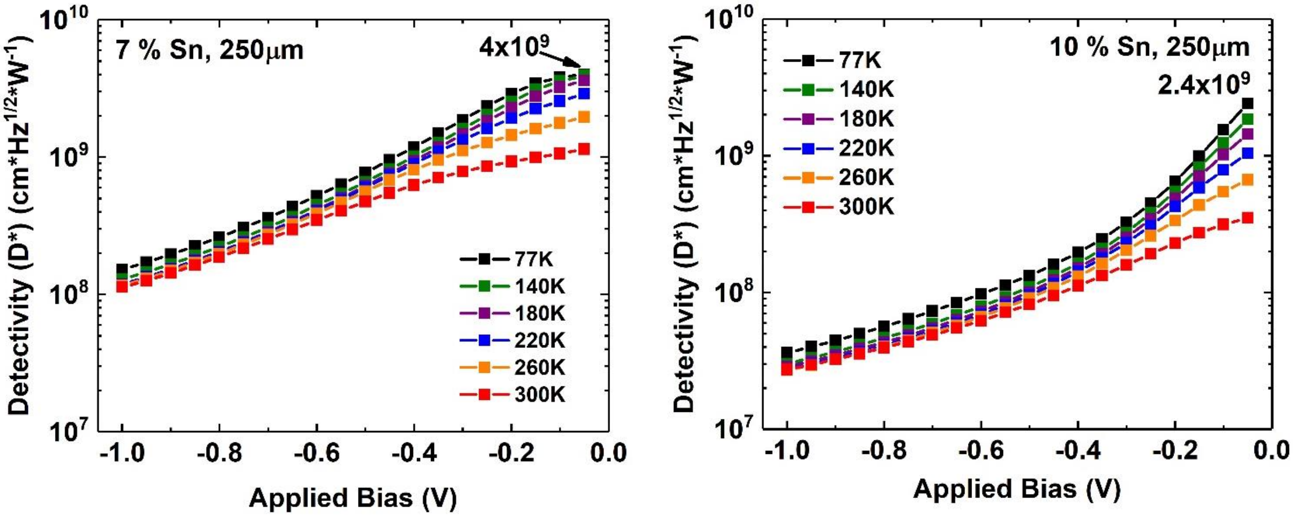

(a) (b)

Figure 31: Temperature dependent specific D* versus applied bias measured at 1.55 µm of (a) 7 % Sn and (b) 10 % Sn devices with mesa size of 250 µm in diameter.

Spectral D* of 7 and 10 % Sn photodiodes (measured at 0.1 V reverse bias voltage) is shown in Figure 32 to directly compare with D* of other market-dominating detectors that use Ge, PbS, InAs, and InGaAs technologies. The spectral response absorption edge is extended to 2.6 µm at 300 K for the 10 % Sn device, which is comparable to the edge-response of an extended-InGaAs detector at 300 K. Compared to our previous study on GeSn photoconductors [47], [50], the spectral D* here has been improved due to the lower dark current of the present GeSn photodiode. The spectral D* of the 7 % Sn device at 77 K is only one order of magnitude lower than that of extended-InGaAs detectors. A decrease in the device dark current via a thicker GeSn layer and via application of the passivation technique would dramatically reduce the noise. Moreover, a thicker GeSn layer would enhance the absorption in SWIR. Therefore significantly improved D* of GeSn photodiode detectors can be achieved, making them competitive with commercially available detector technologies in the above-discussed SWIR FPA applications-space.

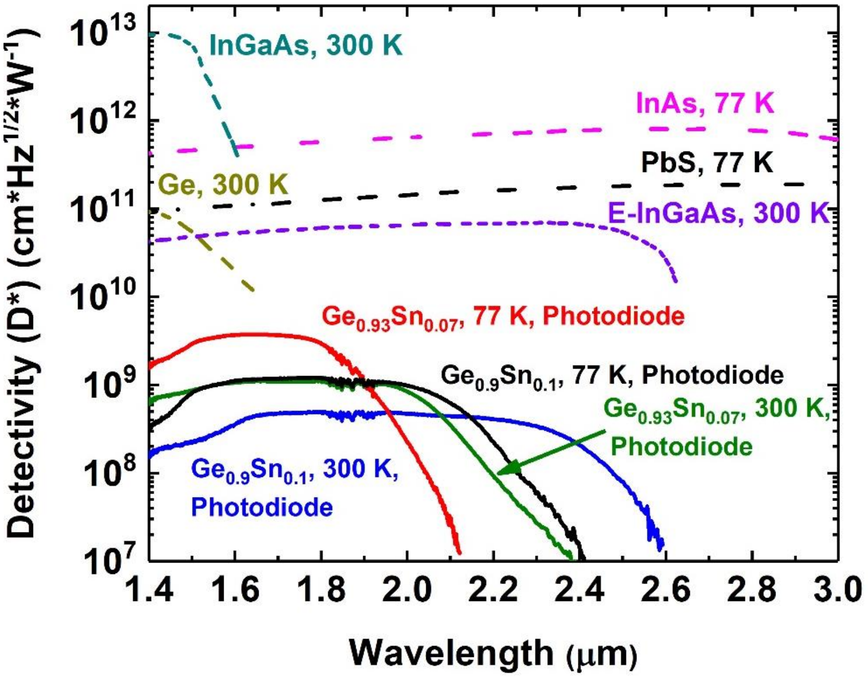

Figure 32: Spectral D* of 7 and 10 % Sn photodiodes measured at 0.1 V reverse bias voltage across a 250 µm-diameter device. Other market dominating detectors in same spectral range are plotted for comparison.

4.2 Second generation $Ge_{1-x}Sn_x$ photodiodes

4.2.1 New photodiode structure design

Based on previous study in section 4.1, there are several problems to be addressed in order to further improve the performance of the devices such as: a narrow depletion region approximately 10 nm or less at -1V due to high doping concentration of each Ge and GeSn layer ($10^{19}cm^{-3}$), a thin absorption layer (200nm) that limits the responsivity, and a high dark current due to placement of junction at defective layer and lack of passivation method. In fact, those issues could be resolved by literally design a new structure with lower doping concentration and thicker absorption layer. However, it is important to match the design with the current growth technique.

Samples studied in this section will not include surface passivation technique which will be discussed in chapter 5.

With the current growth limitation, a nominal Sn composition of 11 % is selected in this design which results in n-type $Ge_{0.89}Sn_{0.11}$ / i-$Ge_{0.89}Sn_{0.11}$ / p-type $Ge_{0.91}Sn_{0.09}$ structure. The calculation of depletion width versus doping concentration with 11 % Sn, diffusion length versus electron and hole lifetime has been done as shown in Figure 33 (a), 33 (b), and 33 (c) while the selection of doping concentration and thickness were presented in Figure 33 (d).

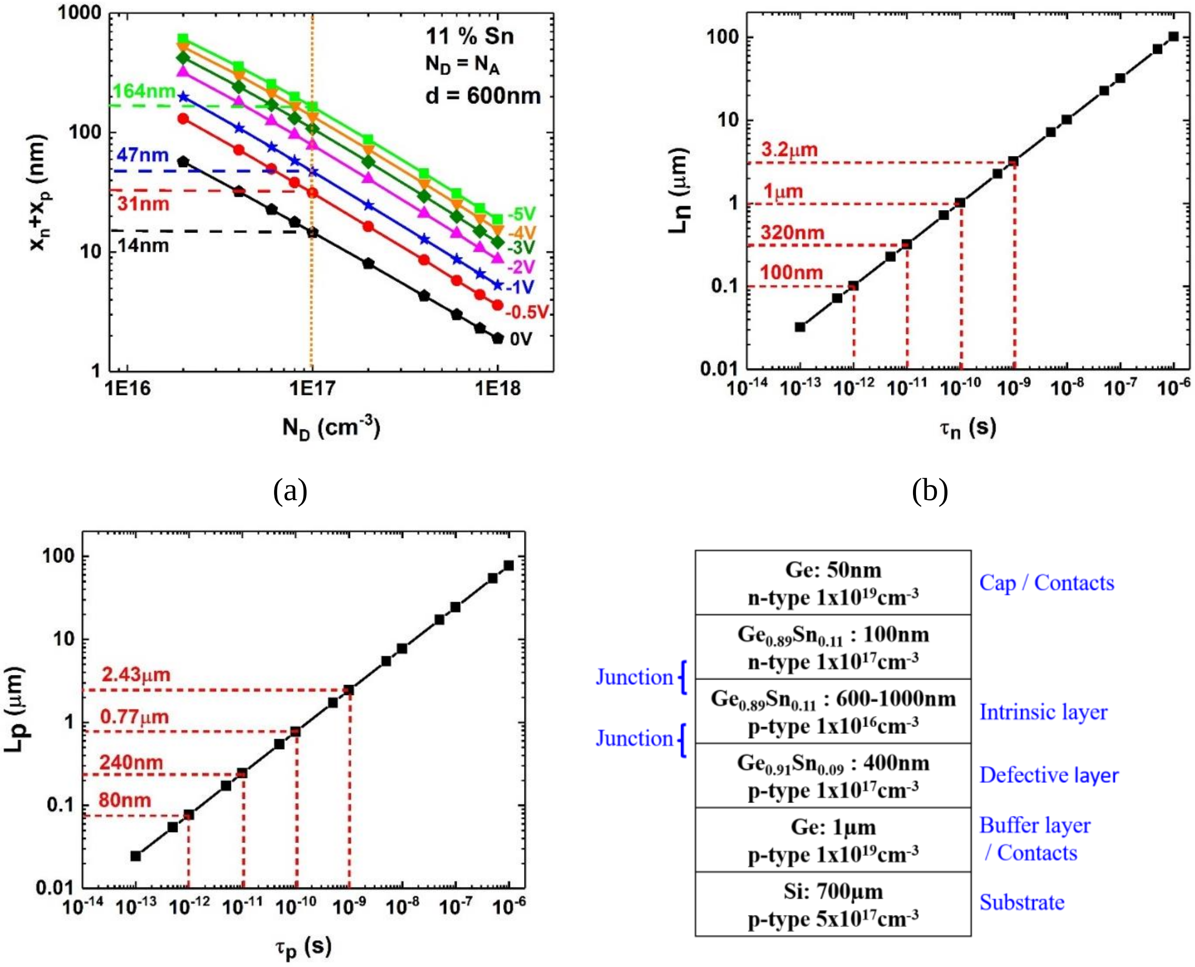

(a) (b)

(c) (d)

Figure 33: (a) Depletion width vs. Doping concentration of 11 % Sn assuming an intrinsic layer of 600 nm and $N_D=N_A$. (b) Diffusion length vs. Electron lifetime. (c) Diffusion length vs. Hole lifetime. (d) Newly proposed structure of photodiode with 11 % Sn (nominal)

The design justification is as follow. It is ideal to have N_D=N_A as low as possible, 1x10^{17} cm^{-3} or less, to increase the depletion width as suggested from Figure 33 (a). If the intrinsic layer is doped unintentionally, it is preferred p-type doping of 1x10^{16} cm^{-3} or less. This results in the formation of junction above defective layer and an increase carrier lifetime. The junctions will be formed at n-type $Ge_{0.89}Sn_{0.11}$ / i-$Ge_{0.89}Sn_{0.11}$ and at p-type $Ge_{0.91}Sn_{0.09}$ / i-$Ge_{0.89}Sn_{0.11}$. The diffusion length of hole in n-type GeSn layer is ~800 nm assuming τ_p=10 ns (Figure 33 (c)) while the diffusion length of electron in p-type GeSn layer is ~3 µm (Figure 33 (b)) assuming τ_p=1 ns. However, due to current growth limitation, a total GeSn thickness of 1 µm is selected although the thickness of intrinsic layer of 1µm is preferred to fully absorb photons at 2 µm. Based on previous study of thick GeSn sample, the first 300-400nm GeSn is considered as defective layer. An active layer of 600 nm should be allocated above the defective layer. Therefore, a n-type GeSn thickness of 100 nm and a p-type GeSn thickness of 400 nm were chosen. The excessed thickness will be counted as diffusion length. Ge cap layer profile is kept as n-type 10^{19} cm^{-3} 50 nm to provide good Ohmic contacts that were observed previously. This layer should also be thin enough to reduce light absorption. Ge buffer is doped with 10^{19} cm^{-3} p-type and Ge buffer thickness is 1 µm. This thick highly doped Ge buffer layer helps to spread the current inside of the device. The device structure is summarized in Figure 33 (d).

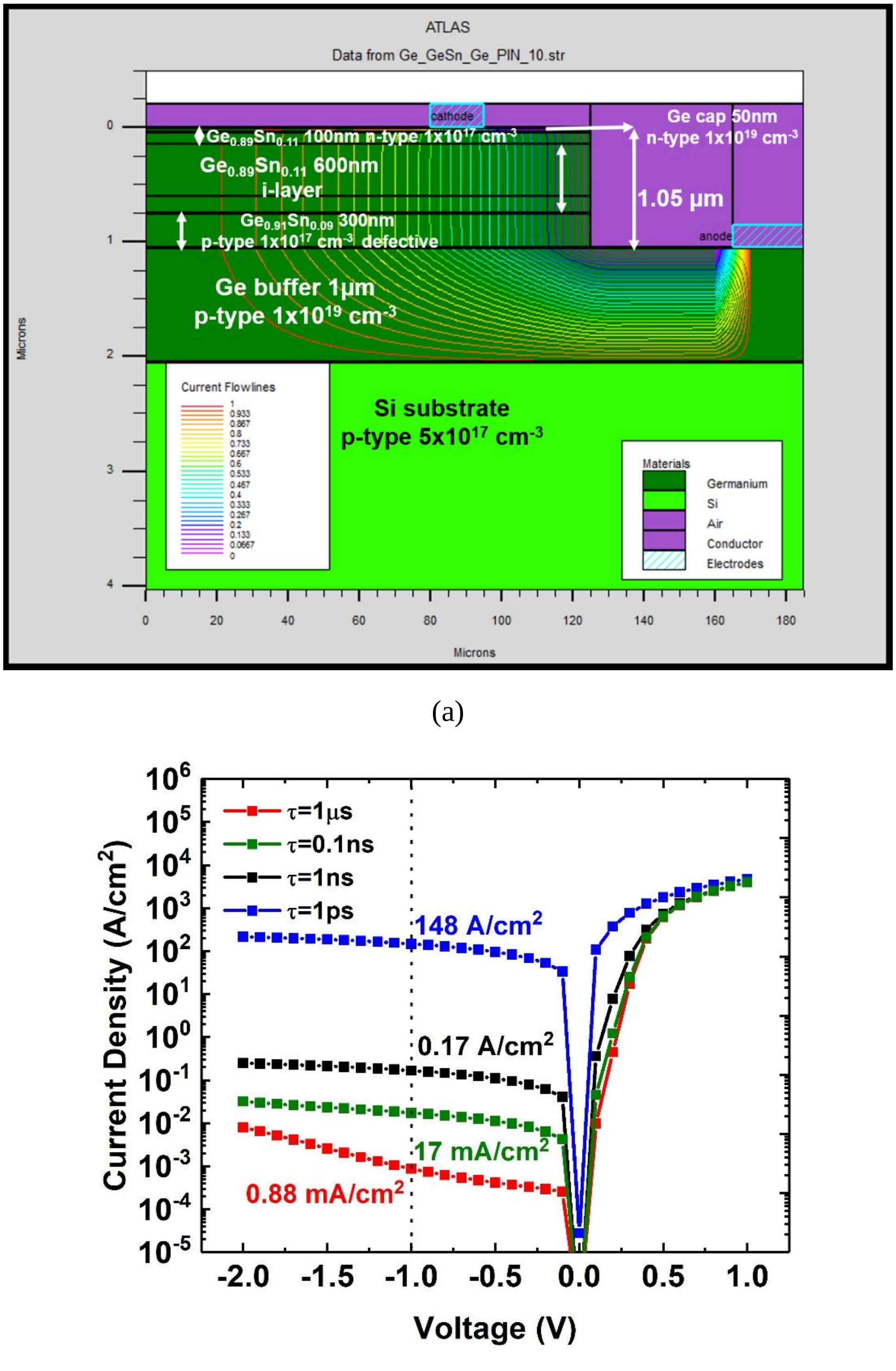

(a)

(b)

Figure 34: Silvaco simulation of (a) current flow of newly design structure and (b) current density versus voltage with $Ge_{0.89}Sn_{0.11}$ lifetime of 1µs, 0.1ns, 1ns, and 1ps.

In Figure 34 (a), the current flow of newly design structure using Silvaco simulation software suggests that there is current crowding effect near the p-contacts, the sidewalls of mesa, and the surface of Ge buffer layer. This could be resolved by either having a backside contacts on lapped Si surface or thick Ge buffer in combination with surface passivation technique. Different configuration of $Ge_{0.89}Sn_{0.11}$ lifetime of 1µs, 0.1ns, 1ns, and 1ps were used to extract current density – voltage characteristic of new photodiode structure. This parameter is strongly connected with material growth quality of GeSn layer. The better material quality is the longer carrier lifetime lasts. Our material quality is predicted to be near 10 ns due to large current density of 10 A/cm^2.

4.2.2 Material growth and characterization

Based on the proposed design, the new photodiode structure was grown using an industry standard ASM Epsilon® 2000 Plus reduced pressure chemical vapor deposition system with $SnCl_4$ and GeH_4 as Sn and Ge precursors, respectively. A 1160-nm-thick p-type (Boron as dopant) Ge buffer was first grown on the Si substrate. Then a 550-nm-thick p-type (unintentionally doped) $Ge_{0.89}Sn_{0.11}$ layer was grown followed by a 150-nm thick n-type (Arsenic as dopant) $Ge_{0.89}Sn_{0.11}$ layer. The growth was completed by capping with a 60-nm-thick heavily doped n-type Ge layer. The details of the growth technique were published elsewhere [23], [66].

After growth, material characterizations including cross-sectional transmission electron microscopy (TEM) and secondary ion mass spectrometry (SIMS) were performed to identify the layer thicknesses, Sn composition, and doping profile. Figure 35 shows a TEM image of the sample (middle panel) where each layer can be identified clearly. (Note that for GeSn, two distinct layers can be resolved: a 250-nm-thick defective bottom layer and a 450-nm-thick high-quality top layer). The Sn composition and doping profile obtained from SIMS are shown in Figure 35 left and right panels, respectively. The Sn composition was measured as 11% in the GeSn top layer, with a slight decrease in the GeSn bottom layer. The higher Sn composition in the GeSn top layer is due to the ease of Sn incorporation when the underneath layer is relaxed [23], [66]. The magenta and red curves in Figure 35 (right panel) indicate the As and B doping concentrations, respectively. The Ge cap and buffer layers were heavily doped to easily form Ohmic contacts. The n- and p-type doping concentrations of the $Ge_{0.89}Sn_{0.11}$ layer were measured as 2×10^{18} cm^{-3} (from the SIMS result) and 1×10^{17} cm^{-3} (unintentional doping, measured separately from a different reference sample), respectively. As a result, the depletion region (calculated as 150-nm width) is located mainly in the p-type GeSn layer with high material quality. Since the depletion region edge is ~150 nm away from the defective GeSn bottom layer, most photo generated carriers can be effectively collected.

Figure 36 summarizes the structure of newly growth photodiode sample. Comparing with the proposed design, this growth has shown great efforts to achieve Sn composition, thickness of each layer, and most of the doping concentration.

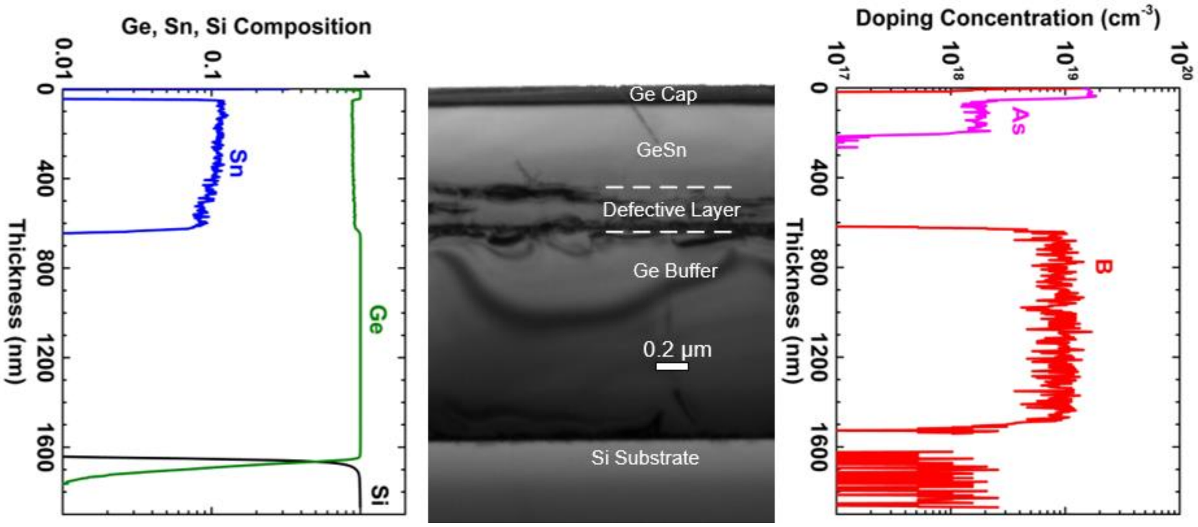

Figure 35: TEM image (middle) of the cross-section of the sample with each layer clearly resolved. The SIMS depth profile analysis of the devices' Ge, Sn, Si composition (left) and doping profile (right).

4.2.3 Device fabrication

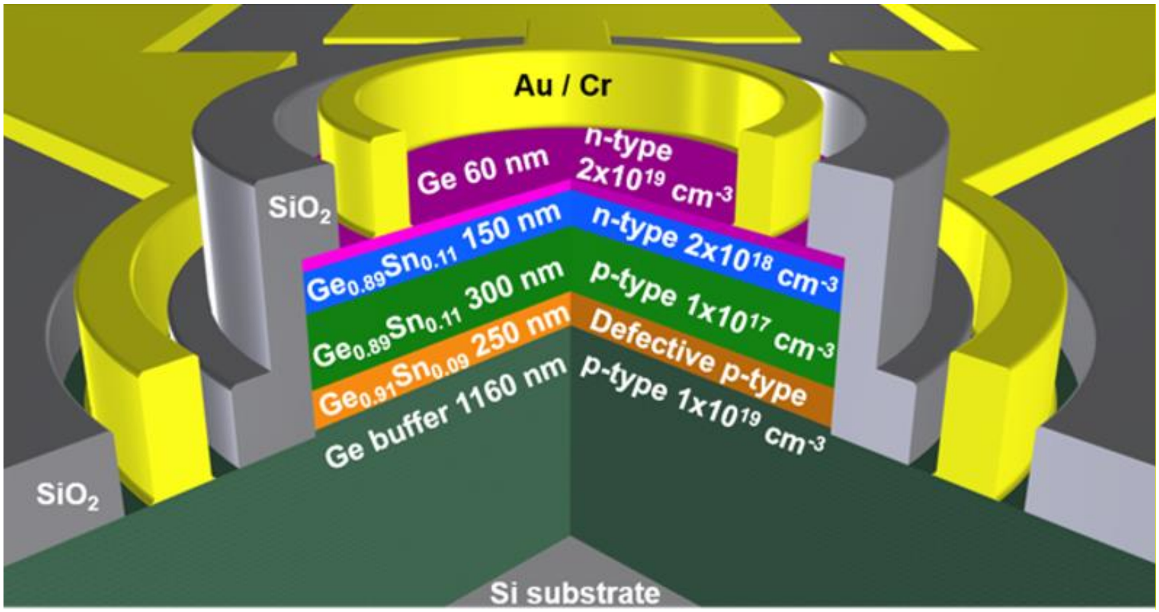

Figure 36: Schematic diagram of the Ge$_{0.89}$Sn$_{0.11}$ photodiode

The fabrication process of 2nd generation photodiode followed similar steps presented in previous section 4.1. Due to thicker Ge / GeSn layer which is around 760 nm, etching process, SiO$_2$ deposition, and metal deposition process were modified accordingly.

Wet chemical etching using HCl: H_2O_2: H_2O = 1:1:10 solution at 0^o C was employed to etch circular mesa structures with diameters of 100 µm, 250 µm and 500 µm. Due to the nature of lateral etching of wet chemical etching process, low temperature etching at 0^o C was studied and applied to reduce lateral etching and to enhance surface smoothness. The solution was prepared in a beaker which was submerged in another beaker of ice. The control of temperature is very important since a slight chance from 0 to 2 ^{0}C introduces a change in etch rate of 10 nm / min. With a stable etching rate of 20 nm / min at 0 ^{0}C, the etching depth was controlled to be 700 nm to expose the p-type Ge layer for metal contact. Figure 37 (a) shows the mesas after wet etching at 0 ^{0}C with a smooth side edge. At room temperature, the etching rate of similar Sn composition increases to approximately 100 nm / min.

A 300-nm-thick SiO_2 passivation layer was then deposited by plasma-enhanced chemical vapor deposition followed by the openings made for the metal contacts. Electrode pads were patterned and metalized with 10/300 nm of Cr/Au. The thickness of silicon oxide and metal were adjusted to be 30 – 40 % of the etching depth to make sure the slope of mesas was successfully connected. Figure 36 shows the cross-view of a schematic diagram for the typical device while figure 37 (b) presents the top view microscope image of the devices with different mesas diameter after lift-off process.

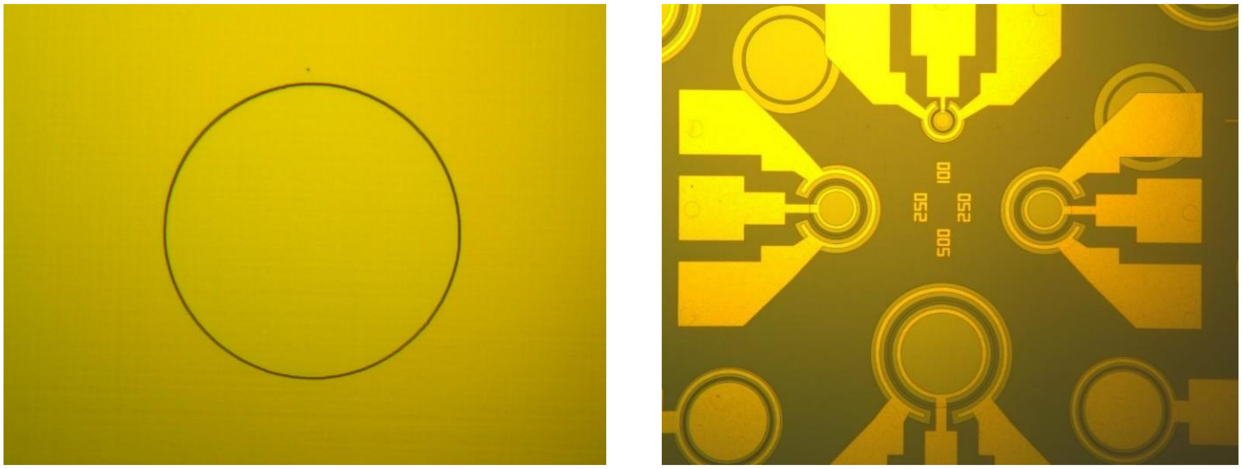

(a) (b)

Figure 37: Top view microscope image of (a) mesa after wet etching at 0^o C and (b) devices after lift-off process.

4.2.4 Temperature dependent current-voltage characterization

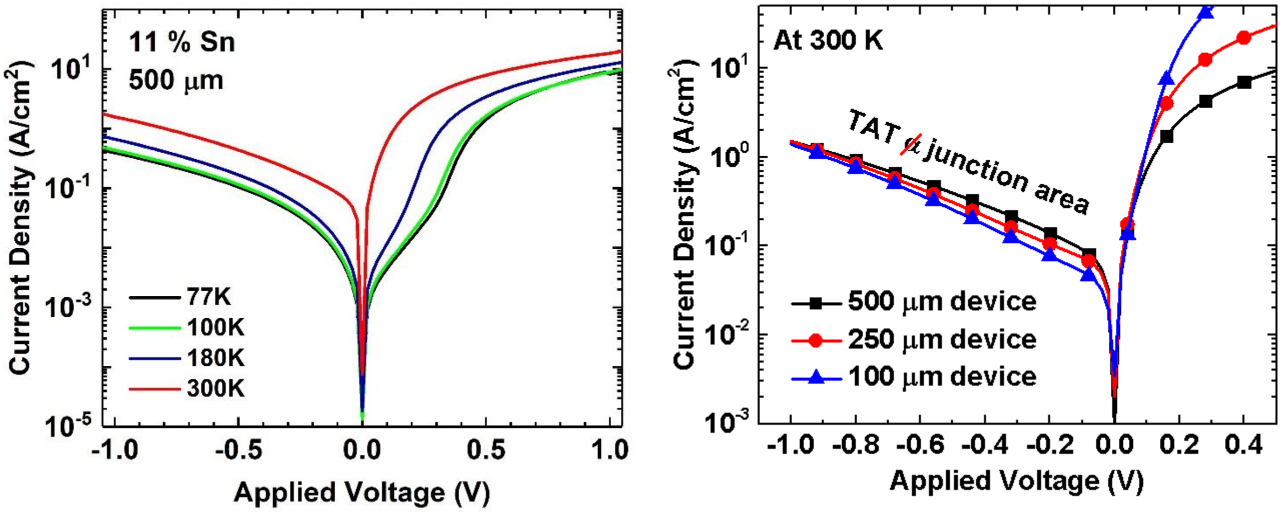

(a) (b)

Figure 38: (a) Temperature dependent J-V characteristic of GeSn photodiode with 11 % Sn and the mesa size is 500 µm in diameter. (b) J-V characteristic of 11 % Sn photodiode at 300 K with mesa size of 100, 250, and 500 µm in diameter.

Figure 38 (a) shows the temperature dependent dark current-voltage characteristics of the 500 µm photodiode with 11 % Sn from 77 to 300 K. It exhibited the rectifying diode-like behavior for presenting temperatures. This characteristic was also observed using 7 and 10 % Sn photodiode presented above. As the temperature increases, the dark current density increases. At – 1 V and 77 K, the dark current density of 250 µm and 500 µm device is 1.1 and 0.4 A/cm^2 respectively, which is 9-10 times less than the one of 10 % Sn of similar size. While at 300 K, the dark current density of 250 µm and 500 µm device increases to 3 and 1.6 A/cm^2. This dark current density is 5-6 times less than the one of 10 % Sn. Such reduction of dark current with a slight increase in Sn composition could be attributed to newly design which relocate the junctions away from defective layer. In order to further understand the origin of the dark current, the dynamic resistances $R_{dynamic}$ will be extracted from *I-V* characteristics and analyze in our future publication. Generally speaking, the dynamic resistance is a combination of series, forward bias, trap-assisted tunneling (TAT) and shunt resistances as given in Ref. [94].

Table 10. Series Resistance, Shunt Resistance, and Dark Current at 77 K and 300 K

Device	77 K			300 K		
	R_S (Ω)	R_{Sh} (kΩ)	J_D @-1V (A/cm^2)	R_S (Ω)	R_{Sh} (kΩ)	J_D @-1V (A/cm^2)
7 % Sn, 250 µm	26.2	599	2.3	55.5	0.85	5.8
7 % Sn, 500 µm	19.6	101	1.8	44.7	0.22	3.2
10 % Sn, 250 µm	35.6	23.0	9.4	40.6	0.21	18
10 % Sn, 500 µm	33.2	4.70	4.3	41.3	0.08	7.8
11 % Sn, 250 µm	36	12×10^3	1.1	22	6.9	3
11 % Sn, 500 µm	33	12	0.4	24	0.9	1.6

Table 10 summarized series resistance, shunt resistance, and dark current of 7, 10, and 11 % Sn photodiode with diameter of 250 and 500 µm at 77 and 300 K. Parameters of 11 % photodiode with new design are highlighted for comparison. The series resistance of 11 % photodiode ranged from 36 (250 µm) and 33 Ohm (500 µm) at 77 K to 22 (250 µm) and 24 Ohm (500 µm) at 300 K. The relatively high series resistance suggested that there is a current crowding effect at the contacts, which was predicted by current flow using Silvaco simulation. The shunt resistance of the 500 µm devices ranges from 0.9 to 12 kΩ, which is much smaller than that of commercial detectors whose shunt resistance is in the range of mega-Ohms. This is mainly due to the surface and sidewall leakage currents, which could be significantly reduced by using advanced passivation techniques [49], [57]. However, the reported value of shunt resistance has been improved 2.5 times at 77 K and 10 times at 300 K comparing with 10 % Sn device. Such increase in shunt resistance will reduce the noise current and result in high specific detectivity D*.

Figure 38 (b) shows the dark current densities of the devices with different diameters of 100 µm, 250 µm and 500 µm at 300 K. The current in the reverse bias region does not scale with the junction area, and the current density decreases with decreasing size of the devices for all temperatures. The similar behavior was observed in Ref. [95]. In fact, the TAT mechanism dominates the bias region, and the TAT current strongly depend on the trap density. From the *I*-*V* analysis, the trap distribution is non-uniform, which leads to that the reverse current does not scale with junction area.

4.2.5 Temperature dependent responsivity and external quantum efficiency

The temperature-dependent responsivity measured at 2.0 µm is shown in Figure 39 (a). A peak responsivity of 0.32 A/W was obtained at -0.1 V bias and 300 K temperature. The obtained responsivity is approximately three times of our previously reported device (0.12 A/W measured at 2 µm),[13] which can be explained as follows: i) the thicker GeSn layer enhances the light absorption, resulting in more photo generated carriers; ii) the optimized doping profile separates the depletion region of the *pn* junction away from the defective GeSn layer, leading to improved carrier extraction efficiency. Moreover, since a 2.0 µm laser source was used, the responsivity is mainly contributed by the GeSn layer. Note that the responsivity decreases as the temperature decreases. This is due to the bandgap increase at lower temperature, which results in reduced light absorption. In addition, trap states (inside the high quality GeSn layer) not only affect the tunneling mechanism, but also are responsible for non-radiative recombination of the photo-generated carriers. In fact, at lower temperature, the photo-excited carriers partially recombine at the deeper level trap, where they cannot gain sufficient thermal energy and then to be released; while at higher temperatures, the carriers could recombine through the shallow trap level, where they can be released by thermal excitation, which leads to increased responsivity at higher temperature. In addition, at all temperatures, the responsivity decreases with increased reverse bias. This responsivity reduction is possibly associated with the Franz-Keldysh effect [55], [96]. Figure 5 (b) shows the normalized responsivity of the 500 μm photodiode at 300 K for different voltage bias from 0.1 V to 1 V. The responsivity decreases near the band edge due to Franz- Keldysh effect [96]. Note that the band edge appears to shift to shorter wavelength with higher electric field. The Franz-Keldysh effect describes oscillations in the carrier transition probability for energies above the conduction band edge in the presence of an electric field [96].

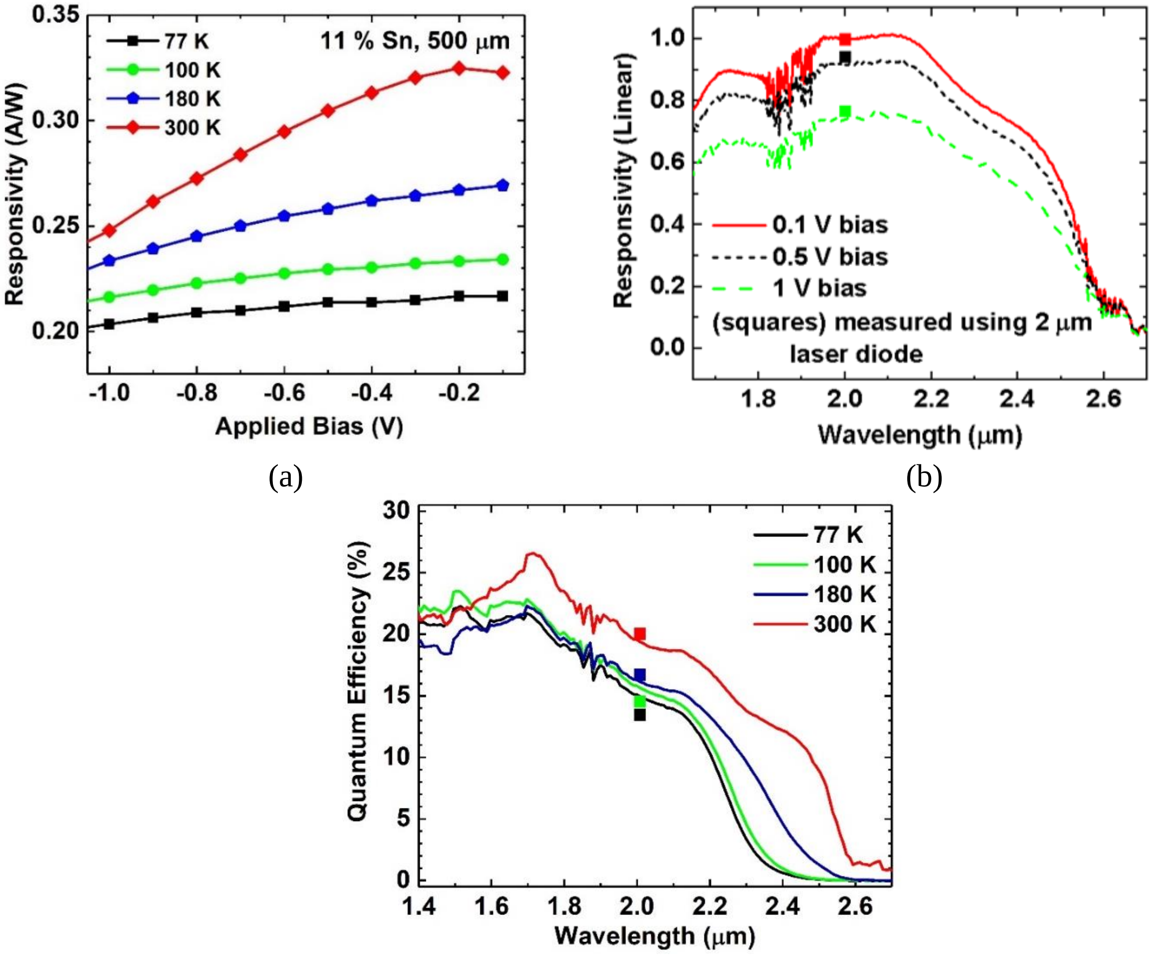

(a) (b)

(c)

Figure 39: (a) Temperature dependent responsivity versus bias voltage measured at 2 μm of 11 % Sn photodiode with 500 μm in diameter. (b) Measured responsivity as a function of wavelength for different applied voltages to demonstrate the Franz-Keldysh effect. (c) Temperature-dependent spectral EQE. The dots are measured data using 2 μm laser diode.

The EQEs of the $Ge_{0.89}Sn_{0.11}$ photodiode from 300 to 77 K are shown in Figure 39 (c). The EQEs increase as the temperature increases. The reasons are expected to be similar to those of the increase of the responsivity. The falling edge of the EQE curve, which corresponds to spectral response cutoff, shifts towards longer wavelength as temperature increases because of the reduced bandgap energy. The EQE curve at room temperature shows a cusp-like feature at around 2.3 µm significantly different from its smooth rolling-over feature at low temperatures. The feature originates from the absorption of the 150-nm n-type doped GeSn layer above the depletion region. At 300 K, the EQE achieves 22 % and 20 % at 1.55 µm and 2.0 µm, respectively. The theoretical calculated value of EQE for GeSn material system at 2.0 µm is ~60 % without anti-reflection coatings (assuming 100% internal quantum efficiency). The measured EQE of our $Ge_{0.89}Sn_{0.11}$ photodiode is one third of this value, indicating that the internal quantum efficiency is ~33 %. The EQE could be improved by using a passivation technique to reduce the surface recombination or using anti-reflection coating to reduce the reflection loss. Moreover, it was found that EQEs measured using 2 µm laser diode (dots) agree well with the values from spectral EQEs at the same wavelength. However, there are relative errors that are less than 10 % between the QE measured using 2 µm laser diode and the QE measured using FTIR. The reason comes from that the devices respond to second harmonic distortion of the laser diode.

In addition, near the absorption edge, the product of the absorption coefficient and the layer thickness in this case is much smaller than unity. Therefore, the spectral response signal is approximately proportional to the absorption coefficient, which is related to the energy bandgap of direct semiconductors through the following equation [97]:

$$\alpha = C\frac{(hv - E_g)^{0.5}}{hv} \tag{29}$$

where α is the absorption coefficient, C is a constant, $h\nu$ is the photon energy, and E_g is the bandgap. The bandgap of the GeSn absorbing layer at different temperatures was extracted by plotting $(S\cdot h\nu)^2$ against $h\nu$, where S is the spectral response signal. The extracted bandgap at 300 K was 0.46 eV. The temperature dependence of the bandgap was predicted by the Varshni's relation.

4.2.6 Specific spectral D*

The spectral specific detectivity D* of the $Ge_{0.89}Sn_{0.11}$ photodiode at 77 and 300 K was plotted together with previously reported $Ge_{0.9}Sn_{0.1}$ detector and with others commercialized available detectors, as shown in Figure 40. The D* of the $Ge_{0.9}Sn_{0.1}$ was replotted using responsivity measured at 2.0 µm to be comparable with the $Ge_{0.89}Sn_{0.11}$ photodiode. Thanks to the new design structure and the mature growth technique, the performance of $Ge_{0.89}Sn_{0.11}$ photodiode has been improved with a peak D* of 1.7×10^{9} cm·Hz$^{1/2}$·W^{-1} at 300 K and 4.3×10^{9} cm·Hz$^{1/2}$·W^{-1} at 77 K, which is four times higher than that of $Ge_{0.9}Sn_{0.1}$ detector. It is worth noting that this D* value is only one order of magnitude lower than that of the commercial extended-InGaAs detector. As the temperature increases, the D* decreases due to the increase in the noise current. This has been observed in the noise analysis presented in previous section. Moreover, a steeper falling edge was observed from the $Ge_{0.89}Sn_{0.11}$ photodiode compared to that of the previously reported device. This is due to the reduced mid-gap defect states that could serve as carrier generation/recombination centers, which indicates the improved material quality.

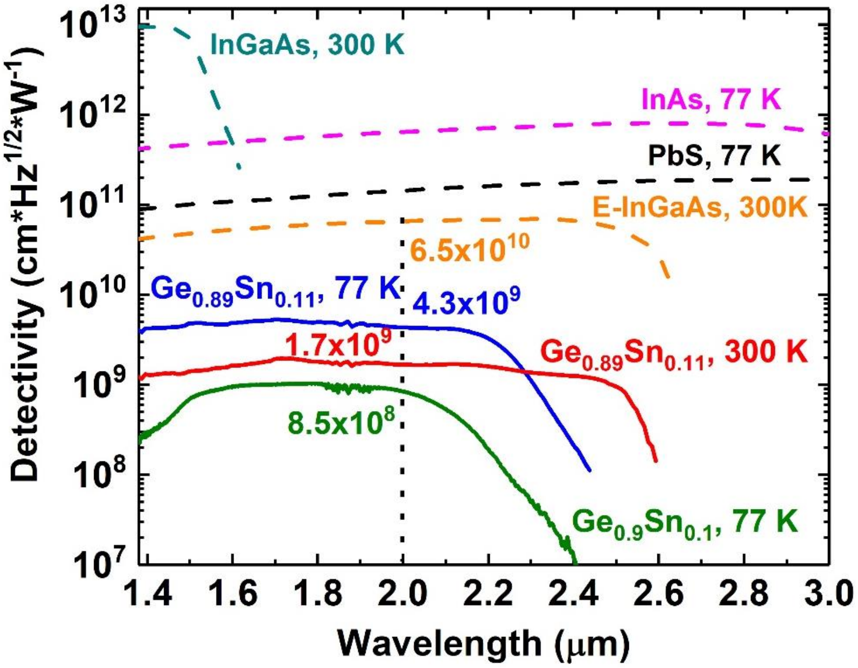

Figure 40: Spectral D* of the 500 μm $Ge_{0.89}Sn_{0.11}$ photodiode measured with a voltage bias of -0.1 V at 77 K (red) and 300 K (black). For comparison, the D* spectra of several commercial detectors and our previously reported detector at 77 K (green) are also plotted. The numbers indicate the values of D* at 2.0 μm.

Chapter 5: Effect of germanium oxynitride and germanium tin / germanium oxide passivation technique

High dark current is currently one of the key factor holding back the performance of GeSn photodetector. As the Sn composition increases, the band gap decreases which results in the enhancement of tunneling and intrinsic carrier concentration. Moreover, the high dark current could possibly be due to surface leakage via dangling bonds at the surface of GeSn or Ge and materials defects. While the materials defects could not be resolved immediately, the later issue could be reduced by implementing an appropriate surface passivation. Several efforts using Si, SiO_2, SiN_x, GeO_x / $GeSnO_x$ followed by Al_2O_3 have shown success with different degrees [49], [57]. To attain low dark current GeSn photodetector, this chapter presents an effort to study two types of surface passivation technique: GeO_xN_y (germanium oxynitride) and GeO_x / $GeSnO_x$ followed by Al_2O_3.

The first method, germanium oxynitride passivation, is well-known as an effective surface passivation technique for germanium-based optoelectronics devices. Thanks to the incorporation of nitride, the germanium oxynitride film has proven to have excellent chemical, water, and heat stability than germanium oxide [98], [99]. The growth of germanium oxynitride layer has been successfully demonstrated via thermal and plasma nitridation of Ge surfaces [100]–[102], chemical vapor deposition [103], and thermal ammonolysis of GeO_2 [104], [105]. It was applied on GeSn photodiodes samples with 11 % Sn presented in second part of chapter 4. The second method employed an oxygen source instead of ozone source in atomic layer deposition system to form germanium oxide and germanium tin oxide which have been demonstrated as an effective surface passivation for MOSFETs [106]. This method was recently reported using GeSn photodiodes. Since GeO_x / $GeSnO_x$ layer is volatile in contact with water, a layer of Al_2O_3 (ALD) was deposited immediately above GeO$_x$ / GeSnO$_x$ layer as a protective layer. The quality of the oxidized germanium layer depends strongly on pressure and temperature [107]. A set of thick film GeSn photoconductor with and without passivation were processed in parallel.

Photodiodes samples with germanium oxynitride passivation showed a decrease in dark current.

5.1 Germanium oxynitride as surface passivation technique for GeSn photodiodes

5.1.1 Device fabrication

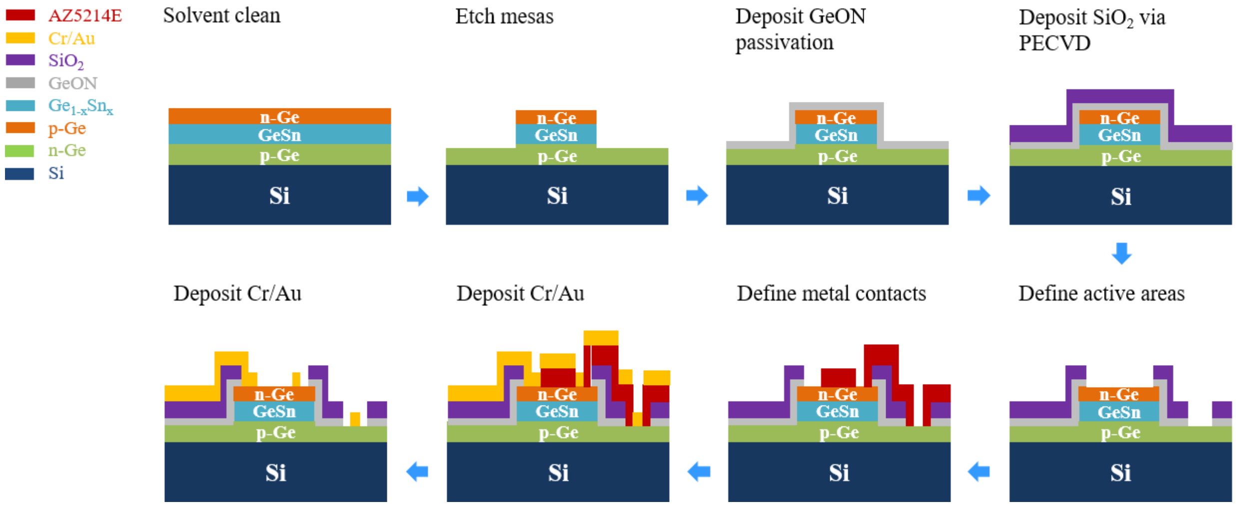

Figure 41: Fabrication process flow of 11 % Sn photodiode with GeON as surface passivation layer and with SiO$_2$ as dielectric layer

The fabrication process of GeSn photodiode with surface passivation using GeON followed the one presented in chapter 4.2 except for an additional step to deposit GeON passivation with 1 and 3 nm thickness right after defining the mesas as shown in Figure 41. The process began with the forming of circular mesas of 250 and 500 µm in diameter using photolithography. Wet chemical etching (HCl:H$_2$O$_2$:H$_2$O = 1:1:10) at low temperature was performed to transfer the pattern down to p-Ge while reducing the lateral sidewall attack. After removing the photoresist as a mask, a thin layer of GeON was deposited on top of the devices. This particular process was done by our collaborator ASM Inc. Next, a PECVD layer of SiO$_2$ was deposited to provide contacts isolation between n-Ge and p-Ge. The fabrication process concluded with opening active areas through SiO_2 / GeON layer and metal contacts formation via electron-beam evaporator of 10 nm adhesion layer Cr and 300 nm Au.

5.1.2 Device characterization

Current density-voltage analysis

Figure 42 (a) and 42 (b) depicts current density versus applied voltage of 250 and 500 µm in diameter 11 % Sn photodiodes measured at room temperature. Each set of devices is composed of 3 configurations: 3 nm GeON sample, 1 nm GeON sample, and no GeON sample (only SiO_2). For the case of 250 µm in diameter devices, the sample with 3 nm GeON has lowest current density of 1.41 A/cm^2 at -1V, which is 2.5 times less than the sample without surface passivation and 2 times less than the one with 1 nm of GeON. For the case of 500 µm devices, although the current density measured at -1V of each sample did not show significant discrepancy, sample with 3 nm GeON has the smallest current density at 1.52 A/cm^2. In addition, it is worth to note that the dark current suppression using 1 nm of GeON passivation is not sufficient based on the current density measured at room temperature.

Temperature dependent current density of 3 nm GeON devices with a diameter of 250 and 500 µm was further investigated and was used to extract shunt resistance, series resistance, and activation energy. Only temperature dependent J-V of 250 um device was shown in Figure 42 (c). The rectifying diode like behavior was observed on both devices at each temperature. As the temperature increases, the reverse current density increases as a result of more thermally activated carriers. By having a 3nm of GeON passivation, the current density measured at 77 K and -1V is 0.16 A/cm^2, which is 7.5 times less than the device without passivation under identical measurement condition. At 300 K and -1V, the current density was reduced by two times comparing with 0 nm GeON device.

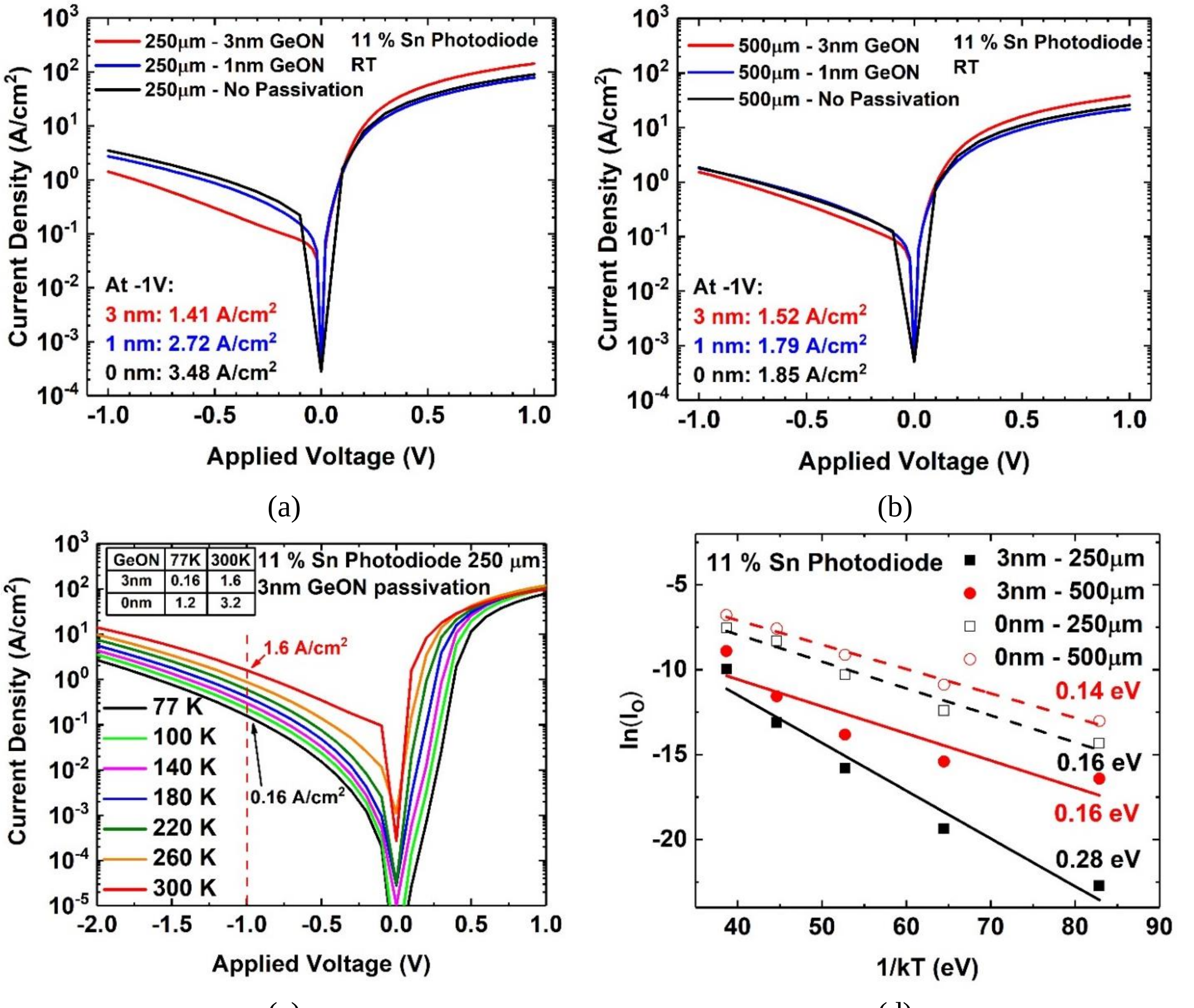

(a) (b)

(c) (d)

Figure 42: Room temperature current density versus voltage of 11 % Sn photodiodes with (a) 250 and (b) 500 µm in diameter and 3nm, 1 nm, and 0 nm GeON passivation. (c) Temperature dependent current density versus voltage of 11 % Sn photodiodes with 250 µm in diameter and 3nm GeON passivation. (d) Reverse saturation current Arrhenius plot of 11 % Sn photodiodes with 250 and 500 µm in diameter with (solid) and without (dash) GeON passivation.

The shunt resistance and series resistance were extracted by using the current equation presented in chapter 4. Under forward bias regions, the series resistance is the dominant factor of the photodiode resistance. The series resistance is determined by the electric contacts and the n-type Ge layer. Under reverse bias regions, the shunt resistance predominates. The sources of shunt resistance are mainly coming from the following facts: 1) There is surface recombination due to the lack of surface passivation. 2) Since a wet chemical etching process was used for the mesa etch, some Sn could be re-deposited on the mesa surface and sidewall, resulting in the shunt current [55]. In fact, an increase of shunt resistance from 5 to 1750 kΩ at 77 K and from 720 Ω to 3.15 kΩ at 300 K was observed for 250 µm in diameter devices with 0 and 3 nm GeON, respectively. As shown in Table 11, the device with larger perimeter featuring lower shunt resistance was obtained as expected. In contrast with Rsh, small series resistance is desirable in a photodiode. There is no clear trend for series resistance as the temperature changes. The series resistance is in the range of 13 – 16 Ω for devices with 3 nm GeON regardless of diameter and temperature. Whereas the series resistance of devices without GeON passivation ranges from 24 to 47 Ω.

The activation energy provides information about the dominant current mechanism. One of the common method that is being employed to determine activation energy is to plot the reverse saturation current versus the inverse of the temperature $I_0 = I_{00} \exp(-E_A/kT)$, where I_{00} is a constant and E_A is the activation energy in the forward bias region. If the activation energy E_A is comparable to the bandgap E_g, diffusion current dominates. If it is half of the bandgap, Shockley-Read-Hall (SRH) recombination-generation current is limiting. If it is much less than half of the bandgap, the trap-assisted tunneling (TAT) and band-to-band tunneling (BTBT) are possible the dominant factors [33], [89], [90], [108]. The possible sources causing TAT are from the points defected during the epitaxy growth at low temperature which is not evitable and from the dangling bonds at the surface. Effective passivation method could reduce the traps at the surface, which results in increase the activation energy. For the E_A obtained in this study, the 250 µm in diameter devices without passivation has an E_A value of 0.16 eV that is lower than $E_g/2$ (0.23 eV for 11 % Sn devices), which seems to suggest a process of TAT and / or BTBT. Meanwhile, the devices with 3 nm GeON passivation shows an E_A value of 0.28 eV which is near $E_g/2$. This activation energy value means that the forward-bias current is dominated by diffusion and SRH components, and the leakage current is minimized.

Table 11. Extracted series resistance, shunt resistance, and dark current density at -1 V, and activation energy of 250 µm and 500 µm 11 % Sn photodiodes at 77 and 300 K.

Device	77 K			300 K			E_A (eV)
	R_S (Ω)	R_{Sh} (kΩ)	J_D @-1V (A/cm^2)	R_S (Ω)	R_{Sh} (kΩ)	J_D @-1V (A/cm^2)	
3 nm, 250 µm	14	1749	0.16	16	3.15	1.6	0.28
0 nm, 250 µm	47	5	1.13	24	0.72	2.98	0.16
3 nm, 500 µm	13	2.68	0.6	15	0.39	2.1	0.16
0 nm, 500 µm	30	10.5	0.39	25	0.27	1.6	0.14

The extraction method of activation energy based on the use of reverse saturation current only features current mechanism in the forward bias region where the reverse saturation current is calculated. The activation energy in the reverse bias region could be determined by plotting the Arrhenius reverse dark current under different applied bias. Figure 43 (a) and 43 (b) plot the extracted activation energy under -0.1, -0.5, and -1V applied bias and is noticeable that the activation energy decreases with the bias. This decrease can be explained by the presence of higher electric fields, which enhances the TAT and BTBT leakage contributions. Both samples with 3nm GeON passivation and without passivation exhibit two slopes of activation energy. The first slope region belongs to 77 – 140 K range while the second slope belongs to 180 – 300 K range. The sample without GeON passivation has very low activation energy value (<< $E_g/2$) regardless of temperature, in the range from 0.03 (-0.5 and -1 V) to 0.05 eV (-0.1 V) for the first slope region and from 0.004 (-0.5 and -1 V) to 0.005 eV (-0.1 V) for the second slope region. Such low activation energy (<0.1 eV) suggests a prevailing current mechanism from band-to-band tunneling. On the other hand, 3 nm GeON sample shows a significant increase in activation energy in both region. It is worth to point out that an activation energy of 0.25 eV was obtained at -0.1 V. This highest value is close to $E_g/2$, which favors SRH current mechanisms. It is likely that the passivation method using GeON is more effective to reduce leakage current at low reverse bias. While at -0.5 V and beyond, the current leakage is dominated by tunneling effect due to high doping of n-Ge / p-Ge and small bandgap of $Ge_{0.89}Sn_{0.11}$. Similar behavior was recently reported by using ozone oxidation to form GeO and GeSnO followed by ALD deposition of Al_2O_3 [57].

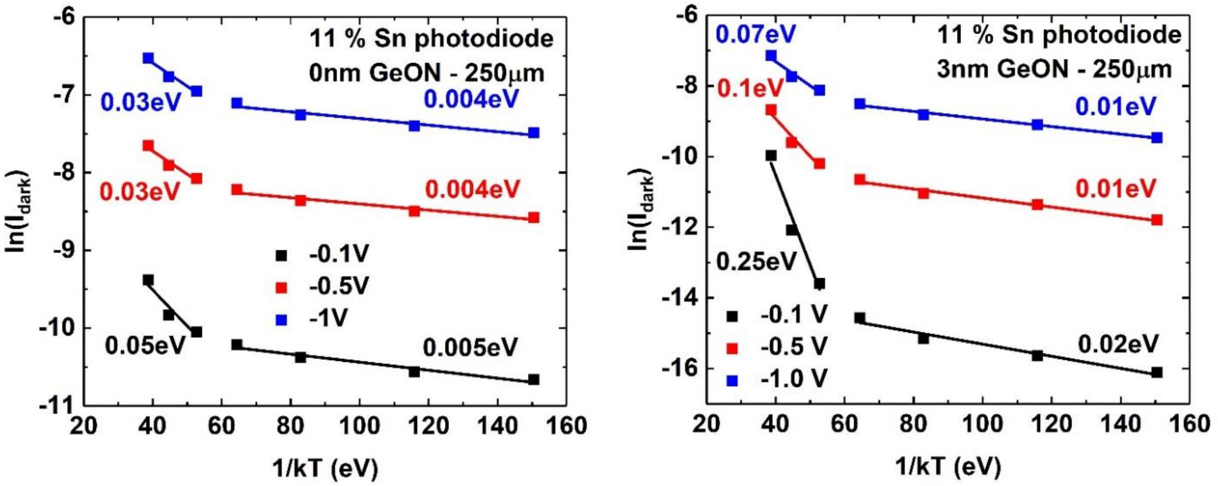

(a) (b)

Figure 43: Reverse dark current Arrhenius plot measured at -0.1, -0.5, and -1 V of 11 % Sn photodiodes with 250 µm in diameter and (a) 0 nm and (b) 3 nm of GeON passivation.

*Temperature dependent responsivity and specific D**

The responsivity characterization of 3 nm GeON sample was performed with 2 µm incident laser source. An optical chopper was connected to a lock-in amplifier where the change in voltage was manually read. Temperature dependent responsivity of 3 nm GeON passivation device was investigated and directly compared with controlled samples which do not have GeON passivation and was presented in chapter 4, as shown in Figure 44 (a) and 44 (b). Once again, the responsivity decreases as the temperature decreases. A peak responsivity of 0.37 A/W measured at -0.1 V and 300 K was obtained. This is slightly better than the reported value, 0.32 A/W, under similar condition. It is also equivalent with an EQE of 23 %. Besides, the responsivity of the sample with 3 nm GeON passivation at each temperature was improved from 0.21 to 0.24 A/W (77 K), from 0.23 to 0.27 A/W (100K), from 0.26 to 0.3 A/W (180 K), and from 0.32 to 0.37 A/W (300 K). This is likely due to enhanced photogenerated carrier collection efficiency from diffusion as a result of less surface recombination.

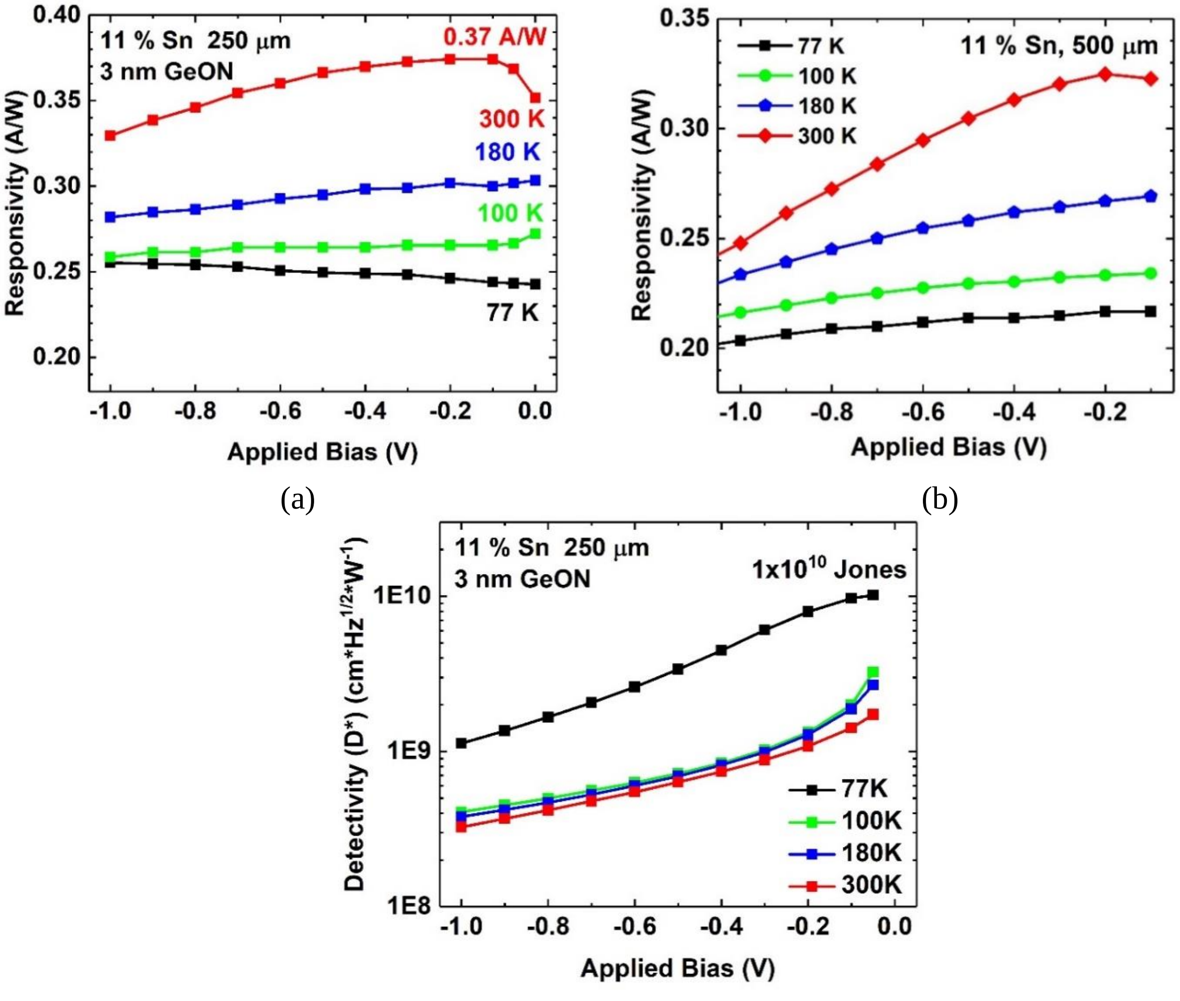

(a) (b)

(c)

Figure 44: Temperature dependent responsivity versus bias voltage measured at 2 μm of 11 % Sn photodiode with (a) 250 μm in diameter and 3 nm of GeON passivation and (b) (a) 500 μm in diameter and 0 nm of GeON passivation. (c) Temperature dependent D* versus bias voltage measured at 2 μm of 11 % Sn photodiode with 250 μm in diameter and 3 nm of GeON passivation.

Although responsivity is highest at room temperature, the specific D* is highest at 77 K where current density is smallest. As analyzed in previous chapters, D* is a function of responsivity, active areas, and reverse of square root of noise current, which is the prevailing factor. Therefore, as the temperature decreases, the D* increases. A peak D* of 9.7x10^{19} Jones was achieved at 77 K as shown in Figure 44 (c), which is twice larger than the one of the device without surface passivation.

The spectral D* of the 250 µm $Ge_{0.89}Sn_{0.11}$ photodiode with 3 nm of GeON passivation at 77 and 300 K and at -0.1 V was plotted with the one without passivation and commercial detector Ext-InGaAs, as shown in Figure 45. The peak D* at 2um of 3nm GeON device measured at 77 K is only 6 times less than Ext-InGaAs and is twice larger than the controlling device without passivation. The small red shift at 77 K of the device with passivation is contributed from smaller applied bias (-0.1 V) comparing with the one without passivation (-0.3 V). This discrepancy in cut-off wavelength near the band edge is associated with Franz- Keldysh effect.

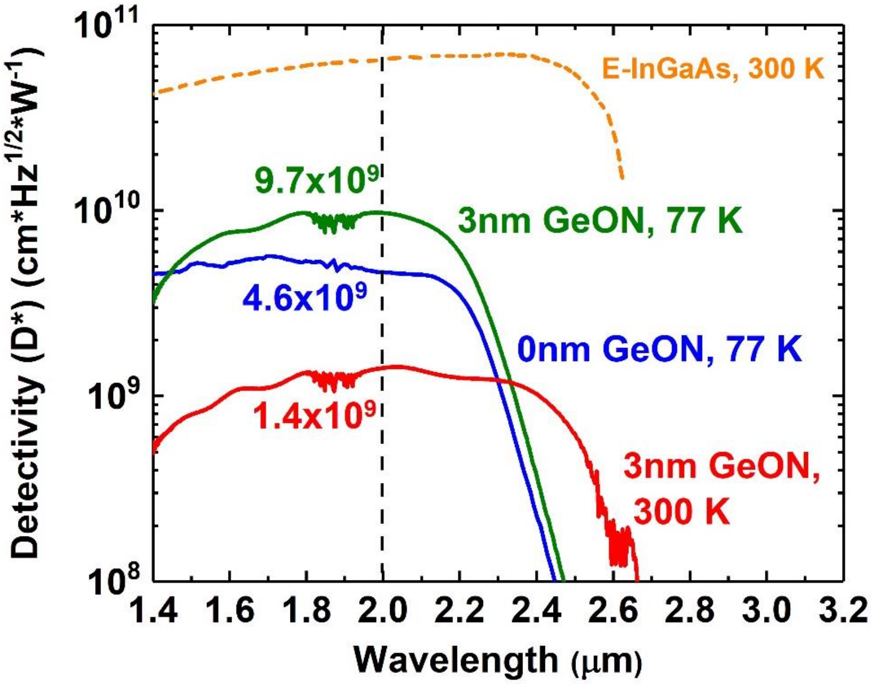

Figure 45: Spectral D* of the 250 μm $Ge_{0.89}Sn_{0.11}$ photodiode with 3 nm of GeON passivation measured with a voltage bias of -0.1 V at 77 K (green) and 300 K (red). For comparison, the D* spectra of commercial detector Ext-InGaAs and 250 μm $Ge_{0.89}Sn_{0.11}$ at 77 K without passivation (blue) are also plotted. The numbers indicate the values of D* at 2.0 μm.

5.2 Aluminum oxide on germanium tin oxide as surface passivation for GeSn photodetectors

5.2.1 Device fabrication

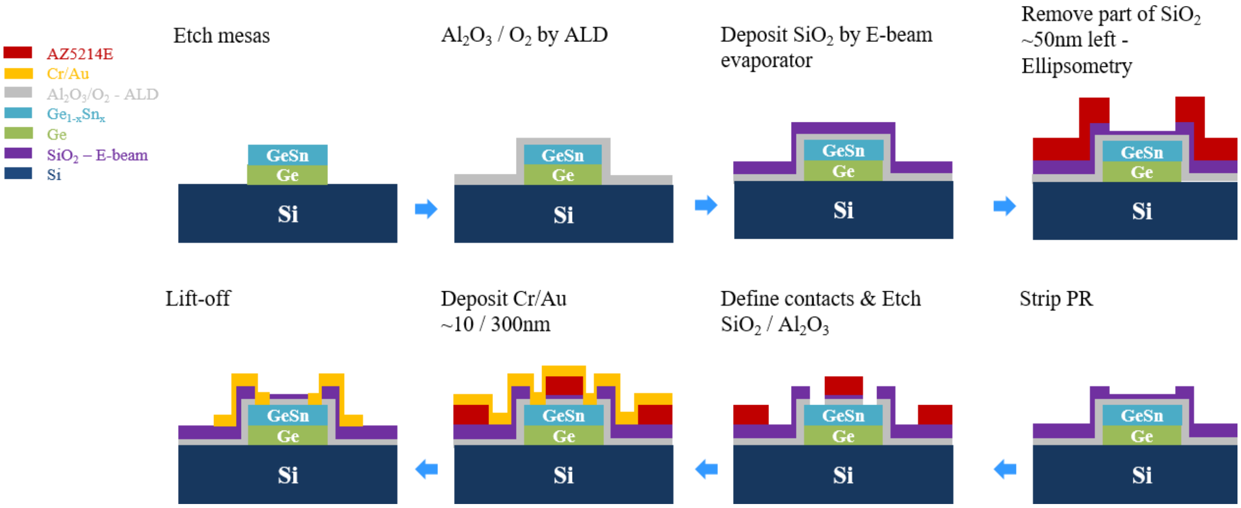

Figure 46: Fabrication process flow of thick film GeSn photoconductors with Al_2O_3 / Ge of 250 nm and with SiO_2 as dielectric layer

Figure 46 presents the fabrication process of thick film photoconductors with incopration of surface passivation. It involved six pair of samples with Sn composition of 11 %, 13 %, 16 %, 17.5 %, 20 %, and 22 %. Only one sample per pair was applied with surface passivation while the other one went through similar process without applying surface passivation layer. The later samples has been presented in chapter 3. The process began with formation of 500x500 μm^2 square mesas by using photoligthography and low temperature chemical wet etching. Photoresist, acting as a hard mask, was baked at 130^o C for 15 min. Detailed etching process was reported previously in chapter 3.

Before the deposition of surface passivation layer, a chemical pre-clean step was performed using HF : HCl (1:1). This chemical solution has been proven as a very effective method to clean Ge and GeSn surface due to the volatibility of SnO and GeO in HF : HCl [109]. Cleaned samples were immediately loaded in the ALD chamber that was preheated to 200^o C. In contrast with ozone precusor, higher temperature is prefered due to Ge-O bonding diffulty in the oxidation process for germanium and germanium tin using oxide precursor. However, processing temperature of 300^o C and above has led to Sn segregation to the samples surface escpecially for our case where 5/6 samples have high Sn composition from 13 %. Therefore, a temperature of 200^o C was selected as the operating tempearture for oxidation process and deposition of Al_2O_3. After exposing samples with consecutive 100 cycles of Ar and O_2, 10 nm of Al_2O_3 was deposited by using trimethylaluminum (TMA) and water precursors at 200^o C. The 2nd batch of six samples was loaded in the same ALD chamber and was only exposed with identical temperature condition.

The fabrication process resumed with the deposition of SiO_2 using electron beam evaporator for all samples with and without passivation as shown in Figure 47 (a). The thickness of SiO_2 was kept in the range of 400 – 600 nm, which is 30-40 % of the etching depth. The active areas were immediately defined on top of the mesas, followed by oxide opening step by using BOE (for samples without passivation). Normally, the oxide layer would be fully opened so that the metal contacts could be properly formed. However, that would result in removing the very thin surface passivation layer, which contradicts with the defined purpose. Therefore, two-steps oxide opening was done with careful thickness calibration by Ellipsometry. The first step will leave approximately 40 nm of SiO_2 after exposing with BOE solution, which is sufficient to protect the underneath passivation layer, as shown in Figure 47 (b). This 40 nm of SiO_2 along with 10 nm of GeSnO / Al_2O_3 were later removed right at 3rd mask alignment step defining the metal contacts, as shown in step 6 of Figure 6 and in optical image of Figure 47 (c). Since the SiO_2 layer surrounding the mesas were partially etched away at the same time, it is important to control the etching time in BOE solution. The thickness of SiO_2 in the first etching step was confirmed by subtracting the remaining thickness of SiO_2 provided by Ellipsometry measurement (449 nm) and by Dektak (467 nm) from the original thickness (490 nm).

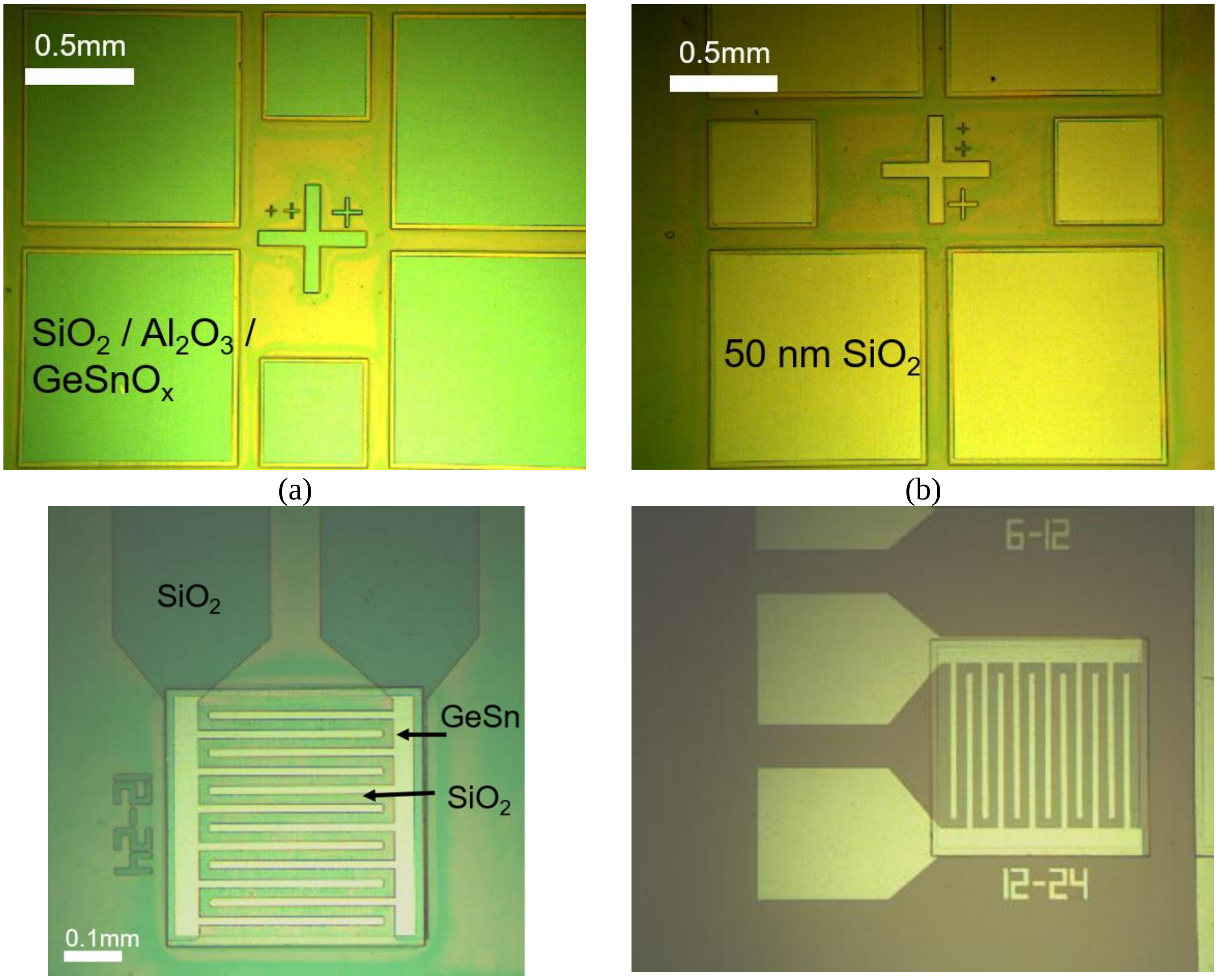

(a) (b)

(c) (d)

Figure 47: Top view microscope image of the photoconductor surface (a) after depositing SiO_2 on passivation layer (step 3), (b) after 1st SiO_2 opening step (step 4) with only 50 nm of SiO_2, (c) after 2nd SiO_2 opening step (step 6), and (d) after lift-off (step 8).

XPS characterizations were performed to determine the etching time of the remaining SiO_2 and passivation layer. Intensity (count/s) versus the binding energy of Al2s was plotted in Figure 48 (a) (13 % Sn) and Figure 48 (c) (11 % Sn) while Figure 48 (b) (13 % Sn) and Figure 48 (d) present the intensity versus the binding energy of Si2p for 10 and 15 s that the samples were exposed in BOE solution. In fact, Al_2O_3 and SiO_2 layer of 13 % Sn sample were mostly removed after 15 s dip due to quick fall of Al2s and Si2p signals. For the case of 11 % Sn sample, the intensity of Si2p decreased while the one of Al2s increased as the etching time increased from 10 s to 15 s. This concludes that part of SiO_2 layer was removed and Al_2O_3 layer was intact. Therefore, 11 % Sn sample was further processed in BOE with an extra 2-3 s considering a safe SiO_2 thickness for the deposition of metal contacts.

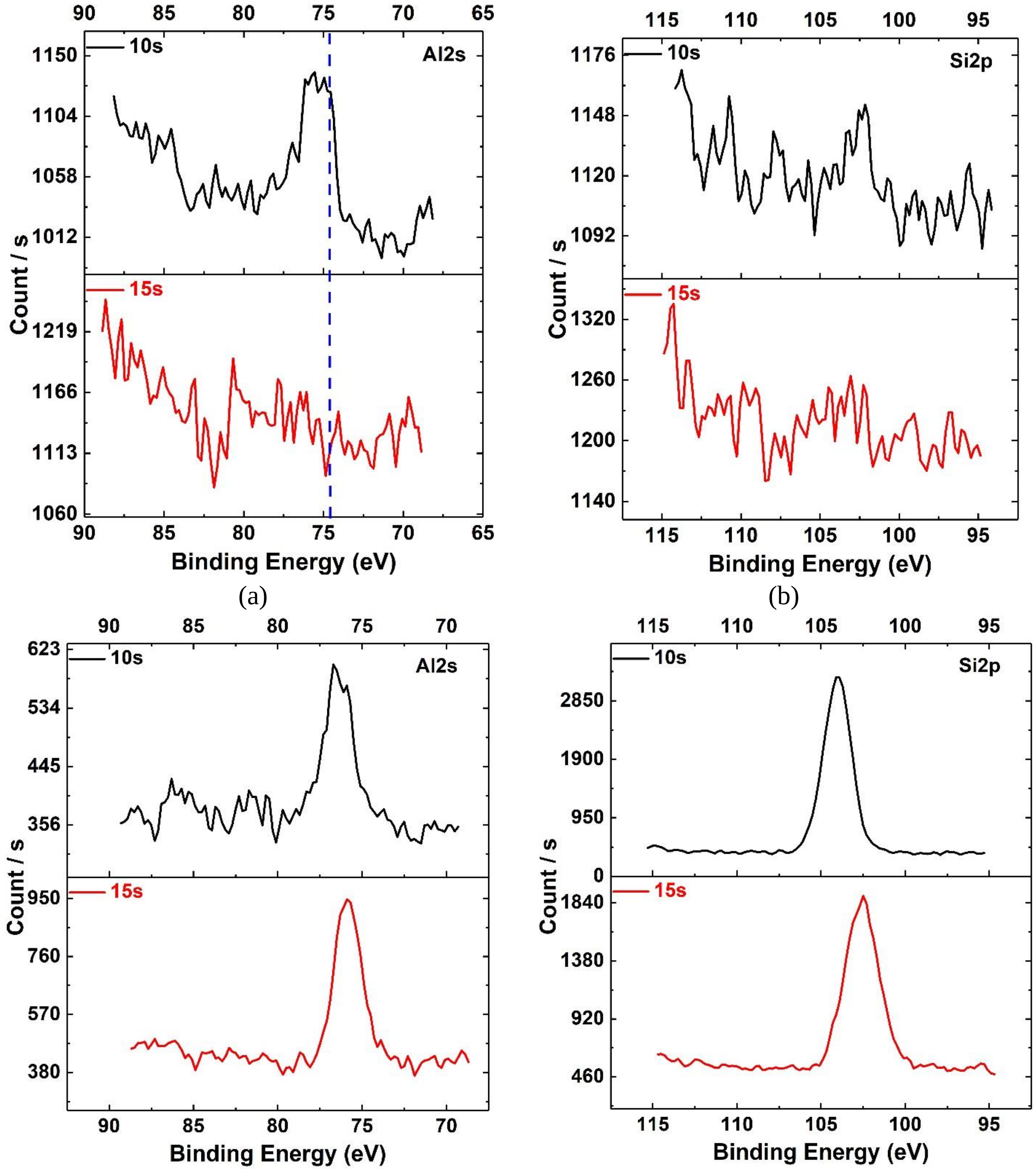

(a) (b)

(c) (d)

Figure 48: (a) Al2s spectra and (b) Si2p spectra of 13 % Sn sample after wet etching in BOE solution for 10 and 15 s. (c) Al2s spectra and (b) Si2p spectra of 11 % Sn sample after wet etching in BOE solution for 10 and 15 s.

Knowing the etching time of the 2nd etch step, metal contacts were defined by third photolithography mask followed by a wet etch in BOE for 17 s for samples with passivation layer. The fabrication process ended with metal deposition of 10 / 300 nm Cr /Au and lift-off in PG remover heated at 80° C. Top view of metalized devices was shown in Figure 47 (d). XPS was once again performed to (1) verify that the remaining SiO_2 layer and the passivation layer were removed and (2) determine the oxide state of germanium / germanium tin layer of the active areas. The XPS beam was focused on the open area of 11 %, 13 %, 20 %, and 22 % Sn coplanar devices. Figure 49 (a) plots the intensity versus the binding energy of Al2s atoms and Figure 49 (b) presents the one of Si2p atoms. Based on the intensity of Al2s and Si2p, SiO_2 and Al_2O_3 layer were mostly removed only for samples with 13 % and 22 % Sn. This suggests that the SiO_2 layer deposited by electron-beam evaporator is not uniform. Figure 49 (c) summarizes the core spectra of germanium (Ge3d) using 11 %, 13%, 20 %, and 22 % Sn samples. The Ge3d binding energy of four samples mainly centered at 30.3 eV with a small broadening shifting towards higher energy level. This chemical shift, roughly 2.3 eV, signals the presence of the oxide. The oxide should be formed in the exposure with oxygen source in ALD chamber since air oxidation forms higher oxides of Ge [107] and our samples were treated with HF : HCl solution which is very efficient in breaking the nature bonding of Ge-O / Sn-O. In general, there are four well-known oxide states for germanium which are 1+, 2+, 3+, and 4+ corresponding with a shift in binding energy of 0.8, 1.8, 2.6, and 3.4 eV, respectively [107], [110]. Obtaining higher oxidation states requires energy to break more Ge bonds, which can be supplied by thermal energy or activated oxygen. The 2+ and 4+ are the most favorable oxidation state of Ge due to high stability of Ge=O bond geometry and two-bridge bonded oxygen atoms. Studies has shown that emission of 3+ state was observed in addition to 2+ and 1+ states at 200° C, which is similar with our study despite of a low intensity. Further optimization on the flow, temperature, and pressure would improve the forming of Ge-O bond and quality of the passivation layer.

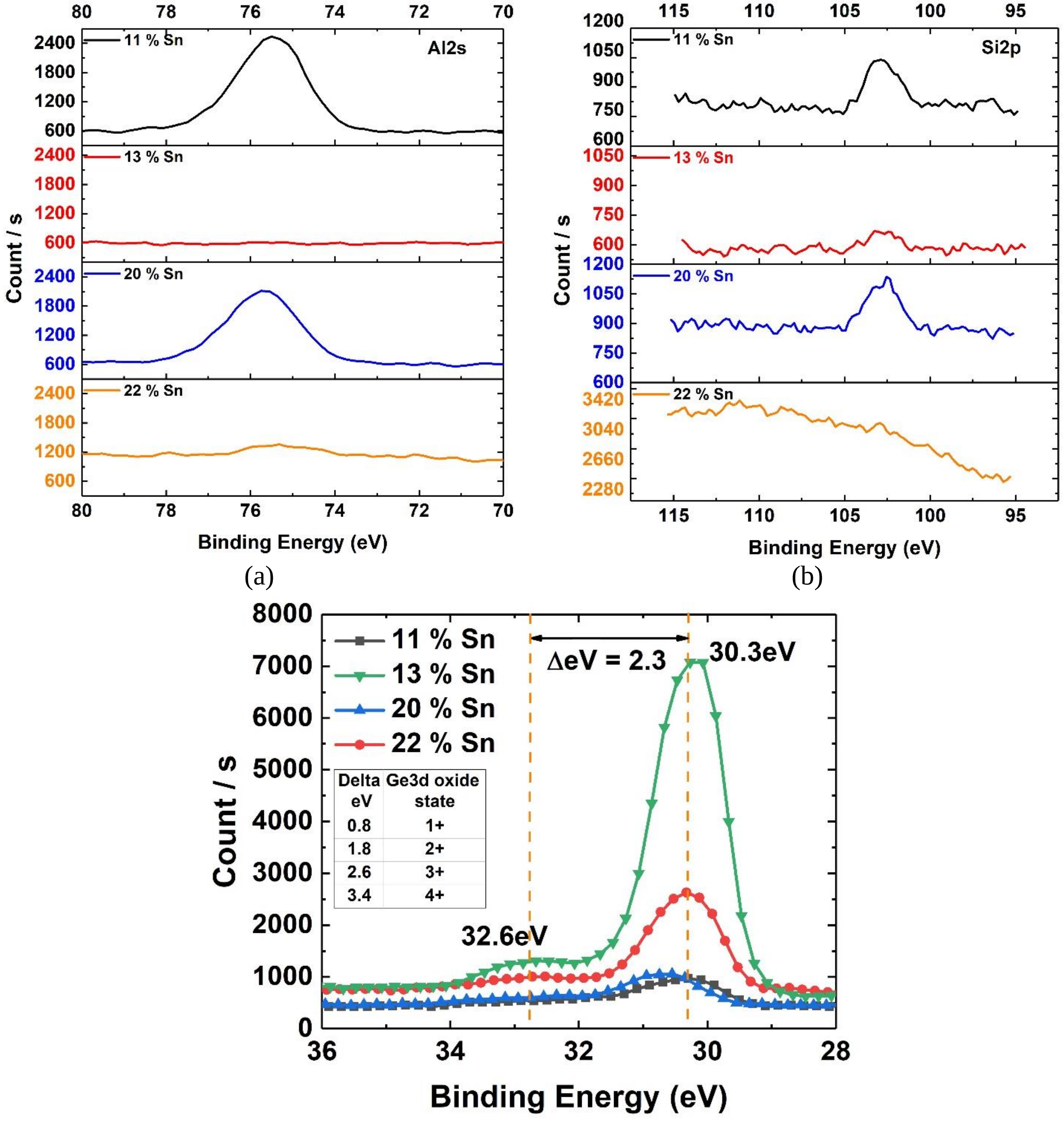

Delta eV	Ge3d oxide state
0.8	1+
1.8	2+
2.6	3+
3.4	4+

(a)

(b)

(c)

Figure 49: (a) Al2s spectra, (b) Si2p spectra, and (c) Ge3d spectra of 11 %, 13 %, 20 %, and 22 % Sn samples after wet etching in BOE solution for 15-17 s. The small shift towards longer binding energy level in (c) signals the existence of germanium oxide.

5.2.2 Device characterization

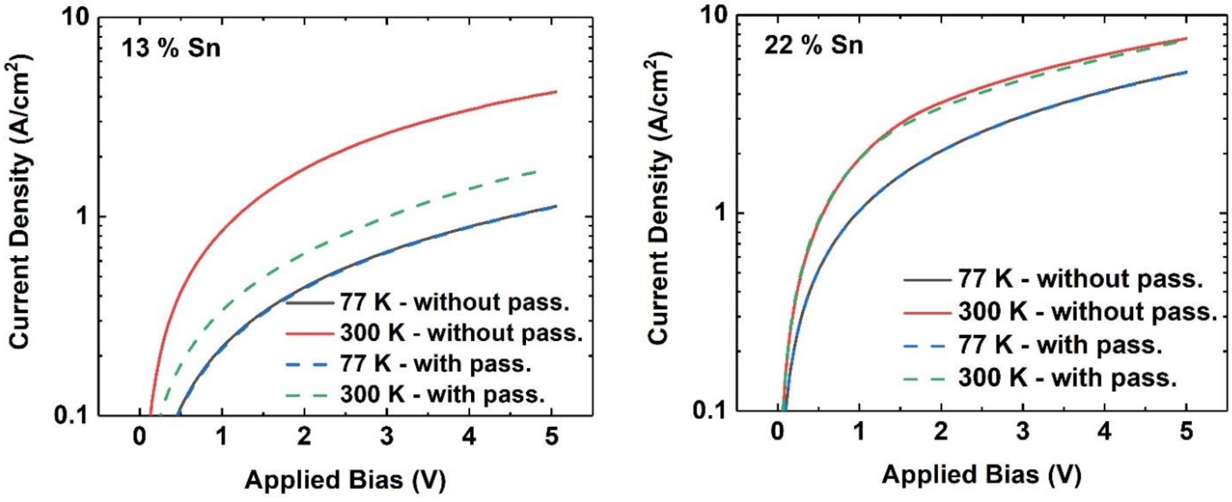

(a) (b)

Figure 50: Current density-voltage characteristic of (a) 13 % Sn and (b) 22 % Sn sample with (dash) and without passivation (solid) measured at 77 and 300 K.

Current-voltage measurements of 11 %, 13 %, 16 %, 17.5 %, 20 %, and 22 % Sn photoconductors samples with and without passivation was performed at 77 and 300 K. The current density of all samples measured at 1 V was extracted and summarized in Table 12. As Sn composition increase, the current density increases as a result of more available thermally excited carriers. As suggested by XPS spectra presented above, 13 % Sn sample has better surface passivation layer, followed by 22 % Sn sample. The current density of 13 % Sn photoconductor was reduced from 0.85 A/cm^2 (without passivation) to 0.4 A/cm^2 (with passivation) measured at 300 K and 1 V, as shown in Figure 50 (a). A slight reduction in current density from 1.93 to 1.88 A/cm^2 was also observed for 22 % Sn photoconductor sample at 300 K. The current density at 77 K remained the same. For the case of 11 %, 16 %, 17.5 %, and 20 % Sn, there is no clear discrepancy between samples with passivation and those without passivation, as shown in Figure 50 (b). This is in agreement with XPS Ge3d spectra where Ge-O was not clearly formed and hence only Al_2O_3 was deposited for samples with passivation. In addition, the very thin layer of Al_2O_3 /

SiO_2 was not completely removed during the fabrication process for some samples, which in turn slightly increased the resistance of those devices.

Table 12. Extracted current density at 1 V of 11 %, 13 %, 16 %, 17.5 %, 20 %, and 22 % Sn photoconductors measured at 77 and 300 K.

Temperature	Al_2O_3 / GeO_x	Current density at 1 V (A/cm^2)					
		11 % Sn	13 % Sn	16 % Sn	17.5 % Sn	20 % Sn	22 % Sn
77 K	With	0.25	0.22	0.51	0.88	1.03	1.03
	Without	0.27	0.22	0.47	0.72	0.94	1.03
300 K	With	0.38	0.4	1.64	1.3	1.56	1.88
	Without	0.31	0.85	1.24	1.16	1.49	1.93

Temperature dependent responsivity of 11 %, 13 %, 16 %, 17.5 %, 20 %, and 22 % Sn photoconductor samples with and without passivation was characterized at 2.0 µm using incident laser source and from 77 to 300 K. Representative curves of responsivity versus voltage using 13 % and 22 % Sn photoconductor samples with and without passivation were presented in Figure 51 (a), 51 (b), 51 (c), and 51 (d), respectively. It is expected to observe an increase in responsivity as the applied bias increases and as the temperature decreases. A peak responsivity of 0.2 A/W was obtained at near 5 V for those samples. However, samples with and without passivation do not show distinct enhance in responsivity.

In summary, the surface passivation technique using oxide as precursor to oxidize germanium surface followed by a deposition of Al_2O_3 in an ALD system has been demonstrated on high Sn composition photoconductors. The responsivity of samples with and without passivation is similar while the 13 % Sn sample with passivation shown a reduction in current density at 300 K. XPS spectra of Ge3d also revealed the existence of germanium oxide for that sample. Further optimization of the deposition recipe and the fabrication process such as increase in depositing temperature, a replacement of oxide with ozone precursor, and deposition of the SiO_2

layer by using PECVD would improve the quality of the passivation layer and hence further improve GeSn photoconductor performance.

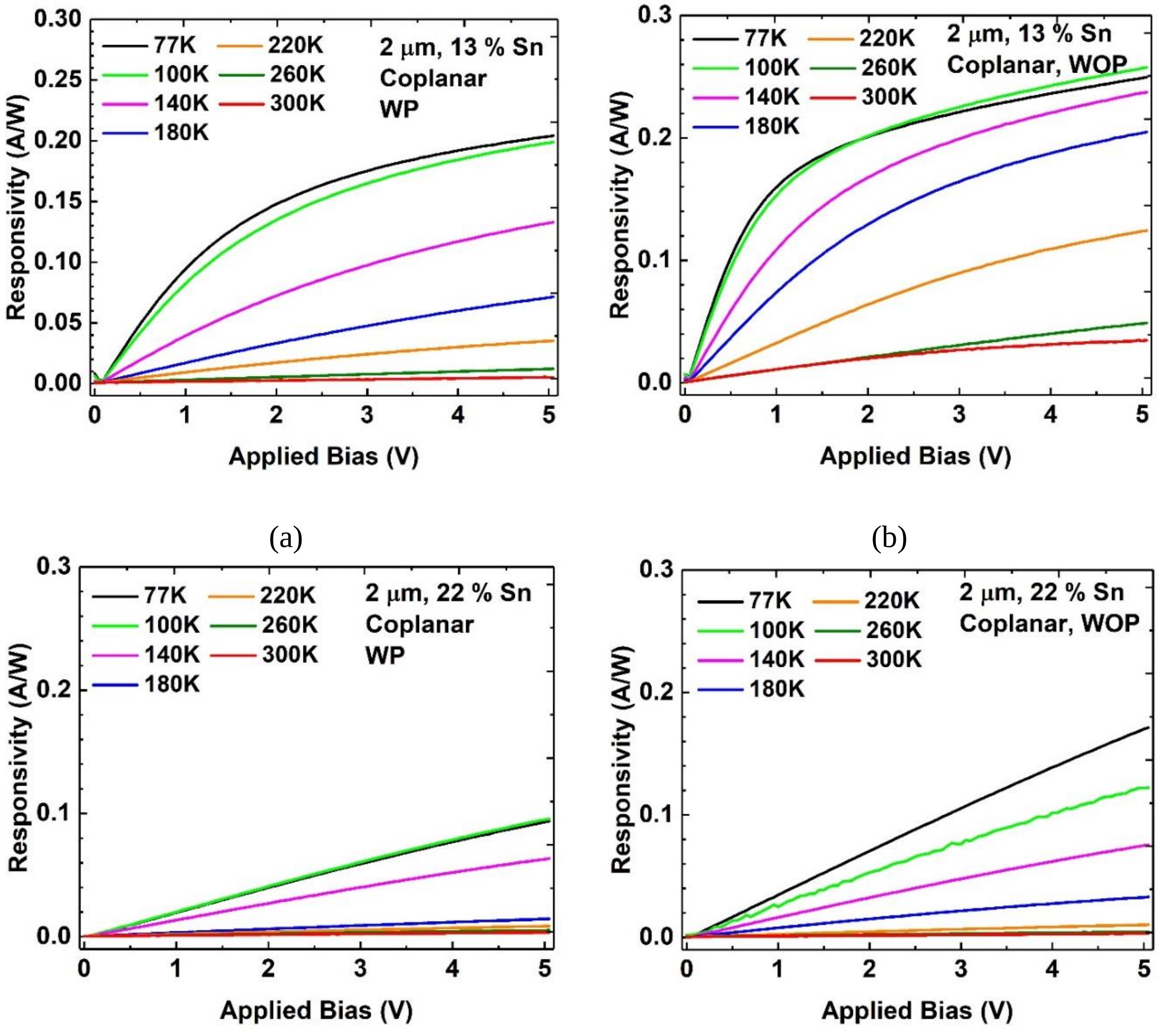

(a) (b)

(c) (d)

Figure 51: Temperature dependent responsivity measure at 2.0 μm of (a) 13 % photoconductor with passivation, (b) 13 % Sn photoconductor without passivation, (c) 22 % Sn photoconductor with passivation and (d) without passivation.

Chapter 6: Demonstration of a SWIR image

The development of IR imaging sensor began in 1950s where capturing images relied on scanning single element detector and linear arrays detectors. An image is generated by scanning the scene across the linear array. This early system represented for the first-generation imagers. It utilized InSb and PbSe in the MWIR region (3–5 µm), and Ge:Hg in the LWIR region (8–14 µm) for military purpose. The Ge:Hg detector arrays required two-stage cooler to operate at 25 K and to provide high image quality. It was later replaced by the well-known narrow bandgap material HgCdTe that only requires one stage cooler to operate at 80 K. The number of elements in first generation detector arrays was either 60, 120, or 180 [11], [111].

The second-generation sensor started in 1980's. It typically has more elements ($>10^6$) and each individual element, called "pixels", is configured in two-dimensional arrays at the focal plane of an imaging system. Such assemblage of pixels is called focal plane array (FPA). The major factor that distinguishes second-generation with the first-generation IR sensor is the presence of staring systems, which includes the multiplexing functions in the focal plane. Fully two-dimensional array formats were introduced in early 1990's such as HgCdTe arrays of 64×64 and 256×256 elements for LWIR, and InSb arrays of 480×640 elements for MIR. By the late 1990's, InGaAs linear array of 256, 512, and 1024 elements was fabricated for environmental sensing from 0.8 to 2.6 µm [11], [111].

There is no clear definition for third-generation IR sensors which emerged at the beginning of the millennium. In the common understanding, third-generation IR systems provide enhanced capabilities such as larger number of pixels, higher frame rates, better thermal resolution, as well as multicolor functionality and other on-chip signal-processing functions [112].

For the last couple of decades, array size of IR FPAs has been revolutionized with exponential increase rate. As illustrated in Figure 52, FPAs have the same growth rate as dynamic random-access memory (DRAM) ICs which had a double growth rate approximately 18 months. However, FPA size was behind the one of DRAM by about 5–10 years. Charge coupled devices (CCDs) have the largest array size of 100 M pixels, followed by PtSi, InSb, HgCdTe, and InGaAs. The largest CCD color arrays, made by Dalsa, have approximately 25 megapixels, with a pixel size of 12 μm and a chip size over 60 mm on a side [111].

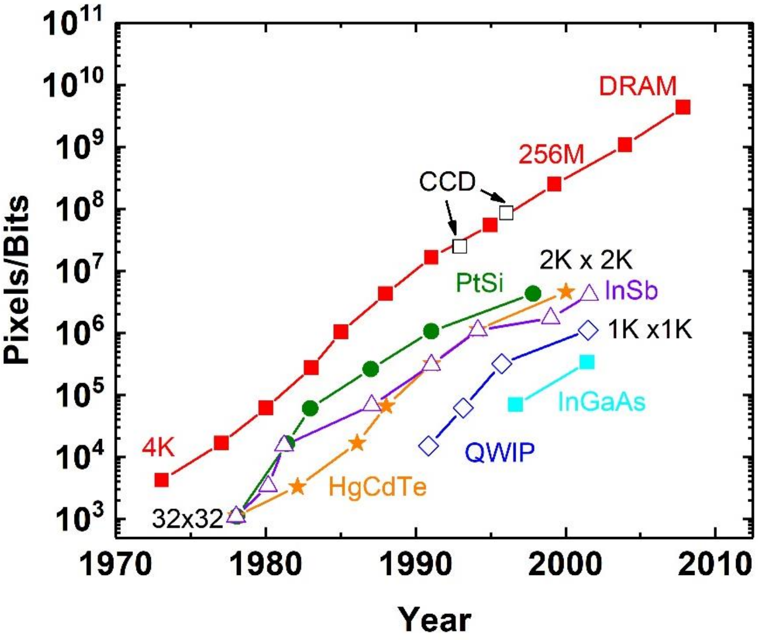

Figure 52: Replotted trends of array format size over years [112].

In fact, the fundamental limit of a pixel size is determined by diffraction: $d = 2.44\lambda f$ where d is the diameter of the spot, λ is the wavelength, and f is the f-number of the focusing lens [113]. As an example, a detector operating in the 5 μm wavelength has a minimum detector size of 25 μm using common f/2.0 optics. For SWIR, pixel size will shrink accordingly. Using the same optics, a detector operating at 2.0 μm can use detector pixels as small as 10 μm. Besides, the pixel size was also constrained by the perimeter of readout circuit wafer. Since the silicon industry has standardized on a field size of 22×22 mm^2 for its lithography tools, the size of each pixel should not exceed 18 µm to be fitted in a 1024×1024 array. To obtain an FPA with larger pixel counts, "stitching" technique was employed [11], [113].

There are multiple methods to classify the architectures of FPAs among which monolithic and hybrid are the most common one. In the monolithic approach, photon detection and circuit readout or multiplexing are performed in a single piece device without using any external circuit connection. As a result, the fabrication steps and difficulties are significantly reduced, leading to a cost reduction and higher yields. So far, the monolithic arrays on Si are the most mature technology in this approach with two generic device systems available in the market e.g. charge coupled devices (CCDs) and complementary metal-oxide-semiconductor (CMOS) sensors. In CCD sensor, the charge is first integrated at the pixel and subsequently transferred to limited number of outputs (usually one node) where the voltage signal is converted and collected by external circuit. Therefore, high image quality could be achieved thanks to high output uniformity. The CMOS sensor has a more interesting way to address data. Each pixel performs its own charge-voltage conversion and can be individually addressed. It also includes amplifiers, noise-correction, and digitization circuits which results in a complex structure and a reduction in the active area for sensing. Although it affects the output image due to less uniformity (fill factor, which is ratio of a pixel's light sensitive area to its total area, is reduced from 80 % to 30-50 % [11]), CMOS sensor has an advantage in fabrication cost with available CMOS foundries.

In a hybrid approach, detectors and multiplexers are fabricated separately in different substrate and could be optimized independently. Therefore, the fill factor near 100 % is achievable and there are more room for multiplexer chip. The detector and multiplexer are connected via the flip-chip bonding technique with the use of indium bumps or loophole interconnection. Both methods encounter difficulties in making small pixel pitches less than 10 µm since high yield is a required standard. On the other hand, light illumination could either aligned to top front or to back side. The back-side illumination is preferred to avoid metallization areas from the multiplexer chip (front size). The opaque areas and substrate thickness are thinned to the range of 10-20 µm to avoid crosstalk and maintain sufficient quantum efficiency [113].

Si-based GeSn detector system is strongly believed to be a non-expensive high performance solution for IR imager supported by the facts: (1) high responsivity and specific D*, (2) extended cut-off wavelength from SWIR to MIR up to 4.0 µm, (3) group IV materials growth on Si wafer which enables the ability to be manufactured in large-scale in CMOS foundry, and (4) monolithic integration on Si photonics. In addition, in 2016, the concept was first successfully demonstrated by Chang *et al.* A GeSn-based 320×256 focal plane array imaging sensor with spectra response in the 1.6-1.9 µm range was used to capture a tungsten light bulb although the FPA was grown on Ge substrate [52]. In this chapter, a single-element Si-based GeSn photodetector (11 % Sn photodiode and 11 % Sn photoconductor with spectral response up to 2.8 µm) will be used to demonstrate the imaging capability in SWIR. A three-dimensional stage was used to control the movement of a single detector in serpentine fashion to mimic the function of an array. It is a milestone showing that the GeSn material becomes more mature since the first introduction and Si-based GeSn detectors have enormous potential to compete with commercially available detectors in the SWIR and MIR.

Details growth method, material structure and characterization, and devices fabrication of 11 % Sn photoconductor and 11 % Sn photodiode that were used in this chapter were presented in chapter 4 and 5.

6.1 Measurement setup

The IR imaging process using a single Si-based GeSn photodetector is a consecutive sequential of pixel movement and signal detection. To mimic the function of an array detectors, a single pixel movement employed a serpentine pattern with a time delay of 0.25 ms in between each move as shown in Figure 53 (a). The array size was defined by providing y-length and z-length. The choice of scan step, which is the center-to-center distance between two consecutive position, is important and depends on the single pixel dimension.

The single pixel was first wired-bonded on a chip carrier that was attached to a Janis cryostat system mounting on a z-stage of 3D-stage. At the start of each measurement, the stage was programmed to move to a home position which is equivalent to the origin position of z-axis (vertical) and y-axis (horizontal). Next, z-stage and y-stage were driven to the starting coordinate where the first responsivity signal was immediately captured by using a lock-in amplifier and an integrated chopper set at 380 Hz. The incident light could either be from a 2.0 µm laser source or a white light source with a wavelength range of 360-2400 nm (HL-2000 model from OceanOptics). Subsequently, the pixel was moved to the second position.

Figure 53 (c) and 53 (d) plot the optical setup of transmission and reflection mode. The beam spot size is set to be larger than the object. In the transmission mode, the incident light (2.0 µm laser source) was shined directly to the object which is placed in parallel with the detector. The single pixel detector will collect the shape of the object. In the reflection mode, the white light source was aligned to a 50/50 beam splitter where the object is attached. The choice of white light source eased the calibration process. The reflected surface image of the object was collect by the single pixel. An optical filter of 1.6 µm was also used to remove the wavelength above 1.6 µm.

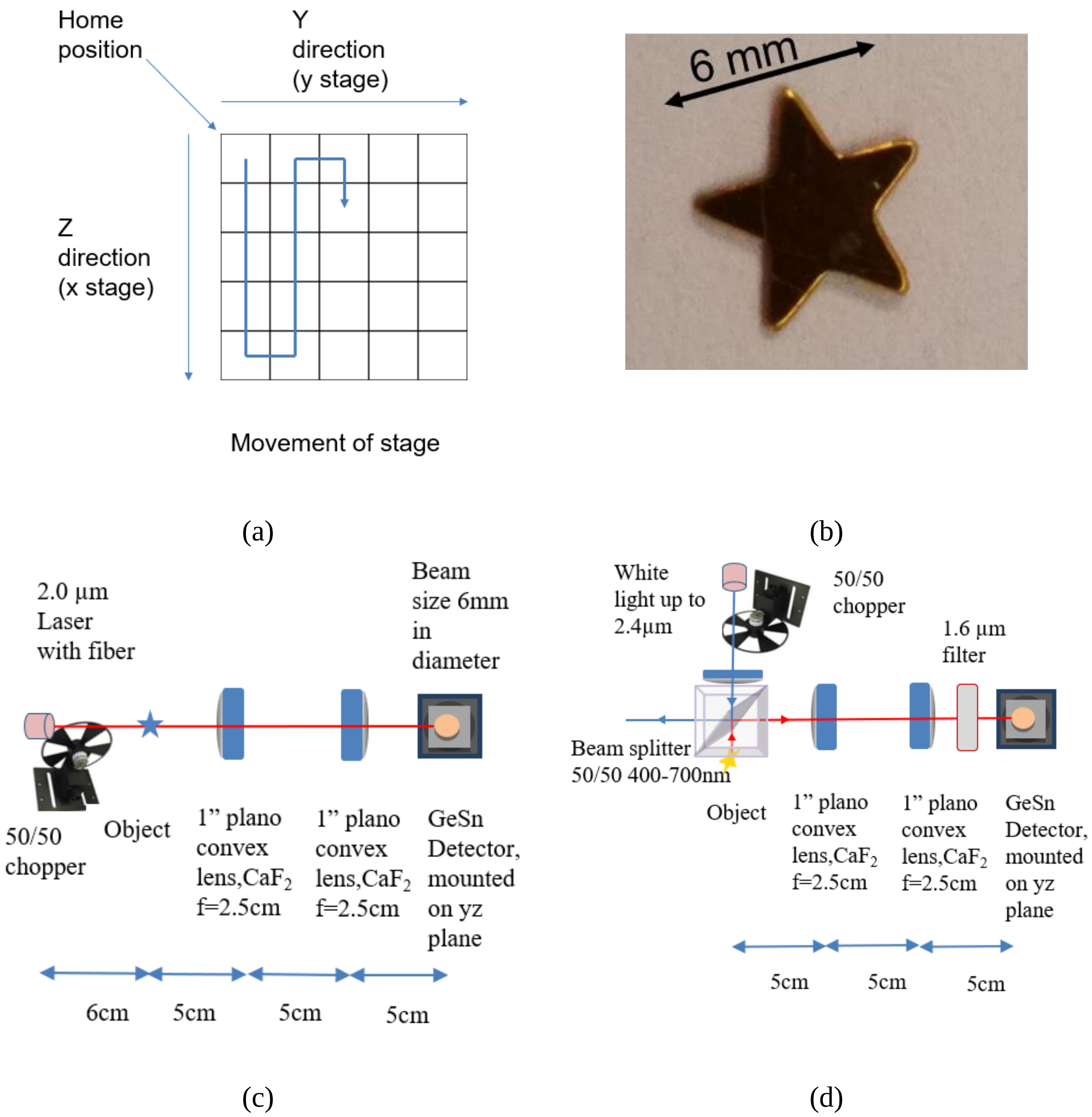

Figure 53: (a) Movement pattern of the single element detector driven by programmable 3D-stage. (b) Metal-coated star with 6mm length. (c) Transmission mode setup. (d) Relfection mode setup

6.2 Transmission mode

Transmission mode experiment was first conducted to demonstrate the IR imaging capability of single pixel Si-based GeSn photodetector due to its simplicity of optics and material of the object. In this experiment, the object is a star covered by aluminum foil, which prevents the penetration of IR wavelength. A 500 μm in diameter photodiode of 11 % Sn was used to capture signal at 77 K and to replicate an array of 41×41 elements with a scan step of 250 µm. A total delay time of 0.55 s between two consecutive positions was selected.

As the incident beam spot size is larger than the object, the captured image will include the shape of the object and part of the incident light spot, which could be considered as the background. Therefore, the beam spot image without object was captured and was utilized to eliminate the background by normalizing the signal from the image with object and the one without object. The incident 2.0 µm laser source's beam spot was plotted in contour mode in Figure 54 (a). Figure 54 (b) presents the image of the star object after eliminating the background with clear vertices.

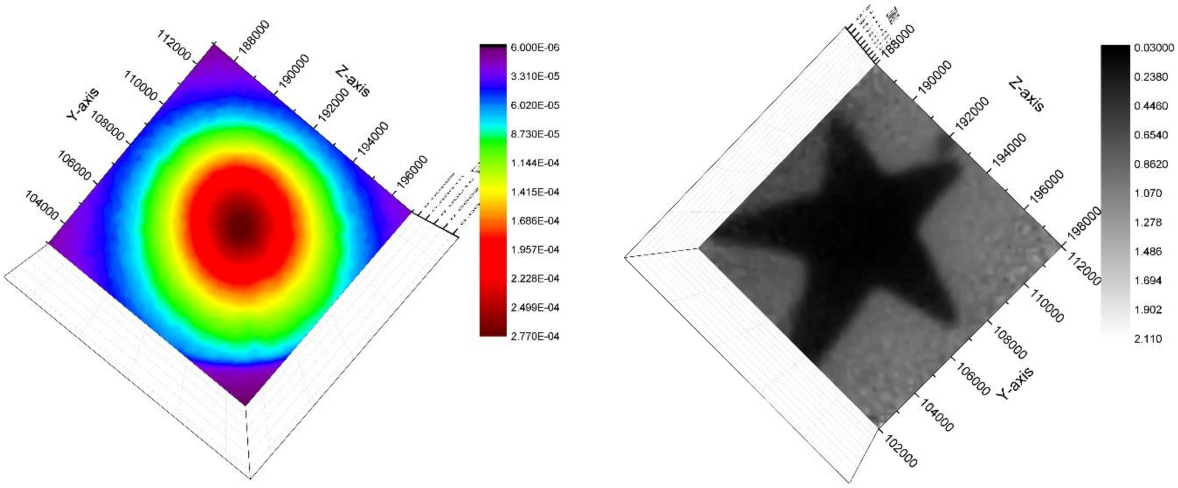

(a) (b)

Figure 54: (a) Beam profile of 2.0 µm laser incident light. (b) Image of the star using transmission mode and 2.0 µm laser.

6.3 Reflection mode

Reflection mode is a common method to provide the image at the surface of the object. The demonstration of IR imaging started with a metal-coated star as the object with a dimension of 6 mm each side. A 500 µm in diameter photodiode of 11 % Sn was used to capture signal at 77 K and to replicate an array of 71×71 elements with a scan step of 100 µm. Similar setting of delay time (0.55 s) was selected and filter was not applied. Figure 55 (f) shows the image of the star's surface after 40 minutes of scanning using a single pixel detector. Such a long scanning time is not efficient for capturing a larger area. The scanning time could be reduced either by increasing the scan step which sacrifices the resolution of the image or by decreasing the delay time which could cause image distortion. In this study, the delay time was modified to provide a more optimized scanning time without significantly reducing the image quality.

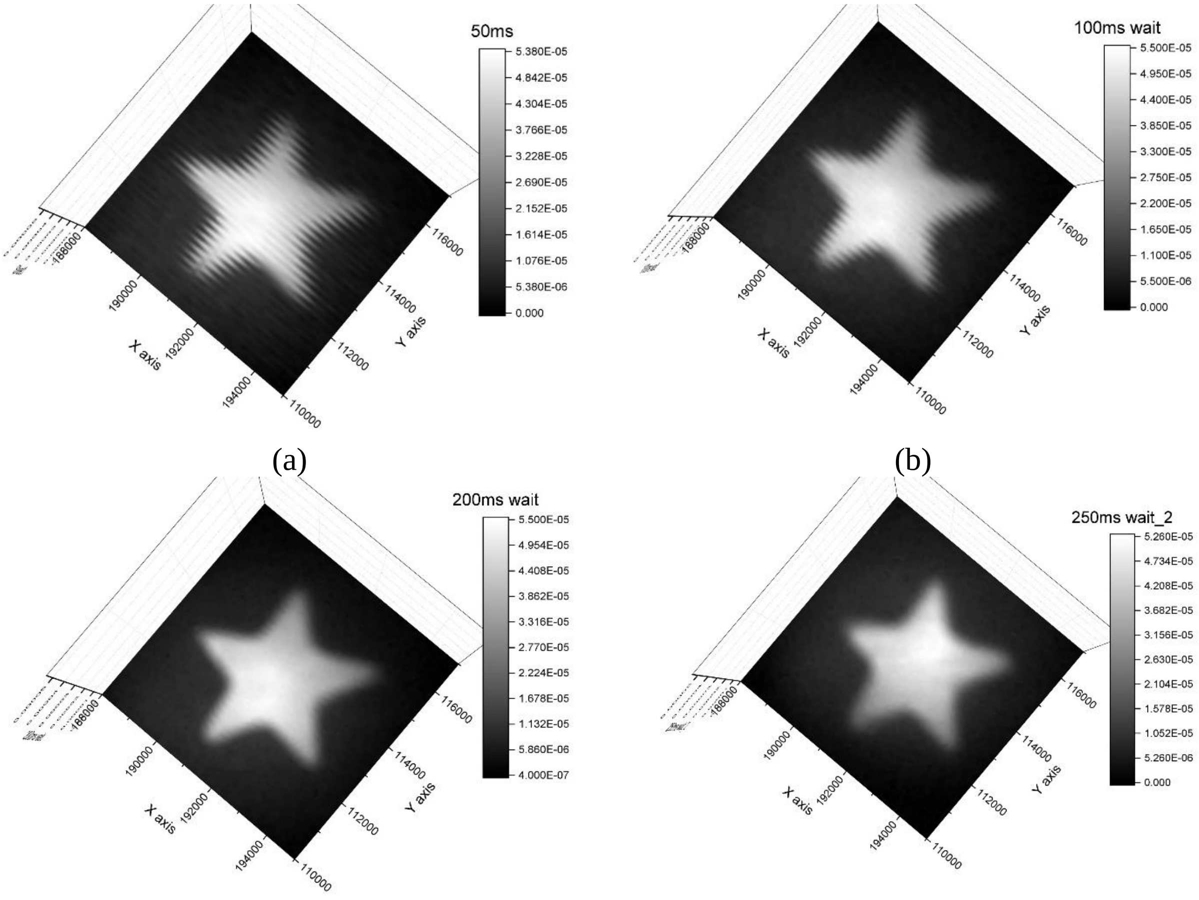

(a) (b)

(c) (d)

Figure 55: Image at the surface of the star using a white light source and 11 % Sn photodiode with different setting of delay time ranging from (a) 50 ms, (b) 100 ms, (c) 200 ms, (d) 250 ms, (e) 300 ms, and (f) 500 ms.

Figure 55 (Cont.)

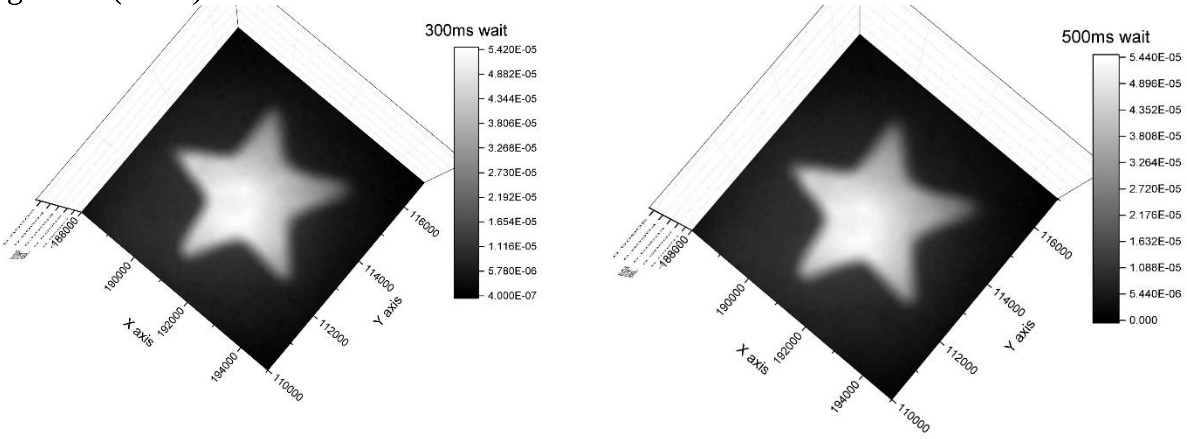

(e) (f)

Figure 55 (a), 55 (b), 55 (c), 55 (d), 55 (e), and 55 (f) depict the images of the object for 50, 100, 200, 250, 300, and 500 ms delay time, respectively. Image distortion was observed when the delay time is approximately 200 ms or less. In addition, there is no clear difference for the case of 300 ms or 500 ms delay time. The 250 ms case provides an acceptable image quality with a total scanning time of 20 minutes, which is half of the original setting. Therefore, the 300 ms delay time is a good choice for image quality while the option of 250 ms delay time is best for scanning time.

Further scans were collected with the aid of a 1.6 μm filter to reduce the majority contribution from visible light. As a result, the images of the star were successfully captured in the SWIR using 11 % Sn photodiode at 77 and 300 K, as shown in Figure 56 (a) and 56 (b). It is as expected to observe a better image quality at 77 K due to higher D* value.

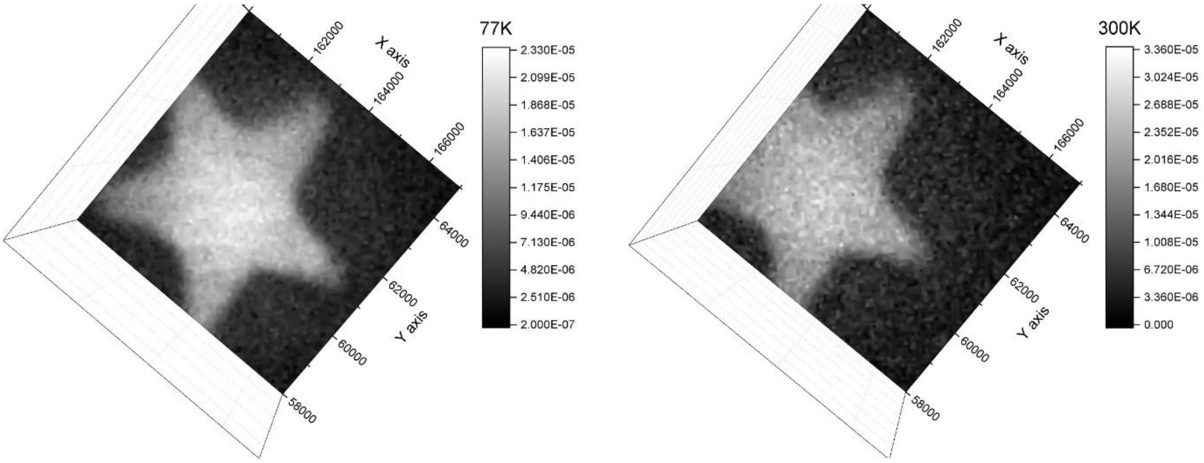

(a) (b)

Figure 56: Image at the surface of the star using white light source and reflection mode measured by 11 % Sn photodiode at (a) 77 K and (b) 300 K with the aid of 1.6 µm filter.

The demonstration of IR imaging capability resumed with the use of 11 % Sn photoconductor. The measurement was conducted at 77 K where the 11 % Sn photoconductor reach its peak D* to reproduce an image of a gift card bar code, a more common object in daily life. The four digits 4-5-8-6, marked by red circle as shown in Figure 57 (a), was successfully captured as a reverse image in Figure 57(b). Further optimization in optics would significantly improve the image quality.

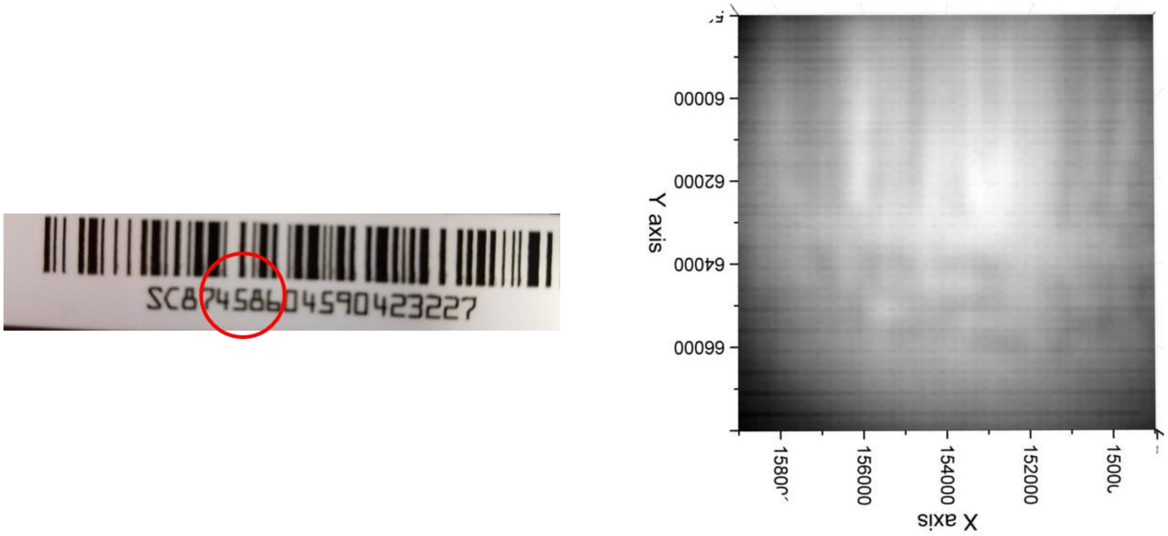

(a) (b)

Figure 57: (a) Bar code at the back side of a gift card. (b) Reverse image of the bar code captured by 11 % Sn photoconductor.

Chapter 7: Summary and future work

7.1 Summary

This research focuses on the study of Si-based GeSn photodetector to provide a non-expensive high-performance solution for FPAs in SWIR towards MIR detection. Two primary photodetector structures were fabricated and systematically characterized to set up a baseline for single element detector. The active GeSn layer was growth on a buffer Ge layer on a Si substrate by using a CVD reactor.

The first studied structure was a thin film GeSn photoconductor with a nominal Sn composition up to 10 % and an active GeSn layer thickness of 200 nm. The photoconductive gain was enhanced by introducing interdigitated electrodes structures which reduces the carrier transit time. A peak responsivity of 2.85 A/W was reported at 1.55 µm and 77 K and a cut-off wavelength was extended to 2.6 µm at 300 K. As the growth technique was gradually improved, higher Sn composition were incorporated and thicker GeSn active layer were achieved. GeSn photoconductors with Sn composition of 11 %, 13 %, 16 %, 17.5 %, 20 %, and 22 %, and a thickness up to 1.0 µm were fabricated and characterized. The cut-off wavelength of 22 % Sn device surpassed the SWIR and reached 4.0 µm while 11 % Sn device showed a peak responsivity of 20 A/W at 2.0 µm due to superior material quality.

The second type of detector that was studied is a DHS Ge/GeSn/Ge on Si substrate photodiode. It involves two photodiode structure designs. The first one which contains 7 % and 10 % Sn was used to evaluate the photodiode performance by extracting temperature dependent spectral response, I-V characteristic, shunt resistance, series resistance, responsivity, and D*. Several issues limiting the GeSn photodiode performance were found: (1) the thin GeSn active layer (~ 250 nm) that results in low responsivity, (2) the short cut-off wavelength at 2.4 µm due to compressive strain and low Sn incorporation, (3) the short depletion region, because of high doping junction (~ 10^{19} cm^{-3}), that enables high dark current (25 mA/cm^2 at -0.1V) and poor carrier collection. The second photodiode design was proposed to address the above factors not only based on the analyzed results but also from the growth capability. The cut-off wavelength of 11 % Sn with a thick GeSn absorption layer of 700 nm is extended to 2.8 µm at 300 K. The device shows a dark current density of 7.9 mA/cm^2 at 0.1 V. The room-temperature responsivity was measured as 0.34 A/W at 2.0 µm, corresponding to an external quantum efficiency of 20 %.

Surface leakage current is a significant factor that contributes to the high dark current of GeSn photoconductor and photodiode. This could be reduced by applying an effective surface passivation technique. Two types of surface passivation have been studied in this work: germanium oxynitride (GeON) and germanium oxide followed by aluminum oxide (GeO / Al_2O_3). The first technique, which was applied on photodiodes, has revealed a reduction of dark current at low bias voltage. This results in an overall increase in D*. The second technique was deposited on high Sn composition photoconductor devices by using an ALD system. Due to limited choice of oxide precursor which has lower oxidation energy and low deposition temperature, the desired passivation layer was not completely fulfilled. As a result, no significant improvement was observed.

The next step in the development of Si-based GeSn photodetector was a demonstration of IR imaging using a single element photodetector fabricated in this study. The single pixel was integrated to a 3D-stage and its movement was programmed to mimic the function of an array detector. Transmission mode and reflection mode were performed to capture an IR image of a metal-coated star and a series of number using 11 % Sn photoconductor and 11 % Sn photodiode. This was one step toward the realization of FPAs in SWIR.

7.2 Future work

The performance of GeSn photoconductor is currently withheld by high dark current. In addition to the lack of an effective surface passivation method, the defective layers at the interface layers of Ge buffer / Si substrate and GeSn / Ge buffer is believed to be the source of high dark current. One way to address this issue is to remove the defective layers and fabricate the device on an SiO_2 / Si substrate. The fabrication process follows Figure 58.

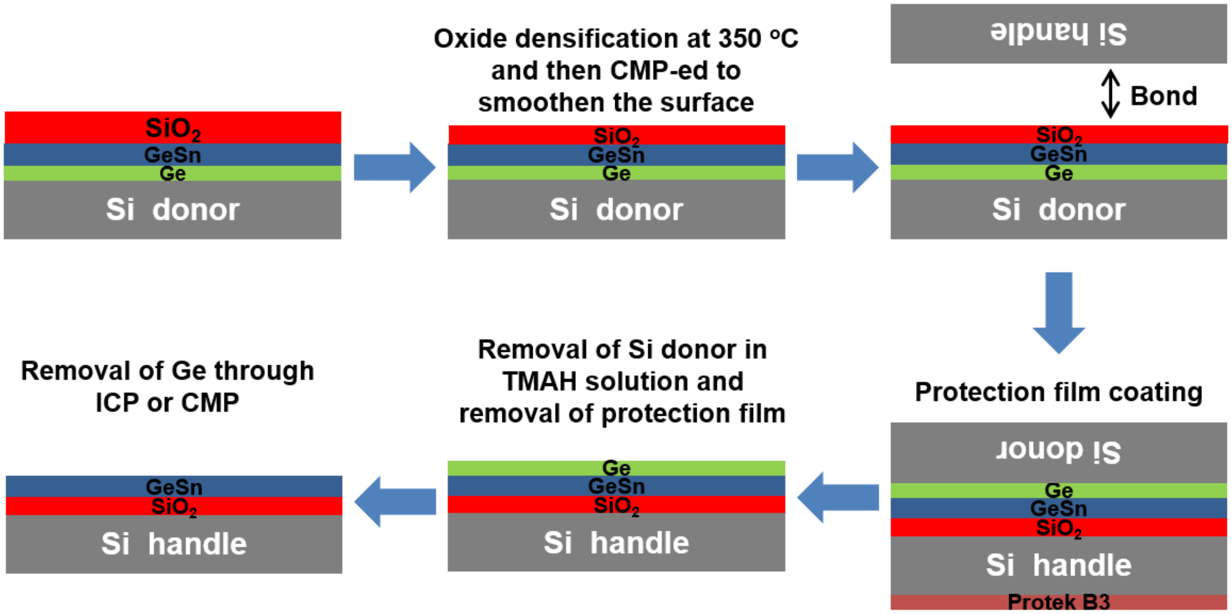

Figure 58: Processing flow of substrate removal process

Based on the results of two passivation method presented in this study, there is still room to improve. The germanium oxynitride method needs more optimization on the layer thickness while more efforts adjusting the deposition temperature, pressure, and choice of oxygen precursor are required for the case of germanium oxide /aluminum oxide method.

With the success of IR imaging using a single pixel GeSn photodetector, fabrication and demonstration of IR image capture using a linear array of detector is the next step to realize the Si-based GeSn FPAs for SWIR detection. Figure 59 shows the third mask of the photomask design of an array with 16 single photoconductors. The photoconductor size is reduced to 100×100 µm^2 and the pitch size is either 20 or 10 µm.

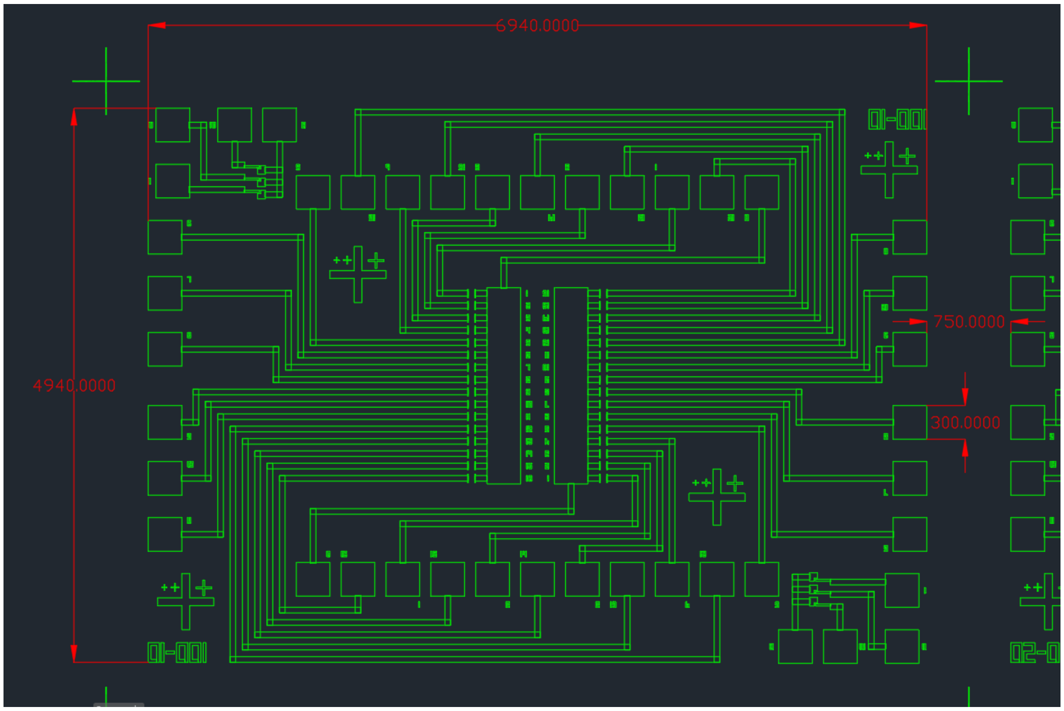

Figure 59: Mask layout (3rd mask) of linear array detector.

Unlike the single photoconductor, the change of current in each pixel as light is on is collected by an external readout circuit without using lock-in amplifier technique. In this study, 16 channels National Instrument data acquisition (DAQ) was used. Since the DAQ has a minimum detection voltage of 300 µV and a total applied voltage of +/- 10 V, a basic differential op-amp with a gain of 10 was required. The signal here could be understood as the photocurrent signal by subtracting signal from the pixel with the one covered with metal as illustrated in Figure 60. As the array is composed of 16 pixels, an equal number of op-amps are needed. The amplified output voltage of 16 op-amps are subsequently connected to the DAQ.

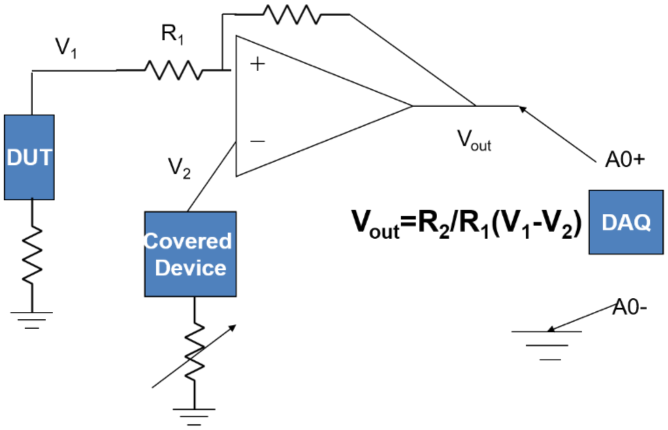

Figure 60: Circuit connection of photoconductor linear array.

References

[1] W. Herschel, “XIV. Experiments on the refrangibility of the invisible rays of the sun,” *Philos. Trans. R. Soc. Lond.*, vol. 90, pp. 284–292, Jan. 1800.

[2] A. Buffaz, M. Carras, L. Doyennette, A. Nedelcu, P. Bois, and V. Berger, “State of the art of quantum cascade photodetectors,” in *Infrared Technology and Applications XXXVI*, 2010, vol. 7660, p. 76603Q.

[3] C. L. Tan and H. Mohseni, “Emerging technologies for high performance infrared detectors,” *Nanophotonics*, vol. 7, no. 1, pp. 169–197, 2018.

[4] C. Downs and T. E. Vandervelde, “Progress in Infrared Photodetectors Since 2000,” *Sensors*, vol. 13, no. 4, pp. 5054–5098, Apr. 2013.

[5] H. Chen, M. S. Asif, A. C. Sankaranarayanan, and A. Veeraraghavan, “FPA-CS: Focal Plane Array-based Compressive Imaging in Short-wave Infrared,” *ArXiv150404085 Cs*, Apr. 2015.

[6] M. P. Hansen and D. S. Malchow, “Overview of SWIR detectors, cameras, and applications,” 2008, vol. 6939, p. 69390I–69390I–11.

[7] A. Rogalski, “History of infrared detectors,” *Opto-Electron. Rev.*, vol. 20, no. 3, pp. 279–308, Sep. 2012.

[8] A. Rogalski, “Infrared detectors: an overview,” *Infrared Phys. Technol.*, vol. 43, no. 3, pp. 187–210, Jun. 2002.

[9] J. Michel, J. Liu, and L. C. Kimerling, “High-performance Ge-on-Si photodetectors,” *Nat. Photonics*, vol. 4, no. 8, pp. 527–534, Aug. 2010.

[10] J. Liu, L. C. Kimerling, and J. Michel, “Monolithic Ge-on-Si lasers for large-scale electronic–photonic integration,” *Semicond. Sci. Technol.*, vol. 27, no. 9, p. 094006, 2012.

[11] A. Rogalski, “Progress in focal plane array technologies,” *Prog. Quantum Electron.*, vol. 36, no. 2, pp. 342–473, Mar. 2012.

[12] D. W. Jenkins and J. D. Dow, “Electronic properties of metastable Ge1-xSnx alloys,” *Phys. Rev. B*, vol. 36, no. 15, pp. 7994–8000, Nov. 1987.

[13] R. Soref, “Toward silicon-based longwave integrated optoelectronics (LIO),” 2008, vol. 6898, pp. 689809-689809–13.

[14] J. Liu, X. Sun, R. Camacho-Aguilera, L. C. Kimerling, and J. Michel, “Ge-on-Si laser operating at room temperature,” *Opt. Lett.*, vol. 35, no. 5, pp. 679–681, Mar. 2010.

[15] S. A. Ghetmiri *et al.*, “Direct-bandgap GeSn grown on silicon with 2230 nm photoluminescence,” *Appl. Phys. Lett.*, vol. 105, no. 15, p. 151109, Oct. 2014.

[16] B. Conley, “GeSn Devices for Short-Wave Infrared Optoelectronics,” *Theses Diss.*, Dec. 2011.

[17] O. Gurdai, J. Carlsson, N. Taylor, and P. Desjardins, “Low-temperature growth and critical epitaxial thicknesses of fully strained metastable Ge1−xSnx (x≲0.26) alloys on Ge(001)2×1,” *J. Appl. Phys.*, vol. 83, no. 1, pp. 162–170, Jan. 1998.

[18] J. Taraci, J. Tolle, and J. Kouvetakis, “Simple chemical routes to diamond-cubic germanium–tin alloys,” *Appl. Phys. Lett.*, vol. 78, no. 23, pp. 3607–3609, May 2001.

[19] M. Bauer *et al.*, “Ge–Sn semiconductors for band-gap and lattice engineering,” *Appl. Phys. Lett.*, vol. 81, no. 16, pp. 2992–2994, Oct. 2002.

[20] V. R. D’Costa *et al.*, “Optical critical points of thin-film $Ge_{1-y}Sn_y$ alloys: A comparative $Ge_{1-y}Sn_y$/ $Ge_{1-y}Si_y$ study,” *Phys. Rev. B*, vol. 73, no. 12, p. 125207, Mar. 2006.

[21] S. Wirths *et al.*, “Lasing in direct-bandgap GeSn alloy grown on Si,” *Nat. Photonics*, vol. 9, no. 2, pp. 88–92, Feb. 2015.

[22] S. Al-Kabi *et al.*, “An optically pumped 2.5 µm GeSn laser on Si operating at 110 K,” *Appl. Phys. Lett.*, vol. 109, no. 17, p. 171105, Oct. 2016.

[23] J. Margetis *et al.*, “Si-based GeSn lasers with wavelength coverage of 2 to 3 µm and operating temperatures up to 180 K,” *ArXiv170805927 Phys.*, Aug. 2017.

[24] G. Sun, R. A. Soref, and H. H. Cheng, “Design of a Si-based lattice-matched room-temperature GeSn/GeSiSn multi-quantum-well mid-infrared laser diode,” *Opt. Express*, vol. 18, no. 19, pp. 19957–19965, Sep. 2010.

[25] B. Schwartz *et al.*, “Electroluminescence of GeSn/Ge MQW LEDs on Si substrate,” *Opt. Lett.*, vol. 40, no. 13, pp. 3209–3212, Jul. 2015.

[26] D. Stange *et al.*, “Study of GeSn based heterostructures: towards optimized group IV MQW LEDs,” *Opt. Express*, vol. 24, no. 2, pp. 1358–1367, Jan. 2016.

[27] S. A. Ghetmiri *et al.*, “Study of a SiGeSn/GeSn/SiGeSn structure toward direct bandgap type-I quantum well for all group-IV optoelectronics,” *Opt. Lett.*, vol. 42, no. 3, pp. 387–390, Feb. 2017.

[28] P. C. Grant *et al.*, “Direct bandgap type-I GeSn/GeSn quantum well on a GeSn- and Ge-buffered Si substrate,” *AIP Adv.*, vol. 8, no. 2, p. 025104, Feb. 2018.

[29] J. D. Gallagher, C. L. Senaratne, P. Sims, T. Aoki, J. Menéndez, and J. Kouvetakis, “Electroluminescence from GeSn heterostructure pin diodes at the indirect to direct transition,” *Appl. Phys. Lett.*, vol. 106, no. 9, p. 091103, Mar. 2015.

[30] Y. Zhou *et al.*, “Systematic study of GeSn heterostructure-based light-emitting diodes towards mid-infrared applications,” *J. Appl. Phys.*, vol. 120, no. 2, p. 023102, Jul. 2016.

[31] J. Mathews, R. Roucka, J. Xie, S.-Q. Yu, J. Menéndez, and J. Kouvetakis, “Extended performance GeSn/Si(100) p-i-n photodetectors for full spectral range telecommunication applications,” *Appl. Phys. Lett.*, vol. 95, no. 13, p. 133506, Sep. 2009.

[32] J. Werner *et al.*, “Germanium-tin p-i-n photodetectors integrated on silicon grown by molecular beam epitaxy,” *Appl. Phys. Lett.*, vol. 98, no. 6, p. 061108, Feb. 2011.

[33] R. Roucka *et al.*, “High-Performance Near-IR Photodiodes: A Novel Chemistry-Based Approach to Ge and GeSn Devices Integrated on Silicon,” *IEEE J. Quantum Electron.*, vol. 47, no. 2, pp. 213–222, Feb. 2011.

[34] S. Su *et al.*, “GeSn p-i-n photodetector for all telecommunication bands detection,” *Opt. Express*, vol. 19, no. 7, pp. 6400–6405, Mar. 2011.

[35] R. Beeler, C. Xu, D. J. Smith, G. Grzybowski, J. Menéndez, and J. Kouvetakis, “Compositional dependence of the absorption edge and dark currents in Ge1−x−ySixSny/Ge(100) photodetectors grown via ultra-low-temperature epitaxy of Ge4H10, Si4H10, and SnD4,” *Appl. Phys. Lett.*, vol. 101, no. 22, p. 221111, Nov. 2012.

[36] H. Tseng *et al.*, “GeSn-based p-i-n photodiodes with strained active layer on a Si wafer,” *Appl. Phys. Lett.*, vol. 103, no. 23, p. 231907, Dec. 2013.

[37] M. Oehme *et al.*, “GeSn p-i-n detectors integrated on Si with up to 4% Sn,” *Appl. Phys. Lett.*, vol. 101, no. 14, p. 141110, Oct. 2012.

[38] A. Gassenq *et al.*, “GeSn/Ge heterostructure short-wave infrared photodetectors on silicon,” *Opt. Express*, vol. 20, no. 25, pp. 27297–27303, Dec. 2012.

[39] D. Zhang *et al.*, “High-responsivity GeSn short-wave infrared p-i-n photodetectors,” *Appl. Phys. Lett.*, vol. 102, no. 14, p. 141111, Apr. 2013.

[40] J. Y. J. Lin *et al.*, “Fabrication of GeSn-On-Insulator (GSOI) to enable monolithic 3D co-integration of logic and photonics,” in *2013 Symposium on VLSI Technology*, 2013, pp. T32–T33.

[41] M. Coppinger, Jo. Hart, N. Bhargava, S. Kim, and J. Kolodzey, “Photoconductivity of germanium tin alloys grown by molecular beam epitaxy,” *Appl. Phys. Lett.*, vol. 102, no. 14, p. 141101, Apr. 2013.

[42] S. Kim, J. Gupta, N. Bhargava, M. Coppinger, and J. Kolodzey, “Current-Voltage Characteristics of GeSn/Ge Heterojunction Diodes Grown by Molecular Beam Epitaxy,” *IEEE Electron Device Lett.*, vol. 34, no. 10, pp. 1217–1219, Oct. 2013.

[43] Y.-H. Peng, H. H. Cheng, V. I. Mashanov, and G.-E. Chang, “GeSn p-i-n waveguide photodetectors on silicon substrates,” *Appl. Phys. Lett.*, vol. 105, no. 23, p. 231109, Dec. 2014.

[44] M. Oehme *et al.*, “GeSn-on-Si normal incidence photodetectors with bandwidths more than 40 GHz,” *Opt. Express*, vol. 22, no. 1, pp. 839–846, Jan. 2014.

[45] M. Oehme *et al.*, “GeSn/Ge multiquantum well photodetectors on Si substrates,” *Opt. Lett.*, vol. 39, no. 16, pp. 4711–4714, Aug. 2014.

[46] B. R. Conley *et al.*, “Temperature dependent spectral response and detectivity of GeSn photoconductors on silicon for short wave infrared detection,” *Opt. Express*, vol. 22, no. 13, pp. 15639–15652, Jun. 2014.

[47] B. R. Conley *et al.*, “Si based GeSn photoconductors with a 1.63 A/W peak responsivity and a 2.4 μm long-wavelength cutoff,” *Appl. Phys. Lett.*, vol. 105, no. 22, p. 221117, Dec. 2014.

[48] S. Kim, N. Bhargava, J. Gupta, M. Coppinger, and J. Kolodzey, “Infrared photoresponse of GeSn/n-Ge heterojunctions grown by molecular beam epitaxy,” *Opt. Express*, vol. 22, no. 9, pp. 11029–11034, May 2014.

[49] Y. Dong *et al.*, “Suppression of dark current in germanium-tin on silicon p-i-n photodiode by a silicon surface passivation technique,” *Opt. Express*, vol. 23, no. 14, pp. 18611–18619, Jul. 2015.

[50] T. N. Pham *et al.*, “Si-based Ge0.9Sn0.1 photodetector with peak responsivity of 2.85 A/W and longwave cutoff at 2.4 μm,” *Electron. Lett.*, vol. 51, no. 11, pp. 854–856, May 2015.

[51] C. Chang, H. Li, S. H. Huang, H. H. Cheng, G. Sun, and R. A. Soref, “Sn-based Ge/Ge0.975Sn0.025/Ge p-i-n photodetector operated with back-side illumination,” *Appl. Phys. Lett.*, vol. 108, no. 15, p. 151101, Apr. 2016.

[52] C. Chang *et al.*, “Ge0.975Sn0.025 320 × 256 imager chip for 1.6–1.9 μm infrared vision,” *Appl. Opt.*, vol. 55, no. 36, pp. 10170–10173, Dec. 2016.

[53] H. Cong *et al.*, “Silicon Based GeSn p-i-n Photodetector for SWIR Detection,” *IEEE Photonics J.*, vol. 8, no. 5, pp. 1–6, Oct. 2016.

[54] J. Zheng *et al.*, “GeSn p-i-n photodetectors with GeSn layer grown by magnetron sputtering epitaxy,” *Appl. Phys. Lett.*, vol. 108, no. 3, p. 033503, Jan. 2016.

[55] T. Pham *et al.*, “Systematic study of Si-based GeSn photodiodes with 2.6 μm detector cutoff for short-wave infrared detection,” *Opt. Express*, vol. 24, no. 5, pp. 4519–4531, Mar. 2016.

[56] Y.-H. Huang, G.-E. Chang, H. Li, and H. H. Cheng, “Sn-based waveguide p-i-n photodetector with strained GeSn/Ge multiple-quantum-well active layer,” *Opt. Lett.*, vol. 42, no. 9, pp. 1652–1655, May 2017.

[57] M. Morea *et al.*, “Passivation of multiple-quantum-well Ge0.97Sn0.03/Ge p-i-n photodetectors,” *Appl. Phys. Lett.*, vol. 110, no. 9, p. 091109, Feb. 2017.

[58] Y. Dong *et al.*, “Two-micron-wavelength germanium-tin photodiodes with low dark current and gigahertz bandwidth,” *Opt. Express*, vol. 25, no. 14, pp. 15818–15827, Jul. 2017.

[59] W. Wang *et al.*, “High-performance GeSn photodetector and fin field-effect transistor (FinFET) on an advanced GeSn-on-insulator platform,” *Opt. Express*, vol. 26, no. 8, pp. 10305–10314, Apr. 2018.

[60] J. Kouvetakis and A. V. G. Chizmeshya, “New classes of Si-based photonic materials and device architectures via designer molecular routes,” *J. Mater. Chem.*, vol. 17, no. 17, pp. 1649–1655, Apr. 2007.

[61] S. Wirths *et al.*, “Reduced Pressure CVD Growth of Ge and Ge1−xSnx Alloys,” *ECS J. Solid State Sci. Technol.*, vol. 2, no. 5, pp. N99–N102, Jan. 2013.

[62] A. Mosleh *et al.*, “Direct Growth of Ge1−xSnx Films on Si Using a Cold-Wall Ultra-High Vacuum Chemical-Vapor-Deposition System,” *Front. Mater.*, vol. 2, 2015.

[63] J. Margetis *et al.*, “Growth and Characterization of Epitaxial Ge1-XSnx Alloys and Heterostructures Using a Commercial CVD System,” *ECS Trans.*, vol. 64, no. 6, pp. 711–720, Aug. 2014.

[64] P. C. Grant *et al.*, “Comparison study of the low temperature growth of dilute GeSn and Ge,” *J. Vac. Sci. Technol. B Nanotechnol. Microelectron. Mater. Process. Meas. Phenom.*, vol. 35, no. 6, p. 061204, Oct. 2017.

[65] J. Margetis *et al.*, “Fundamentals of Ge1−xSnx and SiyGe1−x-ySnx RPCVD epitaxy,” *Mater. Sci. Semicond. Process.*, vol. 70, pp. 38–43, Nov. 2017.

[66] J. Margetis *et al.*, “Study of low-defect and strain-relaxed GeSn growth via reduced pressure CVD in H2 and N2 carrier gas,” *J. Cryst. Growth*, vol. 463, pp. 128–133, Apr. 2017.

[67] F. Gencarelli *et al.*, “Low-temperature Ge and GeSn Chemical Vapor Deposition using Ge2H6,” *Thin Solid Films*, vol. 520, no. 8, pp. 3211–3215, Feb. 2012.

[68] O. Gurdal *et al.*, “Low-temperature growth and critical epitaxial thicknesses of fully strained metastable Ge1−xSnx (x≲0.26) alloys on Ge(001)2×1,” *J. Appl. Phys.*, vol. 83, no. 1, pp. 162–170, Jan. 1998.

[69] R. Chen, H. Lin, Y. Huo, C. Hitzman, T. I. Kamins, and J. S. Harris, “Increased photoluminescence of strain-reduced, high-Sn composition Ge1−xSnx alloys grown by molecular beam epitaxy,” *Appl. Phys. Lett.*, vol. 99, no. 18, p. 181125, Oct. 2011.

[70] M. Coppinger, J. Hart, N. Bhargava, S. Kim, and J. Kolodzey, “Photoconductivity of germanium tin alloys grown by molecular beam epitaxy,” *Appl. Phys. Lett.*, vol. 102, no. 14, p. 141101, Apr. 2013.

[71] T. Ping, H. Lei, C. H. H, W. Huan-Hua, and W. Xiao-Shan, “Epitaxial growth of Ge 1– x Sn x films with x up to 0.14 grown on Ge (00l) at low temperature,” *Chin. Phys. B*, vol. 23, no. 8, p. 088112, 2014.

[72] N. von den Driesch *et al.*, “SiGeSn Ternaries for Efficient Group IV Heterostructure Light Emitters,” *Small*, vol. 13, no. 16, p. 1603321, Apr. 2017.

[73] R. Chen *et al.*, “Demonstration of a Ge/GeSn/Ge Quantum-Well Microdisk Resonator on Silicon: Enabling High-Quality Ge(Sn) Materials for Micro- and Nanophotonics,” *Nano Lett.*, vol. 14, no. 1, pp. 37–43, Jan. 2014.

[74] A. Mosleh *et al.*, “Material Characterization of Ge1−x Sn x Alloys Grown by a Commercial CVD System for Optoelectronic Device Applications,” *J. Electron. Mater.*, vol. 43, no. 4, pp. 938–946, Apr. 2014.

[75] T. S. Kim, H. Y. Yang, Y. H. Kil, T. S. Jeong, S. Kang, and K. H. Shim, “Dry Etching of Germanium by Using Inductively Coupled CF_4 Plasma,” *J. Korean Phys. Soc.*, vol. 54, no. 6, pp. 2290–2296, Jun. 2009.

[76] S. Gupta *et al.*, “Highly Selective Dry Etching of Germanium over Germanium–Tin (Ge1–xSnx): A Novel Route for Ge1–xSnx Nanostructure Fabrication,” *Nano Lett.*, vol. 13, no. 8, pp. 3783–3790, Aug. 2013.

[77] S. A. Ghetmiri *et al.*, “Shortwave-infrared photoluminescence from Ge1−xSnx thin films on silicon,” *J. Vac. Sci. Technol. B Nanotechnol. Microelectron. Mater. Process. Meas. Phenom.*, vol. 32, no. 6, p. 060601, Oct. 2014.

[78] V. Sorianello *et al.*, “High responsivity near-infrared photodetectors in evaporated Ge-on-Si,” *Appl. Phys. Lett.*, vol. 101, no. 8, p. 081101, Aug. 2012.

[79] J. Margetis, S.-Q. Yu, N. Bhargava, B. Li, W. Du, and J. Tolle, “Strain engineering in epitaxial Ge 1− x Sn x : a path towards low-defect and high Sn-content layers,” *Semicond. Sci. Technol.*, vol. 32, no. 12, p. 124006, 2017.

[80] W. Dou *et al.*, “Investigation of GeSn Strain Relaxation and Spontaneous Composition Gradient for Low-Defect and High-Sn Alloy Growth,” *Sci. Rep.*, vol. 8, no. 1, p. 5640, Apr. 2018.

[81] Y. Dong *et al.*, “Etching of germanium-tin using ammonia peroxide mixture,” *J. Appl. Phys.*, vol. 118, no. 24, p. 245303, Dec. 2015.

[82] R. Cheng *et al.*, “Relaxed and Strained Patterned Germanium-Tin Structures: A Raman Scattering Study,” *ECS J. Solid State Sci. Technol.*, vol. 2, no. 4, pp. P138–P145, Jan. 2013.

[83] R. Chen *et al.*, “Material characterization of high Sn-content, compressively-strained GeSn epitaxial films after rapid thermal processing,” *J. Cryst. Growth*, vol. 365, pp. 29–34, Feb. 2013.

[84] J. R. Sites and P. H. Mauk, “Diode quality factor determination for thin-film solar cells,” *Sol. Cells*, vol. 27, no. 1, pp. 411–417, Oct. 1989.

[85] S. S. Hegedus and W. N. Shafarman, “Thin-film solar cells: device measurements and analysis,” *Prog. Photovolt. Res. Appl.*, vol. 12, no. 2-3, pp. 155–176, Mar. 2004.

[86] A. Rogalski, *Infrared Detectors, Second Edition*. CRC Press, 2010.

[87] H. W. Yoon, M. C. Dopkiss, and G. P. Eppeldauer, “Performance comparisons of InGaAs, extended InGaAs, and short-wave HgCdTe detectors between 1µm and 2.5µm,” in *Infrared Spaceborne Remote Sensing XIV*, 2006, vol. 6297, p. 629703.

[88] W. Shockley and W. T. Read, “Statistics of the Recombinations of Holes and Electrons,” *Phys. Rev.*, vol. 87, no. 5, pp. 835–842, Sep. 1952.

[89] Z. Huang, J. Oh, S. K. Banerjee, and J. C. Campbell, “Effectiveness of SiGe Buffer Layers in Reducing Dark Currents of Ge-on-Si Photodetectors,” *IEEE J. Quantum Electron.*, vol. 43, no. 3, pp. 238–242, Mar. 2007.

[90] G. Karve *et al.*, “Origin of dark counts in In0.53Ga0.47As⁄In0.52Al0.48As avalanche photodiodes operated in Geiger mode,” *Appl. Phys. Lett.*, vol. 86, no. 6, p. 063505, Feb. 2005.

[91] C. Lu, C. H. Lee, T. Nishimura, and A. Toriumi, “Yttrium scandate thin film as alternative high-permittivity dielectric for germanium gate stack formation,” *Appl. Phys. Lett.*, vol. 107, no. 7, p. 072904, Aug. 2015.

[92] M. Oehme *et al.*, “Franz-Keldysh effect in GeSn pin photodetectors,” *Appl. Phys. Lett.*, vol. 104, no. 16, p. 161115, Apr. 2014.

[93] S. Sze and K. Ng, *Physics of Semiconductor Devices*. Wiley.

[94] Z. J. Quan, Z. F. Li, W. D. Hu, Z. H. Ye, X. N. Hu, and W. Lu, “Parameter determination from resistance-voltage curve for long-wavelength HgCdTe photodiode,” *J. Appl. Phys.*, vol. 100, no. 8, p. 084503, Oct. 2006.

[95] C. Schulte-Braucks *et al.*, “Negative differential resistance in direct bandgap GeSn p-i-n structures,” *Appl. Phys. Lett.*, vol. 107, no. 4, p. 042101, Jul. 2015.

[96] V. Urick, J. McKinney, and K. Williams, *Fundamentals of Microwave Photonics*. Wiley.

[97] P. Basu, *Theory of Optical Processes in Semiconductors: : bulk and microstructures*. Oxford University Press Canada.

[98] C. O. Chui, F. Ito, and K. C. Saraswat, “Scalability and electrical properties of germanium oxynitride MOS dielectrics,” *IEEE Electron Device Lett.*, vol. 25, no. 9, pp. 613–615, Sep. 2004.

[99] K. Kutsuki, I. Hideshima, G. Okamoto, T. Hosoi, T. Shimura, and H. Watanabe, “Thermal Robustness and Improved Electrical Properties of Ultrathin Germanium Oxynitride Gate Dielectric,” *Jpn. J. Appl. Phys.*, vol. 50, no. 1R, p. 010106, Jan. 2011.

[100] T. Maeda, T. Yasuda, M. Nishizawa, N. Miyata, Y. Morita, and S. Takagi, “Pure germanium nitride formation by atomic nitrogen radicals for application to Ge metal-insulator-semiconductor structures,” *J. Appl. Phys.*, vol. 100, no. 1, p. 014101, Jul. 2006.

[101] K. Kato, H. Kondo, M. Sakashita, and S. Zaima, “Formation processes of Ge3N4 films by radical nitridation and their electrical properties,” *Thin Solid Films*, vol. 518, no. 6, Supplement 1, pp. S226–S230, Jan. 2010.

[102] D. J. Hymes and J. J. Rosenberg, “Growth and Materials Characterization of Native Germanium Oxynitride Thin Films on Germanium,” *J. Electrochem. Soc.*, vol. 135, no. 4, pp. 961–965, Apr. 1988.

[103] D. M. Hoffman *et al.*, “Plasma-enhanced chemical vapor deposition of silicon, germanium, and tin nitride thin films from metalorganic precursors,” *J. Vac. Sci. Technol. Vac. Surf. Films*, vol. 13, no. 3, pp. 820–825, May 1995.

[104] K. Maeda, N. Saito, Y. Inoue, and K. Domen, “Dependence of Activity and Stability of Germanium Nitride Powder for Photocatalytic Overall Water Splitting on Structural Properties,” *Chem. Mater.*, vol. 19, no. 16, pp. 4092–4097, Aug. 2007.

[105] C. Tindall and J. C. Hemminger, “HREELS studies of the chemistry of nitrogen hydrides on Ge(100): formation of a surface nitride at low temperatures,” *Surf. Sci.*, vol. 330, no. 1, pp. 67–74, Jun. 1995.

[106] D. Kuzum *et al.*, “Ge-Interface Engineering with Ozone Oxidation for Low Interface-State Density,” *IEEE Electron Device Lett.*, vol. 29, no. 4, pp. 328–330, Apr. 2008.

[107] K. Prabhakaran and T. Ogino, “Oxidation of Ge(100) and Ge(111) surfaces: an UPS and XPS study,” *Surf. Sci.*, vol. 325, no. 3, pp. 263–271, Mar. 1995.

[108] M. B. Gonzalez *et al.*, “Defect assessment and leakage control in Ge junctions,” *Microelectron. Eng.*, vol. 125, pp. 33–37, Aug. 2014.

[109] S. Gupta, R. Chen, J. S. Harris, and K. C. Saraswat, “Atomic layer deposition of Al2O3 on germanium-tin (GeSn) and impact of wet chemical surface pre-treatment,” *Appl. Phys. Lett.*, vol. 103, no. 24, p. 241601, Dec. 2013.

[110] D. Schmeisser *et al.*, “Surface oxidation states of germanium,” *Surf. Sci.*, vol. 172, no. 2, pp. 455–465, Jul. 1986.

[111] P. Norton, “Third-generation sensors for night vision,” *Opto-Electron. Rev.*, vol. 14, no. 1, pp. 1–10, Mar. 2006.

[112] P. R. Norton, J. B. Campbell, S. B. Horn, and D. A. Reago, “Third-generation infrared imagers,” in *Infrared Technology and Applications XXVI*, 2000, vol. 4130, pp. 226–237.

[113] A. Rogalski, J. Antoszewski, and L. Faraone, “Third-generation infrared photodetector arrays,” *J. Appl. Phys.*, vol. 105, no. 9, p. 091101, May 2009.

Appendix A: Measurement methods

The temperature-dependent testing setup is mainly composed of a Janis cryostat using liquid nitrogen cooling and controlled by a Lakeshore cryogenic controller. A chip carrier with wired-bonded devices placed inside cryostat was connected to outside measurement equipment through an isolated BNC feed-through system. The current-voltage characteristic was measured using a Keithley 6487 picoammeter, based on which the electrical parameters such as reverse saturation current, series resistance, and shunt resistance were extracted. The temperature-dependent spectral response measurement was conducted by using a Fourier-transform infrared (FTIR) spectrometer system. The IR light from the internal source was guided and focused to the sample mounted in the cryostat. Although this method reduces the high-order diffraction ambiguity of full IR spectrum analysis, the radiant flux of the light source remains arbitrary. For the responsivity measurement, a laser diode with a wavelength of 1.55 or 2.0 μm optically chopped at 380 Hz and a lock-in amplifier were used. The optical power of the laser diode was measured using an ILX Lightwave power meter. The absolute responsivity values were calibrated using a NIST traceable InGaAs p-i-n photodiode. Moreover, the D* was calculated based on measured values of responsivity and the dark current.

The spectral EQE of a GeSn photodiode was first reported. It was calibrated by using an Extended InGaAs p-i-n photodiode’s spectral EQE, spectral response of the GeSn photodiode, and spectral response of the Extended InGaAs p-i-n photodiode. The spectral response of Extended InGaAs photodiode and GeSn photodiode was obtained via Nicolet 6700 FTIR system and under same condition for both photodetectors. Dividing the two spectra response at each wavelength yields a ratio which could be used to calibrate the EQE value at each wavelength of GeSn photodiode. The devices active area was taken into consideration. The ratio is: $\frac{EQE_1}{EQE_2} = \frac{S_1}{S_2} \times \frac{A_2}{A_1}$ where EQE_1, S_1, and A_1 are external quantum efficiency at a single wavelength, spectral response at a single wavelength, and active area of GeSn device while EQE_2, S_2, and A_2 are external quantum efficiency at a single wavelength, spectral response at a single wavelength, and active area of Extended InGaAs device, respectively. As A_1, A_2, S_1, S_2, and EQE_2 were known, EQE_1 was therefore calculated. EQE_2 was determined via digitized spectral EQE provided by the supplier. As the EQE of GeSn photodiode was extracted, responsivity at each single wavelength could also be determined and verified with measured value with an error less than 10 %.